

UNIVERSITÀ DEGLI STUDI DI CATANIA

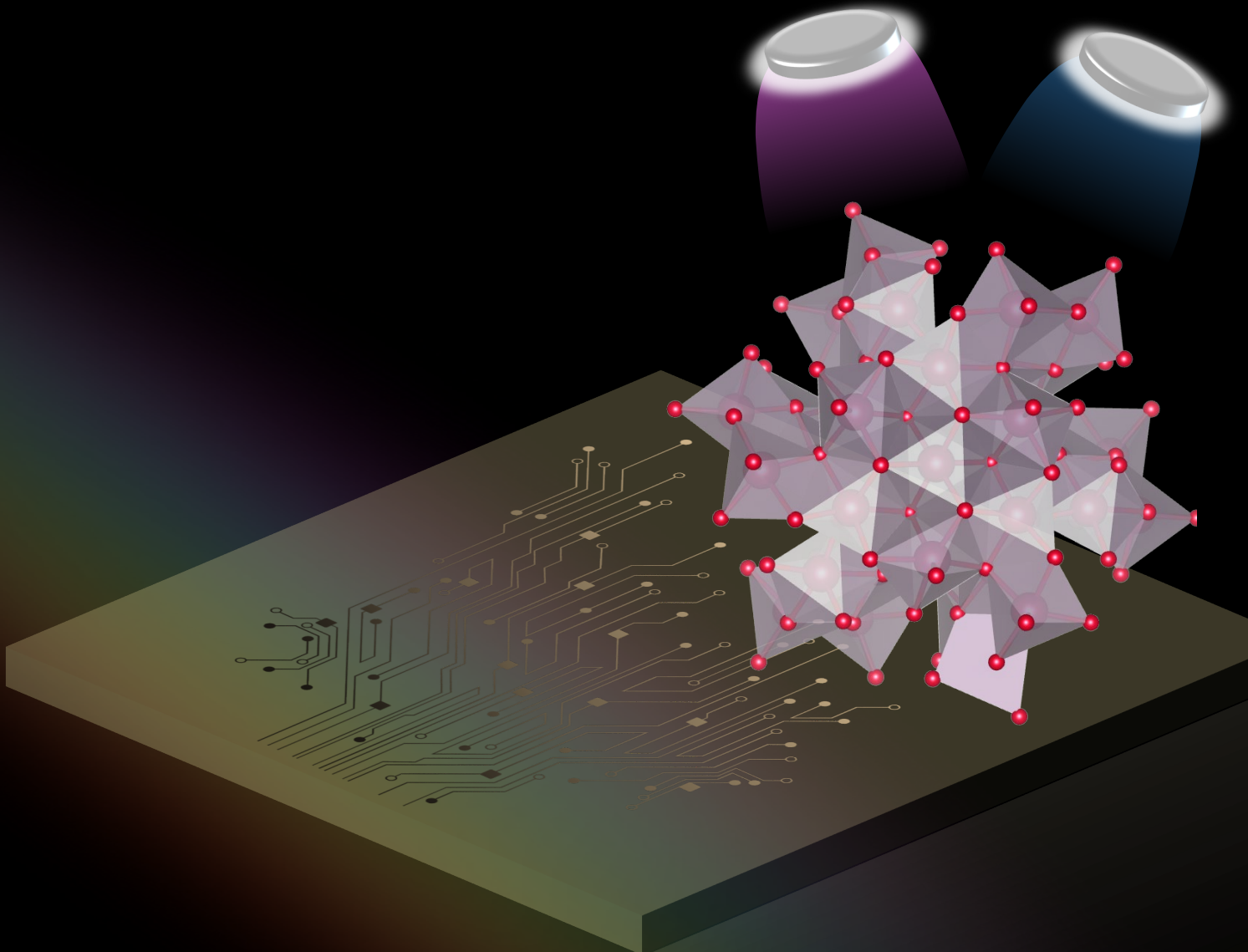
DOTTORATO DI RICERCA IN
SCIENZA DEI MATERIALI E NANOTECNOLOGIE – XXXV CICLO

Transition Metals doped In_2O_3 thin films as TCO for photovoltaic applications

Melanie Micali

TUTOR: CHIAR.MO PROF. ANTONIO TERRASI

COORDINATORE: CHIAR.MO PROF. GIUSEPPE COMPAGNINI





UNIVERSITÀ DEGLI STUDI DI CATANIA

DOTTORATO DI RICERCA IN

SCIENZA DEI MATERIALI E NANOTECNOLOGIE - XXXV CICLO

**Transition Metals doped In_2O_3 thin films
as TCO for photovoltaic applications**

Melanie Micali

TUTOR: CHIAR.MO PROF. ANTONIO TERRASI

COORDINATORE: CHIAR.MO PROF. GIUSEPPE COMPAGNINI

TESI PER IL CONSEGUIMENTO DEL TITOLO DI DOTTORE DI RICERCA

À ma grand-mère, Annie

Cover

Illustration of Transition Metals doped In_2O_3 crystal structure for TCO thin films applications grown by co-sputtering deposition.

Designed by: Melanie Micali, Daphne Antony, Antony Litovoilis

Printed in Catania, December 2022

LA STRADA NON PRESA

*Divergevano due strade in un bosco
ingiallito, e spiacente di non poterle fare
entrambe uno restando, a lungo mi fermai
una di esse finché potevo scrutando
là dove in mezzo agli arbusti svoltava.*

*Poi presi l'altra, così com'era,
che aveva forse i titoli migliori,
perché era erbosa e non portava segni;
benché, in fondo, il passar della gente
le avesse invero segnate più o meno lo stesso,*

*perché nessuna in quella mattina mostrava
sui fili d'erba l'impronta nera d'un passo.
Oh, quell'altra lasciavo a un altro giorno!
Pure, sapendo bene che strada porta a strada,
dubitavo se mai sarei tornato.*

*lo dovrò dire questo con un sospiro
in qualche posto fra molto molto tempo:
Divergevano due strade in un bosco, ed io...
io presi la meno battuta,
e di qui tutta la differenza è venuta.*

R. Frost

Contents

Abstract.....	11
List of Figures.....	13
1. Introduction.....	19
1.1. Renewable energy sources	19
1.2. PV Technologies	21
1.2.1. <i>Wafer-based crystalline silicon solar cells</i>	<i>22</i>
1.2.2. <i>SHJ solar cell design and TCO functions</i>	<i>24</i>
1.3. Transparent Electrodes for PV applications	26
1.3.1. <i>Transparent Conductive Oxide</i>	<i>26</i>
1.3.2. <i>Thin metal layer and emerging nanomaterials</i>	<i>27</i>
1.3.3. <i>Transparent Conductive Polymer</i>	<i>28</i>
1.3.4. <i>Two-dimensional materials.....</i>	<i>28</i>
2. TCO Fundamentals	29
2.1. Introduction	29
2.2. Electronic structure.....	30
2.2.1. <i>Energy band structure of semiconductors</i>	<i>30</i>
2.2.2. <i>Doping mechanism of semiconductors</i>	<i>31</i>

2.2.3. Carrier-Transport phenomena.....	33
2.3. Optical Properties.....	35
2.4. Figures of merit of Transparent Conductors.....	39
2.5. In-based TCO	40
2.5.1. Transition metals-doped In_2O_3	42
3. Experimental Methods	47
3.1. Introduction	47
3.2. TCO deposition.....	47
3.2.1. RF and DC Magnetron Sputtering.....	49
3.3. TCO characterization	51
3.3.1. Rutherford Backscattering Spectrometry.....	51
3.3.2. X-Ray Photoelectron Spectroscopy.....	53
3.3.3. X-Ray Diffraction.....	55
3.3.4. Atomic Force Microscopy.....	57
3.3.5. Kelvin Probe Force Microscopy.....	60
3.3.6. Scanning Electron Microscopy	62
3.3.7. Hall measurements.....	66
3.3.8. Transmittance and reflectance measurements	68
3.4. Devices	70
3.4.1. External Quantum Efficiency measurements	71
4. Structural, optical, and electrical characterization of ITO films co-doped with Molybdenum.....	75
4.1. Introduction	75
4.2. Experimental.....	77
4.3. Results and discussions	78
4.3.1. RBS Analysis	78
4.3.2. XPS Analysis	80

4.3.3. <i>Optical properties</i>	82
4.3.4. <i>Electrical properties</i>	84
4.4. Conclusions	85
5. Zr-doped Indium Oxide thin films as transparent electrodes for photovoltaic applications	87
5.1. Introduction	87
5.2. Methods	89
5.3. Results and discussions	91
5.3.1. <i>RBS Measurements</i>	91
5.3.2. <i>XRD Measurements</i>	93
5.3.3. <i>AFM Measurements</i>	95
5.3.4. <i>FM-KPFM Measurements</i>	96
5.3.5. <i>Electrical properties</i>	98
5.3.6. <i>Optical properties</i>	101
5.3.7. <i>Device Characterization</i>	105
5.4. Conclusions	106
Conclusions	109
A. Appendix	111
A.1 RBS Supplementary Informations	111
A.2 XRD Supplementary Informations	112
A.3 Electrical properties Supplementary Informations	113
A.4 Optical properties Supplementary Informations	114
References	117
Acknowledgements	127

List of publications.....131

Curriculum Vitae133

Abstract

Transparent Electrodes play a key role in many technological applications, from solar cells to touch-sensitive screens, OLED light sources, and smart windows. For transparent electrodes, the need to have good electrical and optical properties pushes the research towards the study of new transparent and conductive materials as an alternative to the more widely used transparent conductive oxides (TCOs). Although they possess a high degree of transparency for the visible light and good electrical conductivity, they can still be expensive and toxic, such as those based on Indium, e.g. Sn-doped Indium Oxide (ITO). Reducing the production costs and using green materials are not the only challenges in this research field. The development of new and advanced technologies, including flexible devices and multi-junction solar cells, has broadened the research to alternative materials with improved opto-electrical properties, that can be processed at low temperatures and integrated into these new device structures.

In this work, we present two Indium-based TCO, where transition metals have been introduced as donors in ITO and in In_2O_3 matrices. RF and DC Magnetron sputtering has been utilized to deposit Mo-doped ITO and Zr-doped In_2O_3 . The depositions have been performed at room temperature to address the compatibility with low-temperature fabrication processes. Furthermore, ultra-thin films with reduced thickness (15-20 nm) have been tested, to investigate the optical and electrical properties of TCO with a very small amount of material sources.

The thesis will be structured as follows:

Chapter I will represent an introduction to the energy problem related to climate warming up and the need to reduce CO_2 emissions, as predicted by The International Energy Agency (IEA) in September 2020 World Energy Outlook, when it established the normative for The Net Zero Emissions by 2050 Scenario (NZE). Renewable energies are presented as crucial sources for the energy transition and particular attention will be given to solar energy and the development of photovoltaic applications. The chapter will give an outlook of the different Si-based solar cells with a description of the different components and architecture. Among the different parts of the solar cells, special attention will be given to Transparent Electrodes and their features, also describing a list

of different types of transparent electrodes traditionally used.

Chapter II will focus on a specific family of Transparent Electrodes, the Transparent Conductive Oxides. The band structure and doping mechanism of these materials will be described along with the optical and electrical properties of TCO. Indium-based TCO will be described as starting point to introduce Transition Metal doped In_2O_3 , a promising material to replace ITO.

Chapter III will contain the theoretical part of the experimental methods used for thin film deposition and characterization. RF and DC Magnetron sputtering equipment will be described, as well as several techniques used for a wide characterization such as Rutherford Backscattering Spectrometry (RBS), X-Ray Diffraction (XRD), X-Ray Photoelectron Spectroscopy (XPS) Atomic Force Microscopy (AFM), Frequency Modulated Kelvin Probe Force Microscopy (FM-KPFM) and Scanning Electron Microscopy (SEM). The study of the electrical properties will be treated by describing sheet resistance and Hall measurements. Transmittance and reflectance measurements in the UV-VIS-NIR spectral range will be presented for the optical properties, with the description of the spectrophotometer. The last part of the chapter will focus on the materials and methods used for the device characterization implemented in this work to test the electrodes performances. The process for the implementation of the Silicon Heterojunction solar cell supplied by Enel 3Sun Company will be illustrated together with the description of the External Quantum Efficiency (EQE) measurements.

Chapter IV reports the synthesis and characterization of Mo-coped ITO (ITMO), where Molybdenum (a transition metal) has been used as donor in ITO, which already has Sn as n-type dopant. The work is thus the first attempt to improve the electro-optical performances of ITO by Mo co-doping.

Chapter V presents the second alternative to standard ITO, using another transition metal to dope In_2O_3 . In fact, Zirconium has been introduced into the In_2O_3 matrix, so obtaining IZrO (Indium Zirconium Oxide). Thin films have been deposited with different thickness and Zr atomic concentrations. As for the other TCO, electrical and optical characterizations have been done looking for enhanced transparency and improved electrical conductivity. In this chapter the implementation and characterization of IZrO on a real device will also be reported. IZrO performances as transparent electrodes have also been tested with External Quantum Efficiency measurements performed on a Silicon Heterojunction solar cell supplied by Enel 3Sun where IZrO thin films have been deposited as front and back transparent electrodes.

List of Figures

Figure 1.1: mean anomaly of surface temperature for (a) 1990-1994 , (b) 2000-2004 (b), and (c) 2017-2021 five-years range.20

Figure 1.2: grams of CO2 emitted for kW/h for different renewable energy.21

Figure 1.3: conversion efficiencies for different photovoltaic technologies, plotted from 1976 to 2022. This plot is courtesy of the National Renewable Energy Laboratory, Golden, CO [8].....22

Figure 1.4: schematic representation of different solar cells architecture: (a) Al-BSF; (b) PERC; (c) PERL; (d) Monofacial SHJ; (e) Bifacial SHJ; (f) Tandem. 24

Figure 2.1: Calculated band structure of In_2O_331

Figure 2.2: schematic representation of doping mechanism and defect levels position for n-type (a) and p-type (c) semiconductors. Density of states for n-type (c) and p-type (d) semiconductor upon doping. The green dashed lines represent the Fermi.....32

Figure 2.3: Optical transitions: direct transition (a); indirect transition involving phonon absorption (b) and phonon emission (c).....36

Figure 2.4: Increase of the energy band gap from E_{g0} (a) for non-doped semiconductor to $E_{g0} + \Delta E_{gMB}$ (b) for doped semiconductor due to Moss-Burstein effect.37

Figure 2.5: Transmission, reflection and absorption spectra of a typical TCO. .38

Figure 2.6: Bixbyte crystal structure of indium oxide (a). Oxygen atoms occupy two different Wyckoff position labeled, 8b where indium atoms are equidistant from oxygen atoms and 24d where indium atoms have three different distance from oxygen; oxygen atoms occupy the 48e Wyckoff position (b). Face-diagonal and body-diagonal placements of the oxygen vacancies for 24d site and 8b site (c).....40

Figure 2.7: Spectral normal reflectance R and transmittance T computed from a quantitative theoretical model for the optical properties of ITO.41

Figure 2.8: In_2O_3 conduction band upon Sn doping (a) and TM doping (b).....44

Figure 2.9: Schematic diagrams of band structures for type-I (a), type-II (b), and type-III (c) TM-doped In_2O_3 . The Fermi Energy (E_F) is represented by a dashed line.45

Figure 3.1: schematic representation of the sputtering mechanism. Energetic ions, usually Ar^+ , hit the atoms of the coating materials, ejecting them from the target.48

Figure 3.2: Magnetron Sputtering system. The addition of a magnetic field increases the length path of electrons, leading to an increase of the ionization of the sputtering.....50

Figure 3.3: schematic of the RBS measurement and experimental set-up. Energetic He^+ ions with mass, energy and velocity M_1 , E_0 and v_0 bombard the sample's atoms with mass, energy and velocity M_2 , E_2 and v_2 . During elastic collision between the energetic ions and the nuclei of the sample's atoms, the ions are reflected backward and collected by a detector.52

Figure 3.4: Experimental set-up for the collection of RBS spectra.53

Figure 3.5: schematic representation of photoelectrons emission. X-ray photons determines the emission of electrons from the core level of the atoms.54

Figure 3.6: binding energy reference diagram for XPS experimental set-up.55

Figure 3.7: XRD experimental set-up.....56

Figure 3.8: Bragg's law diagram.57

Figure 3.9: Experimental set-up for AFM microscopy.....58

Figure 3.10: The effect of tip-to-sample distance on the force interaction between tip and sample.59

Figure 3.11: Electronic energy levels of the sample and AFM tip for the three different steps of the experiment. The tip and sample are separated by distance d with no electrical contact (a); the tip and sample are in electrical contact (b), and (c) an external bias (V_{dc}) is applied between tip and sample to nullify the tip-sample electrical force. E_v is the vacuum energy level. E_{F_s} and E_{F_t} are Fermi energy levels of the sample and tip, respectively.60

Figure 3.12: Schematic representation of KPFM modes measurements: (a) Amplitude modulation mode and (b) Frequency modulation mode. Both AM and FM modes maintain constant tip-sample separation. AM mode uses oscillation amplitude changes as a feedback signal while FM modes uses oscillation frequency change as feedback.62

Figure 3.13: Scanning Electron Microscope components.63

Figure 3.14: Beam-specimen interaction volume and signals produced as a function of the electron penetration-depth.64

Figure 3.15: Spatial distribution of backscattered electrons, and secondary electrons of the I, II and III type. 65

Figure 3.16: Resistivity measurement in Van Der Pauw configuration. The current is injected between two contact and the voltage difference measured on the two remaining. The same is repeated for six possible permutations of the indices. ... 67

Figure 3.17: Hall effect measurements configuration. 68

Figure 3.18: Double-beam spectrophotometer components. 70

Figure 3.19: Tandem solar cell scheme (a); schematic representation of the bifacial Si-HJT solar cell (b). 71

Figure 3.20: Experimental set-up for EQE measurements. 73

Figure 4.1: RBS spectrum in semi-log scale of the as-deposited ITMO sample. Only the RBS region of Sn, In and Mo signals is shown for clarity. Arrows indicate the position of the elements at the surface. 78

Figure 4.2: RBS spectra of He⁺ ions backscattered by ITMO samples as deposited and after annealing at 200 °C, 300 °C, 400 °C and 500 °C for 1h. Continuous lines are the output of the SimNra simulation program used to calculate the atomic areal density of the chemical elements. 79

Figure 4.3: XPS spectra of Mo 3d region in as deposited (a) and 400 °C annealed (b) ITMO samples. 80

Figure 4.4: Sn and In 3d peaks before (black) and after (red) thermal annealing normalized at the same Sn intensity. 82

Figure 4.5: Optical transmittance spectra (a, c) and Tauc Plot (b, d) of ITMO and ITO films. The average values of transmittance in the visible range and the values of the optical energy gap are reported within the figures. 83

Figure 5.1: RBS experimental Spectra and Simulated curves with SimnNra software for IZrO 40 nm thin films with different Zr at% as-deposited compared with 40 nm In₂O₃ film simulated spectra. 91

Figure 5.2: RBS experimental Spectra and Simulated curves with SimnNra software for IZrO thin films as-deposited with Zr = 0.6 at% for different thickness. 92

Figure 5.3: XRD Pattern for as-deposited and annealed IZrO films for different thickness. 93

Figure 5.4: AFM images (3µm x 3µm) of IZrO thin films for different thickness as deposited: (a) 15nm as-deposited, (b) 40nm as-deposited, (c) 90nm as-deposited, and after annealing: (d) 15 nm +A, (e) 40 nm +A, (f) 90 nm + A. 95

Figure 5.5: Surface morphology and surface potential maps from FM-KPFM measurements for IZrO films with different Zr at%: 0 at% (a.1-a.2), 0.6 at% (b.1-b.2), 0.8 at% (c.1-c.2), 0.9 at% (d.1- d.2). 97

Figure 5.6: IZrO thin films resistivity for different Zr at% of 0.6 at%, 0.8 at% and 0.9 at% with a fixed thickness of 40nm, before and after post-deposition thermal annealing compared with ITO reference from literature.98

Figure 5.7: IZrO thin films mobility and carrier concentration for different Zr at% of 0.6at%, 0.8at% and 0.9at% with a fixed thickness of 40nm, before and after post-deposition thermal annealing.99

Figure 5.8: Activation Rate for different Zr at% of 0.6 at%, 0.8 at% and 0.9 at% with a fixed thickness of 40 nm, before and after post-deposition thermal annealing..... 100

Figure 5.9: Activation Rate for different IZrO thickness of 15 nm, 40 nm, and 90 nm with a fixed Zr = 0.6 at%, before and after post-deposition thermal annealing. 101

Figure 5.10: Transmittance spectra of IZrO thin films for different thickness of 90 nm, 40 nm, and 15 nm with a fixed Zr = 0.6 at%, before and after post-deposition thermal annealing..... 102

Figure 5.11: Transmittance spectra of IZrO thin films for different Zr at% of 0.6 at%, 0.8 at% and 0.9 at% with a fixed thickness of 40nm, before and after post-deposition thermal annealing. 102

Figure 5.12: Tauc Plot of IZrO thin films for different Zr at% of 0.6 at%, 0.8 at% and 0.9 at% with a fixed thickness of 40 nm, before and after post-deposition thermal annealing..... 104

Figure 5.13: Tauc Plot of IZrO thin films for different thickness of 15 nm, 40 nm, and 90 nm with a fixed Zr = 0.6 at%, before and after post-deposition thermal annealing..... 104

Figure 5.14: Top view SEM images of 90 nm IZrO deposited on top of rear bifacial SHJ solar cell at different magnification (a),(b), and Bifacial rear-junction Silicon Heterojunction solar cell (astructure supplied by Enel 3sun in the aim of the BEST4U project with IZrO electrodes deposited as aim of this work..... 105

Figure 5.15: EQE data on the SHJ solar cell with 90nm IZrO thickness after annealing deposited as front and back contacts compared with EQE on SHJ solar cell with ITO deposited by Enel 3SUN as front and back contact after annealing. 106

1. Introduction

1.1. Renewable energy sources

The energy problem represents one of the most critical issue of this century. The reason why energy is so important is linked to its key ability to solve all of the other problems. Energy determines the quality of our environment, prevents disease, provides clean water over a long distance, and strongly impacts the prosperity of our society.

Abundant, low-cost, and clean energy sources are essential also to guarantee the energy transition of the global energy sector from fossil-based to zero-carbon by the second half of this century.

Up to now, the climate is warming up, as shown in Figure 1.1 where the evolution of the five-year average annual temperature of all countries around the globe is reported^{1,2}. Normal-temperature, lower and higher temperature areas are represented by white, blue, and red colored regions respectively. The evolution shows how blue regions fade away to move over marked red areas over the years. Global warming continues to accelerate, and the humankind is responsible for this phenomenon, whose catastrophic impacts on the society are more and more perceptible.

The emission of greenhouse gases contributes to the climate warms up. A greenhouse gas absorbs and emits energy in the infrared range. The main greenhouse gas in the earth's atmosphere is water vapor, whose origin is natural, then there are the anthropogenic greenhouse gases: carbon dioxide (CO₂) produced by fossil-fuel combustion, methane (CH₄) from agriculture, and nitrous oxide (N₂O) from fossil-fuel combustion.

The International Energy Agency (IEA), in the September 2020 World Energy Outlook, established The Net Zero Emissions by 2050 Scenario (NZE). This normative shows a narrow, but achievable, pathway for the global energy

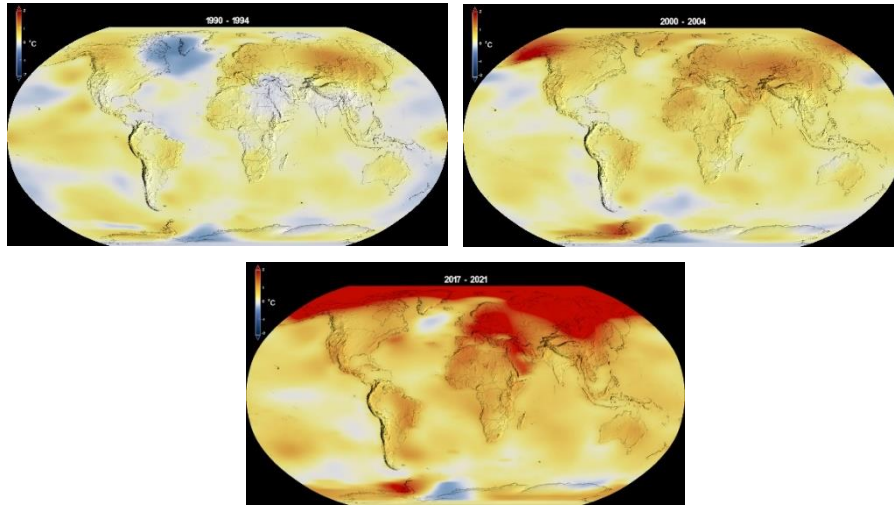


Figure 1.1: mean anomaly of surface temperature for (a) 1990-1994 , (b) 2000-2004 (b), and (c) 2017-2021 five-years range ^{1,2}.

sector to achieve net zero CO₂ emissions by 2050. This scenario also meets key energy-related United Nations Sustainable Development Goals (SDGs), in particular, by achieving universal energy access by 2030 and major improvements in air quality. This is consistent with limiting the global temperature rise to 1.5 °C in line with reductions assessed in the IPCC in its Special Report on Global Warming of 1.5 °C ³⁴.

Renewable energies play a crucial role in the energy transition to mitigate climate change and to reduce greenhouse gas emissions. Renewable energies are wind, solar, hydropower, biomass, and geothermal. Renewable energy compared to fossil fuel produce less CO₂ and other greenhouse gases, but not all the renewable energies are also carbon-free and every energy supply system has a different carbon footprint. Figure 1.2 shows the grams of CO₂ emitted for kW/h for different renewable energy sources. Low carbon technologies have a lower carbon footprint compared to fossil energy technologies, however, some renewable energy sources, such as solar and wind have almost 5-10 times less emitting rather than for example biomass energy.

Wind and solar energy have experienced remarkable growth and huge cost improvements over the past decade with no sign of slowing down. Renewable energy is becoming extremely competitive versus fossil fuels all around the World.

In 2000, the United Nations Development Programme, UN Department of Economic and Social Affairs, and World Energy Council published an estimate of the potential solar energy that could be used by humans each year, taking into

account several factors such as insolation, cloud cover, and the land usable by human kind. The estimate was a global potential of 1,600 to 49,800 EJ solar energy per year, which is several times higher compared to the total world energy consumption, which was 598 EJ in 2018 ⁵.

Photovoltaic cells convert solar energy into electricity. Increasing the conversion power efficiency (CPE) of solar cells is a key goal of research. Multiple factors in solar cell design play roles in limiting the solar cell's ability to convert the sunlight received. The following paragraphs will summarize, with a short overview, the most relevant PV technologies, focusing on c-Si technology and Silicon Heterojunction Solar Cells (SHJ) architecture. Each layer in the complete stack plays a specific role in the conversion efficiency and optimization of solar cells. One of these layers, the Transparent Electrode (TE), allows light to enter the absorber layer and to collect the photo-generated carriers. Materials commonly used for TE will be presented together with specific properties required for PV applications.

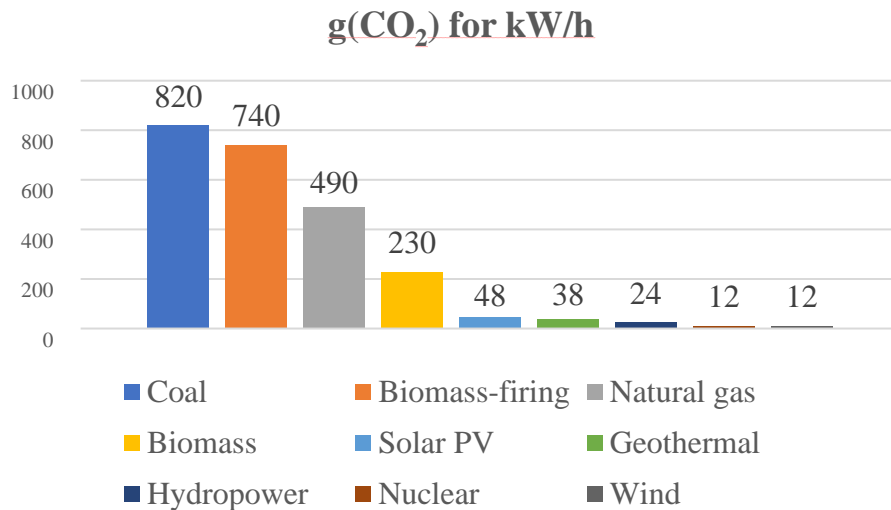


Figure 1.2: grams of CO₂ emitted for kW/h for different renewable energy.

1.2. PV Technologies

In 1839, using an electrochemical cell, Edmond Becquerel demonstrated “the production of an electric current when two plates of platinum or gold immersed in an acid, neutral, or alkaline solution is exposed in an uneven way to

1.2 PV Technologies

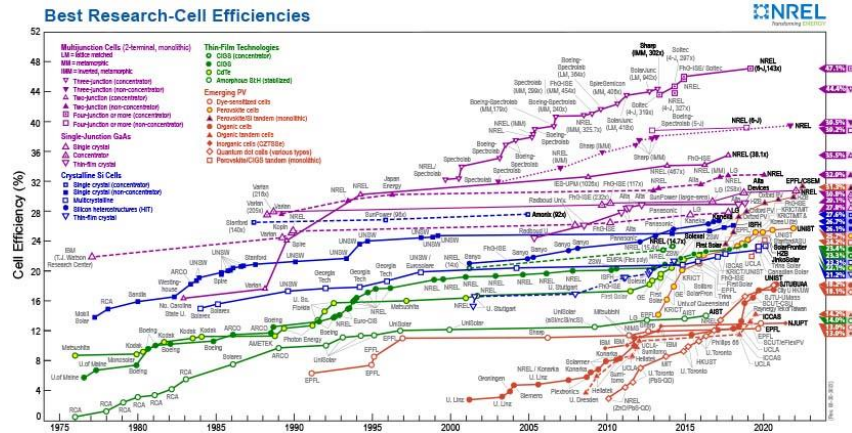


Figure 1.3: conversion efficiencies for different photovoltaic technologies, plotted from 1976 to 2022. This plot is courtesy of the National Renewable Energy Laboratory, Golden, CO ⁸.

solar radiation". This was the first demonstration of the photovoltaic effect ⁶. The first solar cell experienced by Charles Fritts in 1884 consisted of a layer of selenium covered with a thin film of gold and showed an efficiency of 1% ⁷.

Nowadays, solar cells are made of several semiconductor materials, with different geometries, and efficiencies from 13% to 47%. Figure 1.3 shows an overview of the existent PV technologies and their efficiency plotted from 1976 to 2022⁸. Commercial technologies include wafer-based crystalline silicon (c-Si) solar cells, thin film technologies of copper indium/gallium disulfide/diselenide (CIGS), cadmium telluride (CdTe), and multijunction technology using III-V semiconductor as GaAs and InGaP. Organic, dye-sensitized solar PV devices, Quantum Dot PV, and Perovskite-based solar cells are considered novel and emerging technologies.

1.2.1. Wafer-based crystalline silicon solar cells

Wafer-based crystalline silicon (c-Si) is the dominant PV solar cell technology. In the last 10 years the average efficiency of commercial wafer-based silicon modules increased from about 15% to 24% and more.

Different c-Si solar cells exist, broadly distinguished by the type of silicon processing and doping (p- or n-type), poly-crystalline or monocrystalline form, and the type of contacting used to extract current.

Aluminum diffused back-surface field cells (Al-BSF) represent almost 80% of the market. This is the standard technology used on p-or n-type, poly, or monocrystalline wafers. An evolution of the traditional Al-BSF technology with a fully covered back aluminum surface is represented by the passivated emitter and rear contact cell (PERC) introduced by Blakers et al. in 1989⁹, with the addition of a rear surface passivation layer. In 1999, the passivated emitter and rear locally diffused solar cell (PERL)¹⁰ further developed the concept of PERC architecture. However, to reduce the carrier recombination, promising options are represented by solar cells with carrier selective passivating contacts (CSPCs) including silicon heterojunction solar cells (SHJ) and c-Si solar cells with tunnel-oxide passivated contacts.

To further increase the efficiency, silicon-based tandem solar cells have been proposed. The absorber material, c-Si in this case, has a bandgap energy of 1.12 eV, and only photons with higher energy can be absorbed. The two main spectral losses in solar cells are represented by photons with lower and much higher energy values than the c-Si energy bandgap. Excess energy is released as heat into the absorber, while photons with lower energy than the bandgap are not absorbed. Tandem solar cells, combine two or more solar cells with different bandgap, so capturing and converting part of the energy that would otherwise be dissipated through the relaxation process. The next evolutions for the traditional solar panels are bifacial modules, where the total energy generation is increased by allowing the light to be collected by both sides of the wafer. The bifacial solution has several advantages as, for example, the reduction of metal consumption due to the reduction of the metal rear area. The schematic architecture of some PV technologies reported in the paragraph is shown in Figure 1.4

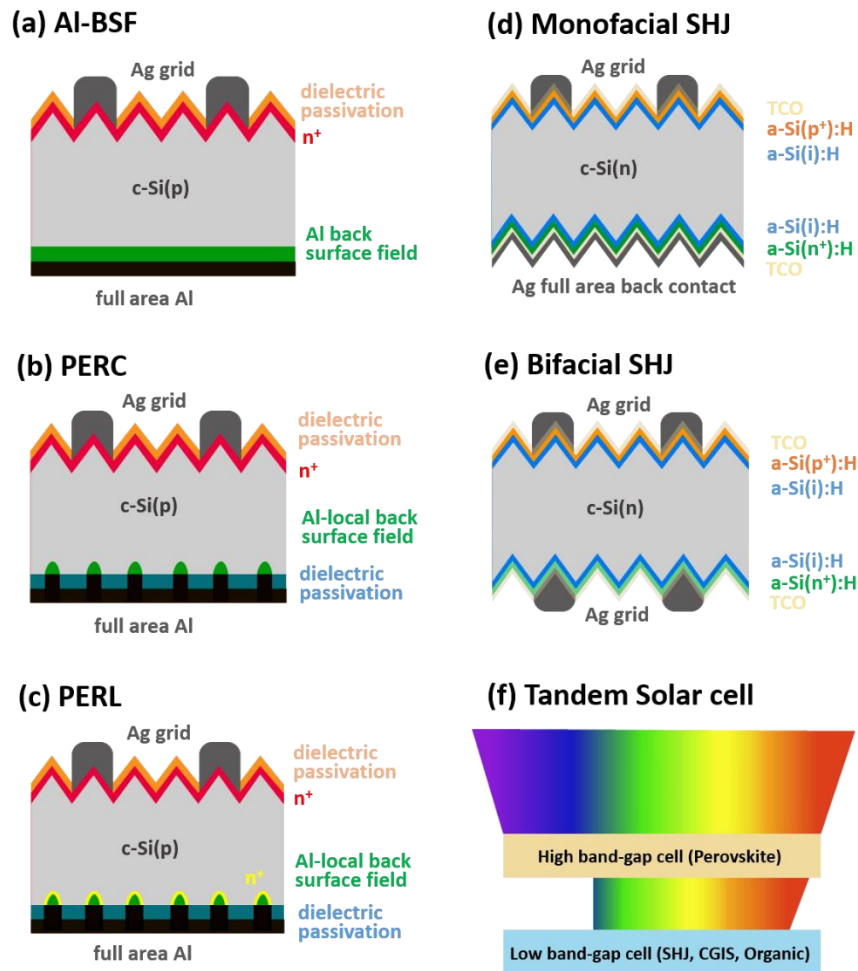


Figure 1.4: schematic representation of different solar cells architecture: (a) Al-BSF; (b) PERC; (c) PERL; (d) Monofacial SHJ; (e) Bifacial SHJ; (f) Tandem.

1.2.2. SHJ solar cell design and TCO functions

Silicon Heterojunction solar cell technology is an attractive technology for large-scale production of solar cells with a power conversion efficiency (PCE) record of 26.5% reached by LONGYI Chinese PV module maker in June 2022. The most relevant features of SHJ solar cells are very high efficiency and a relatively simple production sequence. Thin wafers can be utilized, saving costs and energy due to low-temperature processes ($< 200\text{ }^{\circ}\text{C}$) and no stress-induced wafer bending and cracking avoided by symmetrical deposition processing. In

SHJ solar cells, photons transmitted by TCO and a-Si:H are absorbed by the Silicon wafer. Photo-generated electron-hole pairs are separated by an electric field and extracted by carrier selective transportation layers. The properties of each part of SHJ solar cells (silicon bulk, passivation layers, and carrier selective transportation layers) will be described following in the section.

For SHJ solar cell fabrication, c-Si (100) substrates are generally used. The wafer is first cleaned and etched to remove the SiO₂ native layer and textured with an alkaline solution to obtain Si(111) faceted pyramids. The highest efficiency SHJ solar cells, up to now, are obtained using n-doped c-Si wafers rather than p-type doped silicon wafers, mainly due to the minority carrier lifetime for p-type c-Si.

After the cleaning and texturing process, intrinsic hydrogenated amorphous silicon layers (a-Si:H(i)) are deposited by chemical vapor deposition (CVD) to passivate dangling bonds. This is a way to reduce the density of interface states and prevent interface losses.

Heavily p- and n-doped a-Si:H layers are then deposited by plasma-enhanced chemical vapor deposition (PECVD) to selectively collect photogenerated electrons and holes. Selective contacts ensure high (low) conductivity for the majority (minority) carriers reducing the minority carrier density close to the interface and preventing (or limiting) the formation of interface state at the absorber/contact interface.

On top of the passivating layers and the carrier selective transport layers in SHJS, there are Transparent Conductive Oxide (TCO) layers, a specific type of TE, with the function of being deposited as Transparent Electrodes by sputtering to provide lateral conductivity towards the metal screen printed Ag electrodes.

The function of TCO is crucial in amorphous/crystalline silicon solar cell design. An ideal TCO should have a low sheet resistance to provide sufficient lateral conductivity towards the electrodes to transport the photo-generated electrons to external device terminals. At the front (for monofacial) or front/rear (for bifacial) of SHJ, the TCO layers act as optically transparent electrodes that ensure the transmission of photons in the wavelength region of interest (normally 350-1100 nm) into the absorber of the solar cell. Low contact resistance with adjacent layers, appropriate refractive index, and thickness are also required to maximize the light in-coupling in the solar cell. The solar cell performance is therefore strongly influenced by TCO electrical properties such as carrier concentrations, carrier mobility, and resistivity, but also by optical parameters such as transmittance and reflectance.

The TCOs work function play also an important role to guarantee the lateral conductivity of the TCO. It should match the work function of the adjacent passivation layer. For an SHJ solar cell, low TCO work functions are used on top

of the a-Si(n⁺) passivation layer ($W_F = 4.58$ eV) and high TCO work functions are placed on top of the a-Si(p⁺) passivation layer ($W_F = 5$ eV).

1.3. Transparent Electrodes for PV applications

Materials used as Transparent Electrode can be classified into four big categories:

- Transparent Conductive Oxide
- Thin Metal layer and emerging Nanomaterials
- Transparent Conductive Polymers
- Two-dimensional Materials

1.3.1. Transparent Conductive Oxide

Transparent Conductive Oxides are highly doped (degenerate) metal oxides. Tin oxide (SnO₂), indium oxide (In₂O₃), cadmium oxide (CdO), zinc oxide (ZnO), titanium oxide (TiO₂), and gallium oxide (Ga₂O₃) are well-known binary compounds whose electrical conductivity can be improved introducing some doping elements. The first TCO material, Cadmium Oxide (CdO) was introduced by Baedeker in 1907, using thermal oxidation of sputtered cadmium metal thin films, followed by In- and Sn- doped CdO (CdIn₂O₄, CdSnO₃) thin films. The lowest resistivity for Cd-based TCO reported was 10⁻⁴ Ωcm with a transmittance of 85%-90% in the visible range¹¹. However, Cd toxicity makes these compounds less desirable for practical applications.

Tin-doped Indium Oxide (In₂O₃:Sn) or ITO, is the most common TCO used as a transparent electrode in photovoltaic devices. Commercial ITO thin films have a Sheet Resistance of 20 – 10 Ω/□ for 100- to 300- nm thick films and typical optical transmittance of 90% or higher in visible (VIS) and near-infrared (NIR) range. However, ITO presents several drawbacks for large-scale applications. First, Indium is classified as a critical material. The scarcity of global indium resources associated with its rising cost is one of the greatest concerns of the last decay. In addition, low NIR transmittance, brittleness, and occurrence of cracks under mechanical stress, and lastly limited application in flexible optoelectronic devices. The sputtering process for ITO coating is typically conducted at high temperatures whereas, when a flexible plastic substrate is used, ITO is preferably deposited at lower temperatures to prevent any damage to the substrate, with the corresponding increase of the sheet resistance. To develop flexible optoelectronic devices and meet the increasing demand for Indium there is a requirement to replace ITO with a better alternative TE. Among TCO, doped ZnO materials have been proposed as suitable TCOs, aluminum doped zinc oxide

(AZO) for example, represents a promising green material. Zn is a non-toxic, abundant material and AZO films show very high transparency, up to 91.2%. However, its poor electrical conductivity keeps this material still far from industrial applications. Zinc-doped indium oxide (IZO), is another TCO also widely reported with high mobility values of about $60 \text{ cm}^2\text{V}^{-1}\text{s}^{-1}$ ^{12,13}. This material has excellent optoelectronic properties already in its as-deposited state and it is not affected by post-deposition thermal annealing. However, the significant indium ratio in IZO films raises the issues of indium supply which became one of its possible drawbacks together with its typically amorphous nature and its band gap narrowing with consequent parasitic absorption in the UV-vis range.

Novel TCO used as front contacts in solar cells are also hydrogen-doped In_2O_3 , (IO:H)¹⁴ and cerium/hydrogen or tungsten/hydrogen co-doped In_2O_3 (ICO:H, IWO:H respectively). They offer very low optical absorptance, below 2% from 400 nm up to 1200 nm, and carrier mobility higher than $100 \text{ cm}^2\text{V}^{-1}\text{s}^{-1}$ ¹⁵. One of the challenges of upscaling these hydrogenated doped oxides is to control the introduction of water molecules, to introduce H, during the deposition. Water vapor can diffuse within the devices and may degrade their performance.

Recently, multilayer structures TCO/metal/TCO¹⁶⁻¹⁸ have been reported, AZO/Ag/AZO, ITO/Ag/ITO¹⁷, and other combinations showed optimal sheet resistance R_{sheet} due to the presence of metal layers which however affect the optical properties with reflectance losses.

1.3.2. Thin metal layer and emerging nanomaterials

The metal layers can serve as TCs if they contain holes, are sufficiently thin, or combine these features. Thick Au films of 100-180 nm with sub-wavelength holes array show peak values of transmittance up to 50%, which however is still too low for energy-related applications¹⁹⁻²¹. For the metal-film thickness of only a few tens of nanometers, these materials offer excellent electrical properties and they are thin enough to show some transparency. Very thin layers of Cu, Ag, or Au are the simplest way to perform TEs^{22,23}. Thin Ag films are the best option for their lowest values of absorptance.

Unfortunately, when metals are deposited on glass or some other dielectric material, they are reasonably uniform only at thickness above 10 nm, which is far from the optimal thickness for an idealized TEs. The formation of non-uniform structures at small thickness leads to high reflectance at long wavelengths²³.

Superior properties can be achieved by adding layers that led to dielectric/metal/dielectric stacks to anti-reflective treat the metal, such as $\text{TiO}_2/\text{Ag}/\text{TiO}_2$ ²⁴, $\text{ZnO}/\text{Ag}/\text{ZnO}$ ^{25,26}, and $\text{ZnO}/\text{Cu}/\text{ZnO}$ ^{27,28}.

To take advantage of the high metallic conductivity, metal nanowire (NWs) network grids have been proposed^{29,30}. The electrical properties of such transparent electrodes depend on the network density. Sufficiently sparse grids may avoid losses in transparency. High-quality nanowires can be realized with a high aspect ratio and good crystalline quality: no defect to avoid electron scattering and no nanoparticle formation within the wire to avoid plasmonic absorption³¹. Common challenges with the NWs network include poor chemical stability, oxidizing issues, large surface roughness, and high contact resistance^{32,33}.

1.3.3. Transparent Conductive Polymer

Conducting polymers are organic materials with characteristic high transparency and electrical conductivity. They are more advantageous compared to other electrode materials due to their mechanical flexibility, lightweight, and excellent compatibility with plastic substrates. In the 1980s a broad range of commonly available polymers (polypyrrole, polyaniline, polythiophene, etc.) was found to exhibit significant electrical conductivities with the addition of p- or n-dopants. Polyaniline (PANI), polypyrrole (PPY) and, poly (3,4-ethylenedioxythiophene):poly (4-styrenesulfonate) (PEDOT:PSS) are the three most important conducting polymers^{34,35}. The elevated conductivity results from the formation of polaron and solution species formed through the doping process. However, these polymers show very poor electrical stability when exposed to high temperatures, humidity, or UV light.

1.3.4. Two-dimensional materials

Two-dimensional (2D) materials have been widely proposed as transparent electrodes. Their atomic monolayer structure allows high optical transmittance. Among these, graphene is the leading material. A monolayer of graphene can reach mobilities above $10000 \text{ cm}^2\text{V}^{-1}\text{s}^{-1}$ for free-standing graphene flakes obtained by mechanical exfoliation^{36,37}. However, defects that lower the carrier mobilities are introduced during upscaling processes limiting their application on large area substrates³⁸.

Among these different types of TE, the next chapter will focus on the TCO category. The electronic structure and the electrical and optical properties will be described with particular attention for In-based TCO.

2. TCO Fundamentals

2.1. Introduction

Transparent Conductive Oxides (TCOs) are an important component of flat panel displays, low emissivity windows, electrochromic devices, transparent electronics, and photovoltaic devices, where they can act as transparent electrodes, diffusion barriers, and structural templates³⁹. Although electrical conductivity and optical transparency are conflicting properties, TCOs represent an optimal trade-off between these two characteristics. They show simultaneously high optical transmission in the near-infrared and visible range, and high electrical conductivity⁴⁰. The current TCO industry is based on few materials. The two dominant markets for TCOs includes fluorine-doped tin oxide (FTO), most often used for energy-efficient windows, and indium tin oxide (ITO) used in the majority of flat panel display and solar cells. However, the volume of flat panel displays and hence the volume of ITO coatings, rapidly grows. Industrial issues for current applications are the driving forces for scientific research and the development of new materials for devices with improved performances. Higher conductivity and transparency are the most important goals, this requiring a deep understanding of the relationships between the structure and the electro-optical properties of these materials^{39,41,42}. To this purpose, the chapter describes the basic electronic structure and the electrical and optical properties of TCOs along with an overview of the main characteristics and results of indium-based TCOs. Among the different dopants generally used for In_2O_3 to form *n*-type materials, transition metals doping mechanism and defect levels formation will be proposed⁴³.

2.2. Electronic structure

TCOs are obtained by doping transparent oxides, which are insulator or semiconductor materials at room temperature in their undoped states. To become conductive, the oxide must be highly-doped by increasing the free-carrier concentrations, until the Fermi-level enters into the conduction band. Hence, to understand the nature of the conductivity of TCOs, it is necessary to review the band structure of semiconductors and their doping mechanism. The formation of energy bands and doping will be here briefly described.

2.2.1. Energy band structure of semiconductors

The band structure of a crystalline solid, which is represented by the energy-momentum (E - k) dispersion relationship is usually obtained by solving the Schrödinger equation of one-electron approximation. For semiconductor materials, there is a forbidden energy range, called energy gap, in which allowed states cannot exist. Energy regions or bands are permitted only above or below this energy gap. The upper bands are called conduction bands; the lower bands are the valence bands. The bandgap energy E_g , is defined as the separation between the energy of the bottom of the conduction band and the top of the valence band⁴⁴. Near the edges, the E - k relationship can be approximated by the quadratic expression:

$$E(k) = \frac{\hbar^2 k^2}{2m^*} \quad (2.1)$$

where m^* is the associated *effective mass*. The concept of effective mass comes from the statement that an electron in a crystal may behave as if it had a different mass from the free-electron mass m_0 , as a result of the periodic potential. The effective mass is a tensor quantity with component m_{ij}^* defined as:

$$\frac{1}{m_{ij}^*} = \frac{1}{\hbar^2} \frac{\partial^2 E(k)}{\partial k_i \partial k_j} \quad (2.2)$$

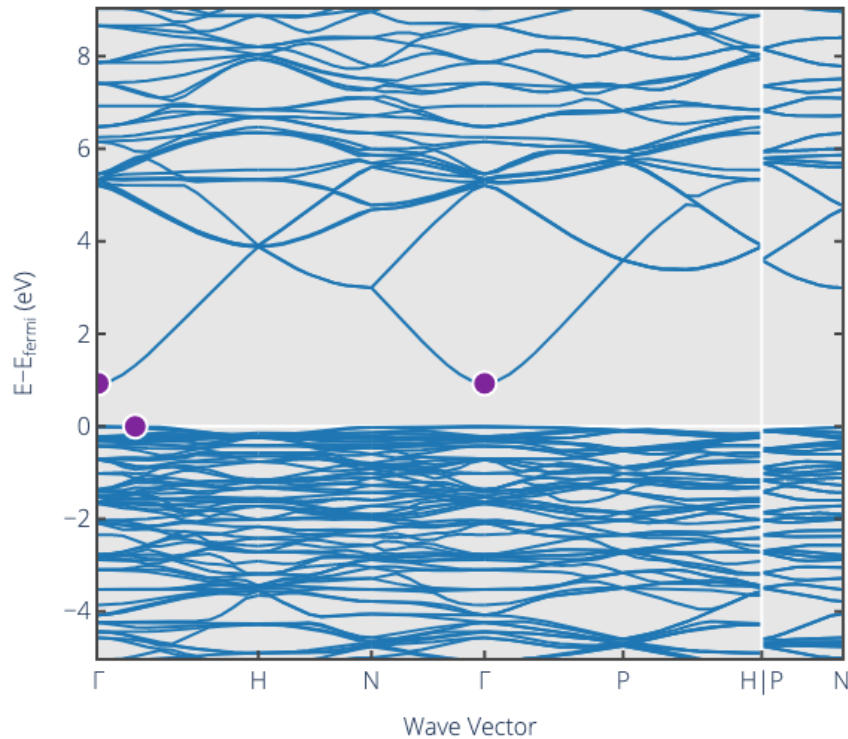


Figure 2.1: Calculated band structure of In_2O_3 ⁴⁵.

Theoretically is inversely proportional to the curvature of the energy band. The smaller the effective mass value, the sharper the curvature of the band in the E versus k plot. The E - k curve is concave at the bottom of the conduction band, so m^* is positive, whereas is convex at the top of the valence band, thus m^* here results negative. The particle in that state will be accelerated by the field in the opposite direction expected for negatively charged particles. This means these particles, called *holes*, behave as if they have a positive charge. Hence, the electron in a crystalline solid, will move like a free-particle with mass m^* , which is related to the curvature of the band. Figure 2.1 shows the band structure of In_2O_3 as an example⁴⁵.

2.2.2. Doping mechanism of semiconductors

A semiconductor can be doped with different types and concentrations of impurities to improve the electrical conductivity. The doping mechanism can occur in two different ways. Some impurities, named donors, can contribute with

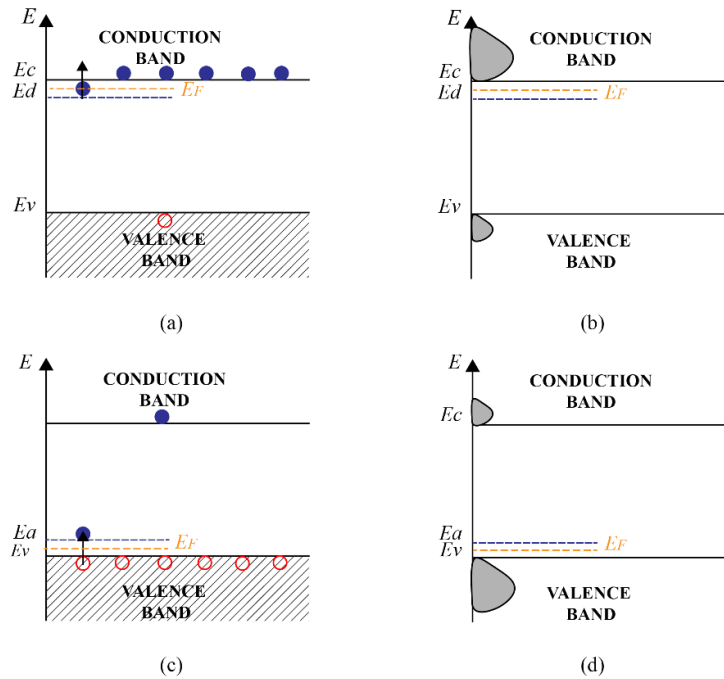


Figure 2.2: schematic representation of doping mechanism and defect levels position for n-type (a) and p-type (c) semiconductors. Density of states for n-type (b) and p-type (d) semiconductor upon doping. The green dashed lines represent the Fermi.

free- *electrons* in the conduction band (*n*-type semiconductor), while others called acceptors, may create deficiency of electrons, called *holes* in the valence band (*p*-type semiconductor). Doping will introduce energy levels that lie within the band gap. In *n*-type semiconductors, these levels are below the conduction band, while for *p*-type semiconductors they are above the valence band. Upon doping, the Fermi level can shift from its original position (in the middle of the bandgap for undoped semiconductors) in two different directions depending on the types of impurities introduced:

- with donor impurities, the Fermi level shifts to a point between the defect level and the conduction band. Hence, the electrons from the defect levels can be easily excited into the conduction band because the magnitude of the impurity ionization energy for shallow impurities (whose levels are close to the band edges) is comparable to the thermal energy $k_B T$.
- with acceptor impurities the Fermi level shifts and move between the valence band and the acceptor level. Electrons from the valence band neutralize the empty defect level leaving

extra holes in the valence band.

Figure 2.2a-d shows a schematic representation of n -type and p -type semiconductor doping mechanisms respectively and their relative density of state upon doping. The density of states (DOS) is a representation of the number of different states at a particular energy level that an electron is allowed to occupy. The DOS is higher in the conduction band for n -type semiconductors, whereas for p -type semiconductors is higher in the valence band.

2.2.3. Carrier-Transport phenomena

When exposed to an external force the electrons acquire a net drift velocity. The drift velocity v_d , is proportional to the strength of the electric field E and the proportionality constant is the *carrier mobility*, μ :

$$v_d = \mu E \quad (2.3)$$

For semiconductors with both electrons and holes as carriers, the drift velocity gives rise to an electric current whose density is given by:

$$J = q(\mu_n n + \mu_p p)E \quad (2.4)$$

where q , n , and p represent the electric charge and the electrons and holes carrier density respectively. Ohm's law defines the conductivity of a material and the relation between the current density, and the strength of the electric field $J = \sigma E$ results linked to the carrier mobility.

$$\sigma = q(\mu_n n + \mu_p p) \quad (2.5)$$

The family of TCOs is dominated by n -type semiconductors. Hence, in the whole section, the electrical and optical properties of semiconductors will be described by referring to n -type. When the majority of carriers ($n \gg p$) are electrons the conductivity can be simplified as:

$$\sigma = q\mu_n n \quad (2.6)$$

The mobility in semiconductors is affected by different scattering

mechanisms and it is related to the scattering time τ_m , as shown in eq. 2.7, defined as the average time between two consecutive scattering events in which carriers are forced to change their direction and/or energy.

$$\mu = \frac{q\tau_m}{m^*} \quad (2.7)$$

Conduction electrons can be scattered by several different mechanisms, such as ionized impurities, lattice defects (dislocations, grain boundaries, vacancies), and lattice vibrations. These scattering processes decrease the overall conductivity by reducing the scattering time τ_m . The total scattering probability is the sum of the probability of every single scattering mechanism:

$$\frac{1}{\tau} = \sum_i \frac{1}{\tau_i} \quad (2.8)$$

where τ_i is the mean scattering time considering the i th scattering process alone.

Equation. 2.8. can be rewritten in terms of mobility and it is known as Matthiessen's Rule ^{46,47}:

$$\frac{1}{\mu} = \sum_i \frac{1}{\mu_i} \quad (2.9)$$

At low electric fields, ionized impurity scattering and phonon scattering are predominant. In phonon scattering, short or long wavelength oscillations of atoms produce a dipole moment and small displacements of tens to thousands of atoms.

The ionized impurities are strong scattering centers for charge carriers and can significantly affect mobility. The mobility from ionized impurities μ_i decrease with increasing carrier concentration n .

For polycrystalline films, scattering by grain boundaries may be considered. Polycrystalline thin films are composite crystallites separated by grain boundaries, which are transitional regions between different orientation crystallites. Grain boundaries contain lattice defects-induced trapping states that compensate a fraction of charge carriers of ionized impurities. This process creates a potential barrier that limits the carrier mobility and the motion from one crystallite to another. The grain boundary scattering becomes relevant only when the mean free path of electrons is comparable with the grain sizes. For degenerate

semiconductors, the mean free path of electrons is much smaller than the grain sizes, hence the contribution of this scattering mechanism is much smaller compared to the others^{12,48}.

2.3. Optical Properties

The optical properties of a semiconductor are characterized by the complex refractive index:

$$\bar{n} = n_r - ik_e \quad (2.10)$$

The real part of the refractive index n_r , is linked to the propagation velocity of the electromagnetic radiation in the medium:

$$n_r = \frac{c}{v} \quad (2.11)$$

while the imaginary part k_e , the extinction coefficient determines the absorption coefficient:

$$\alpha = \frac{4\pi k_e}{\lambda} \quad (2.12)$$

The absorption coefficient in a semiconductor is a function of the photon energy. Near the absorption edge, the absorption coefficient can be expressed as:

$$\alpha \propto (hv - E_g)^\gamma \quad (2.13)$$

where hv is the photon energy, E_g is the energy gap and γ is a constant. The band-to-band transition can be classified into two main types: direct and indirect. For direct band gap materials, the minimum of the conduction band equals in k the maximum of the valence band (Figure 2.3a). For indirect bandgap materials, in which the minimum of the conduction band has a different k value from the maximum of the valence band, transitions are involved to absorb (Figure 2.3b) or emit phonons (Figure 2.3c) to conserve the momentum. The absorption coefficient can be modified as:

$$\alpha \propto (h\nu - E_g \pm E_p)^y \quad (2.14)$$

where E_p represents the phonon energy acquired or released to allow the transition.

In the case of TCO, the carriers introduced by the doping mechanism, shift the absorption edges to higher energy sides (UV region), apparently enlarging the energy gaps, hence the short wavelength cut-off. This variation is attributed to the occupation of the conduction band by conduction electrons. This band filling led to higher values of energy needed for the optical transition. This energy shift is called the *Moss-Burstein* effect (Figure 2.4), and it is described by the following equation:

$$\Delta E_g^{MB} = \frac{\hbar^2}{2m^*} (3\pi^2 n)^{3/2} \quad (2.15)$$

where ΔE_g^{MB} is the increase of the optical bandgap and n is the electron density. The carrier concentration influences the optical window of the semiconductor not only on the UV side but also on the long-wavelength (IR) edge.

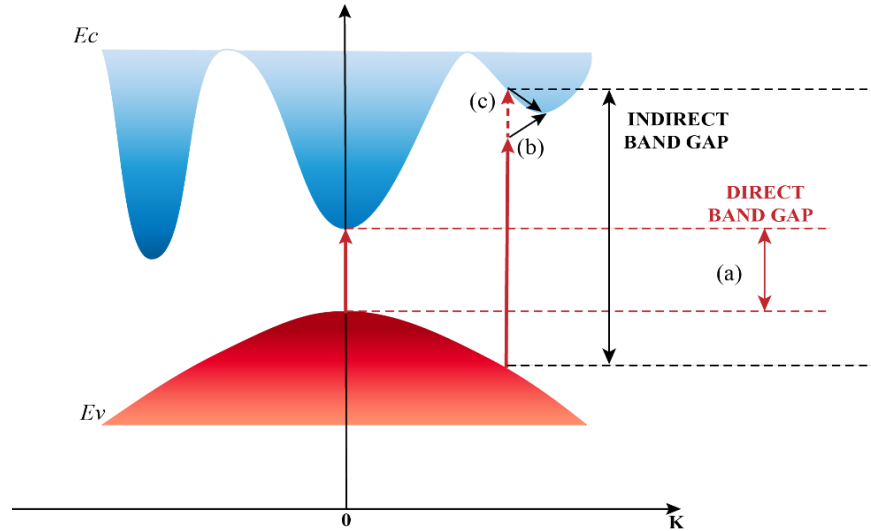


Figure 2.3: Optical transitions: direct transition (a); indirect transition involving phonon absorption (b) and phonon emission (c).

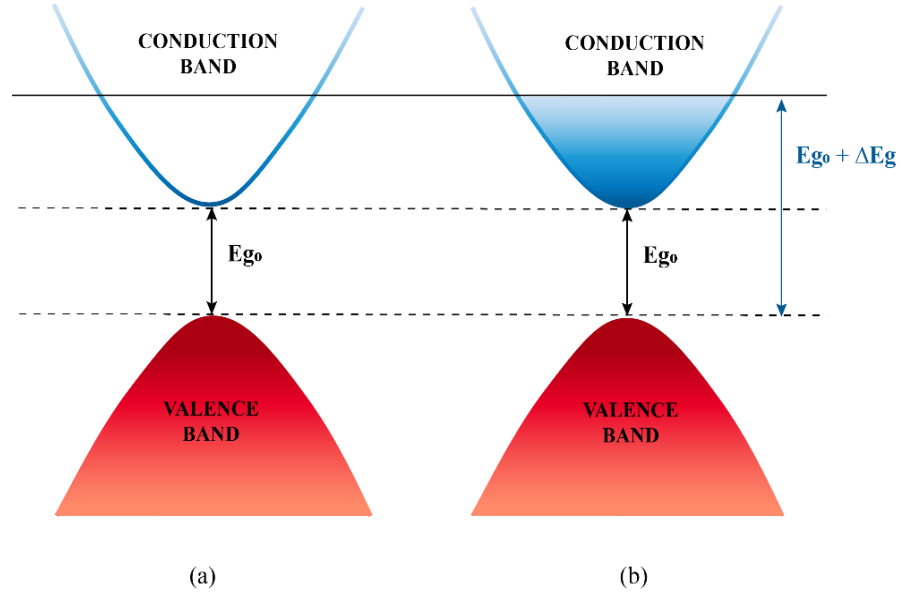


Figure 2.4: Increase of the energy band gap from E_{g0} (a) for non-doped semiconductor to $E_{g0} + \Delta E_{gMB}$ (b) for doped semiconductor due to Moss-Burstein effect.

When carriers are introduced into semiconductors, optical absorption and reflection mechanisms occur. Using Maxwell's equation, the refractive index of a substance can be rewritten for non-magnetic materials as follows:

$$\bar{n} = n_r - ik_e = \sqrt{\varepsilon_r} \quad (2.16)$$

as a function of ε_r which represents the relative permittivity.

The relative permittivity is a complex quantity:

$$\varepsilon_r = \varepsilon_1 + i\varepsilon_2 \quad (2.17)$$

with ε_1 that represents the real part:

$$\varepsilon_1 = \varepsilon_\infty - \frac{\sigma_0 \tau}{\varepsilon_0} \left\{ \frac{1}{1 + \omega^2 \tau^2} \right\} \quad (2.18)$$

where ε_∞ , ε_0 and $\sigma_0 = \frac{ne^2\tau}{m^*}$ are the high-frequency permittivity, the vacuum

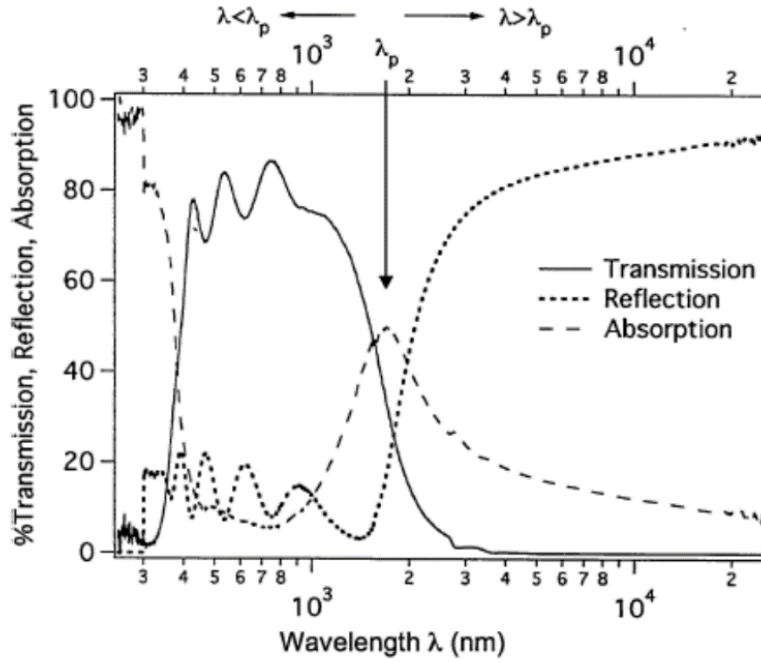


Figure 2.5: Transmission, reflection and absorption spectra of a typical TCO ⁴⁰.

permittivity, and the d.c. conductivity respectively. The quantity ϵ_2 is the imaginary part of permittivity:

$$\epsilon_2 = \frac{\sigma_0 \tau}{\epsilon_0 \omega} \left\{ \frac{1}{1 + \omega^2 \tau^2} \right\} \quad (2.19)$$

Some elementary aspects of semiconductors, hence of TCOs, can be explained with the Drude free-electron theory ⁴⁹. In the Drude theory, electrons oscillate in response to the electric field component of the electromagnetic field. When semiconductor materials are irradiated by electromagnetic radiation, the carriers start to oscillate as a plasma. The maximum threshold frequency that enables the plasma oscillation is called *plasma frequency* and can be expressed by:

$$\omega_p = \sqrt{\frac{ne^2}{\epsilon_\infty \epsilon_0 m^*}} \quad (2.20)$$

The plasma frequency represents the frequency at which the real part of the permittivity equals zero ($\epsilon_1 = 0$ and $N = k$). This results in the reflection of the light at the surface. This value corresponds approximately to the peak of the absorbance spectra, as shown in Figure 2.5. Significant changes in the optical properties occur when the frequency approaches the plasma frequency. For frequency lower than the plasma frequency (in the NIR) ϵ_1 decreases, while ϵ_2 , N and k all increase leading to an increase in the reflectance and lowering of the transmittance. For frequencies higher than the plasma frequency instead, the opposite occurs, the electrons are unable to absorb radiation, and the material behaves as a transparent dielectric. This is the region with high transmittance and low reflectance.

In metals, where carrier concentration is very high, the plasma frequency is located in the UV region, and the light is reflected at the surface, the decrease of carrier concentration, as for semiconductor material, shifts the plasma frequency towards the NIR region, which results in a wider transparency window in the visible region.

2.4. Figures of merit of Transparent Conductors

An optimal TC should have low electrical resistivity combined with high transmittance of visible light. Thus, an appropriate method to quantify the performance of TCs is to determine the Figure of Merit (FoM) defined by Haacke⁵⁰. This quantity involves two different measurements, the so-called *Sheet Resistance* R_{sh} , and the optical transmittance T at the wavelength of 550 nm. The *Sheet Resistance* is used to characterize and easily compare thin films of the same thickness as it is defined as a ratio between the bulk resistivity of the material ρ and its thickness t :

$$R_{sh} = \frac{\rho}{t} \quad (2.21)$$

The FoM is hence defined as the ratio between these two quantities:

$$FoM = \frac{T^{10}}{R_{sh}} \quad (2.22)$$

Larger values of FoM indicate better performances of TCs.

2.5. In-based TCO

The TCOs investigated in this work, are Indium-based transparent conductive oxide. The crystalline structure of In-based TCO is that of the In_2O_3 bixbyite structure shown in Figure 2.6a. The unit cell contains 16 formula units of In_2O_3 . Indium atoms occupy two different Wyckoff positions, labeled $24d$ and $8b$, while oxygen atoms occupy the Wyckoff positions of $48e$ (Figure 2.6b). In the $8b$ sites, indium has six equidistant oxygen atoms neighbors at 2.18 Å. In $24d$ sites, instead, the indium atoms are situated at the corner of a more distorted octahedron^{51,52}. For these indium atoms, there are three possible cation-oxygen distances: 2.14, 2.19 and 2.23 Å. Indium atoms reside at the center of a distorted cube with six corners occupied by oxygen atoms for both $24d$ and $8b$ sites. In the case of the $24d$ sites, they are located along the face diagonal while for $8b$ sites, oxygen vacancies are located along the body diagonal (Figure 2.6c)

In_2O_3 doped TCOs are n-type highly doped semiconductors. The most widely used Indium-based TCO is Sn-doped In_2O_3 (ITO) although other transparent conductors have attracted significant attention including amorphous ZnO-doped In_2O_3 (IZO). ITO offers the highest transmittance combined with the lowest electrical resistivity. ITO films can be deposited by various techniques such as Chemical Vapor Deposition (CVD) or Physical Vapor Deposition (PVD)

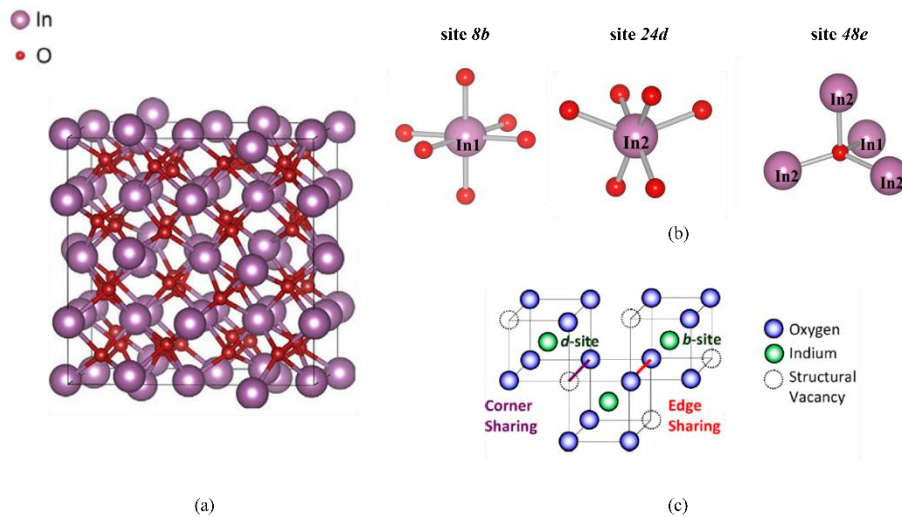


Figure 2.6: Bixbyite crystal structure of indium oxide (a). Oxygen atoms occupy two different Wyckoff position labeled, $8b$ where indium atoms are equidistant from oxygen atoms and $24d$ where indium atoms have three different distance from oxygen; oxygen atoms occupy the $48e$ Wyckoff position (b). Face-diagonal and body-diagonal placements of the oxygen vacancies for $24d$ site and $8b$ site (c).

methods. Among these different deposition processes, sputtering (rf or dc) is the preferred one.

It is well known that sputtering shows some advantages like good control of sputtering conditions and uniform deposition to a large area. Usually, ceramics targets for sputtering contain 10 wt% SnO₂ that allows obtaining thin films with resistivity down to $1.4 \times 10^{-4} \Omega\text{cm}$. Last decades, however, low-density targets (3 wt% SnO₂) have been developed to improve optical properties.

ITO opto-electrical properties are strongly influenced by process conditions such as sputtering power, gas working pressure, oxygen flow, temperature of the substrate during the deposition, and post-deposition annealing treatments. Typically, sputtering processes are performed at elevated substrate temperatures, above 250-350 °C, as these guarantee the highest optical transmittance and the lowest resistivity. Resistivity in ITO is related to carrier concentrations, which in these films originate mainly from doping donors Sn and oxygen vacancies, which in these films originate mainly from doping donors Sn and oxygen vacancies. When an Sn atom substitutes In in a substitutional site, contributes with one electron in the conduction band, while every oxygen vacancy, which is a double-charged donor, contributes with two electrons. High

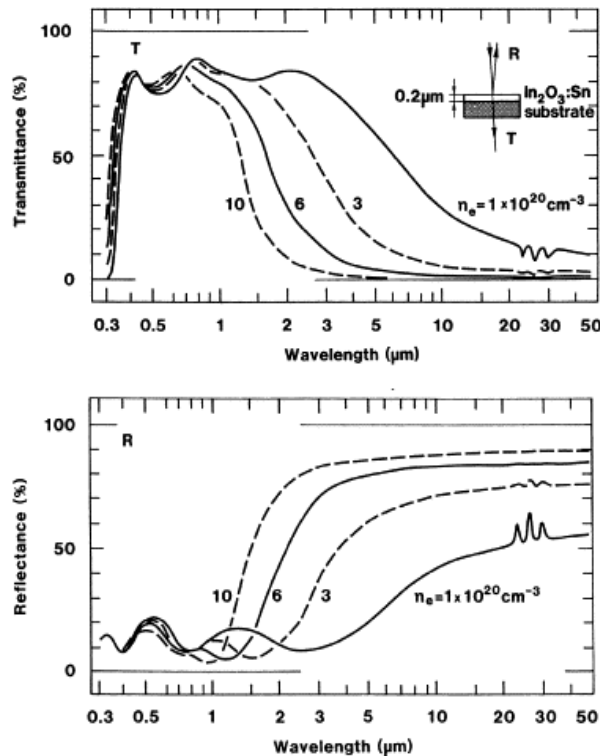


Figure 2.7: Spectral normal reflectance R and transmittance T computed from a quantitative theoretical model for the optical properties of ITO⁴⁰.

values of carrier concentrations decrease carrier mobility due to ionized-impurity scattering. The carrier concentration is also influenced by the oxygen flow introduced during the sputtering process, along with the Sn donors concentration. Appropriate oxygen flow calibration should be performed to find a value where the resistivity shows the minimum value. High oxygen flow during deposition fills the native oxygen vacancies decreasing the carrier density and increasing the resistivity. A low oxygen flow is hence preferred as it leads to higher carrier densities with a consequent decrease of the resistivity.

An appropriate value of carrier concentrations is important not only for the electrical properties but also for the optical ones. Figure 2.7 shows the modeled transmittance and reflectance spectra for ITO, with different carrier concentration values^{53,54}. In the figure we see how different values of n strongly influence the transparency window increasing the bandgap, as a consequence of the *Moss-Burstein* effect, and decreasing the *plasma wavelength*. The optical properties of ITO can be improved with post-deposition thermal treatments. The transmittance of post-annealed films reaches 80% in the region of visible. These variations may be attributed to the annealing of defects originally present in as-deposited films. For as-deposited films in the region close to the optical band-gap, the heavily doped semiconductor can present absorption edges with a logarithmic shape, called *Urbach tails*⁵⁵. This is a defect-related phenomenon due to the formation of intra-gap states represented by non-activated-dopant that contribute to creating these tails. Annealing at appropriate temperatures, help to activate these donors and eliminate the trapping states.

2.5.1. Transition metals-doped In_2O_3

The design of novel n-type transparent conducting oxides beyond Sn-doped In_2O_3 to improve conventional TCO has stimulated extensive interest in the past decade. Improving conventional TCO that can be implemented in the present industrial processes has been the driving force for the research activity in the transparent conductor field. Beyond the demand for long-term stability and sustainable TCO, the demand has extended to TCO with transparency and conductivity which guarantee higher performances. The approaches to using transition metals (TMs) as dopants have attracted high interest in the last years. As shown by equation 2.6, the conductivity in a semiconductor is strongly related to the carrier mobility, which depends on the relaxation time, the charge carriers, and the electron effective mass (equation. 2.7). Therefore, the carrier mobility can be increased by increasing τ or by decreasing m_e . Increasing τ requires the decrease of impurity scattering, lattice distortion scattering, acoustic phonon scattering, and longitudinal optical phonon scattering^{12,47,56}. Decreasing m_e requires the increase of CBM band edge dispersion. In ITO the strong

hybridization between the Sn and In 5s states at the bottom of the conduction band of In_2O_3 can renormalize its band curvature (Figure 2.8a), upon doping because of the increased m_e . Hence, the resulting carrier mobility decreases⁵⁷.

It is expected that transition-metal (TM) atoms might be promising dopants because the TM d orbitals may have sufficiently higher orbital energies than that of In 5s orbitals. Moreover, differing from Sn, the orbital hybridization between TM d orbitals and In 5s orbitals is weak. This results in lower band curvature around the CB minimum (CBM) of In_2O_3 and an electron-effective mass that could be largely maintained (Figure 2.8b). Transition Metal dopants can be classified into three different categories: type-I, type-II, and type-III⁴³:

- **type-I donors** are Titanium (Ti), Vanadium (Va), Chromium (Cr), and Molybdenum (Mo). For these elements, the *d-orbital* defect levels are significantly lower in energy than the conduction band minimum of In_2O_3 (Figure 2.9a), and consequently, effective n-type doping cannot be achieved at room temperature.
- **type-II donors** like Niobium (Nb) and Tungsten (W) form the *d-orbital* defect levels above the conduction band minimum of In_2O_3 . However, these levels are not high enough in energy (Figure 2.9b). The *d bands* will merge with the occupied conduction band when the system is heavily doped so that the Fermi level will be pinned by the partially occupied *d levels*. Although n-type doping can be achieved, the n_e and μ_e will be low due to the large effective mass of the transition metal *d bands*.
- **type-III donors** are Zirconium (Zr), Hafnium (Hf), and Tantalum (Ta): for these atoms, the *d-orbital* defect levels are sufficiently high in energy above the conduction band minimum of In_2O_3 , so that transition metal donors can be fully ionized (Figure 2.9c) and m_e can be largely maintained; therefore, ideal n-type doping could be realized with high μ_e and n_e .

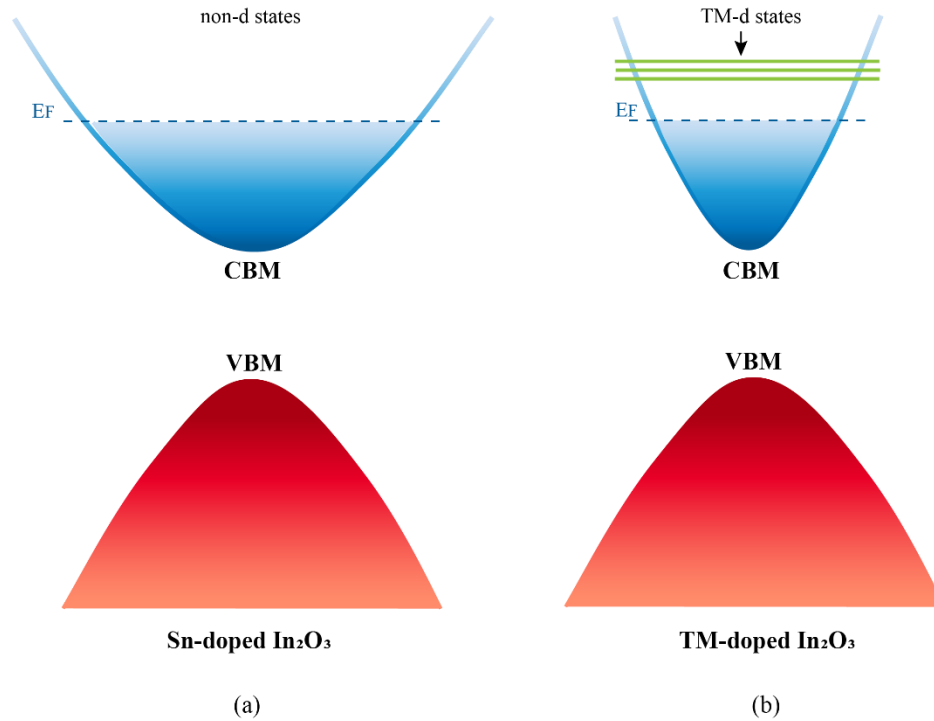


Figure 2.8: In_2O_3 conduction band upon Sn doping (a) and TM doping (b).

In_2O_3 doped with transition metal elements has been proven to be an excellent material for developing high-performance TCOs with variable dopant introduction, such as Zr^{58,59}, Ti⁶⁰, Mo⁶¹, Hf⁶², and W⁶³⁻⁶⁵. Along with the goal of higher performance, however other issues related to material's sustainability, durability, and production cost must be taken into account for further investigation. The cost of producing TCO depends on the cost of raw materials and processing them into thin films. While searching for new TCO approaches and materials it is necessary to determine the right trade-off between optimal performance and sustainability. If from one side ITO contains expensive and toxic elements such as indium and tin and will be better replaced with more sustainable TCO with abundant elements, like AZO, the consolidated excellent opto-electrical properties of indium-based TCO cannot still be replaced in the present industrial process.

The aim is to reduce Indium consumption, through different basic strategies that can be classified into three types. The first concerns the development of In-free TE, as In-free TCO (AZO or AZO/Ag/AZO multilayer structure)^{17,18,66,67}, conductive Polymers as PEDOT PSS³⁴, or nanostructured metals as metallic NWS and metal grids^{29,68}, or carbon nanotubes⁶⁹. The second possibility moves towards the recycling of Indium from old Perovskite solar cells

or sputtering deposition waste (from ITO deposited on the equipment or unused target). The last solution concern the reduction of TCO thickness from the 100 nm thickness standardly used in solar cells down to 15-20 nm. Thinner TCO could reduce free carrier absorption but this could be eventually avoided by adding ARC materials such as SiOx, or SiN to reach an optimal light in coupling^{64,70,71}.

The challenge when we decrease the thickness is that the sheet resistance increases. So the key is to look for dopants for indium oxide that can improve the resistivity of the material through an enhancement of the carrier mobility. This challenge can be well accomplished by transition metals as explained in the last paragraph.

In this work, to develop TCO with a lower amount of indium without leading the opto-electrical properties we choose an element from the group of first type donors, Mo, and an element from the third group donors, Zr, as dopants. Mo has been introduced into the ITO host material to explore the possibility of a co-doping of In_2O_3 with Sn and Mo to improve mobility, whereas, in the other approach, In_2O_3 has been doped with Zr to develop ultra-thin TCO films with reduced thickness down to 20 nm. Deposition and characterization methods of these TCO films will be discussed in Chapter 3, and the structural, electrical, and optical properties will be shown in Chapters 4 and 5.

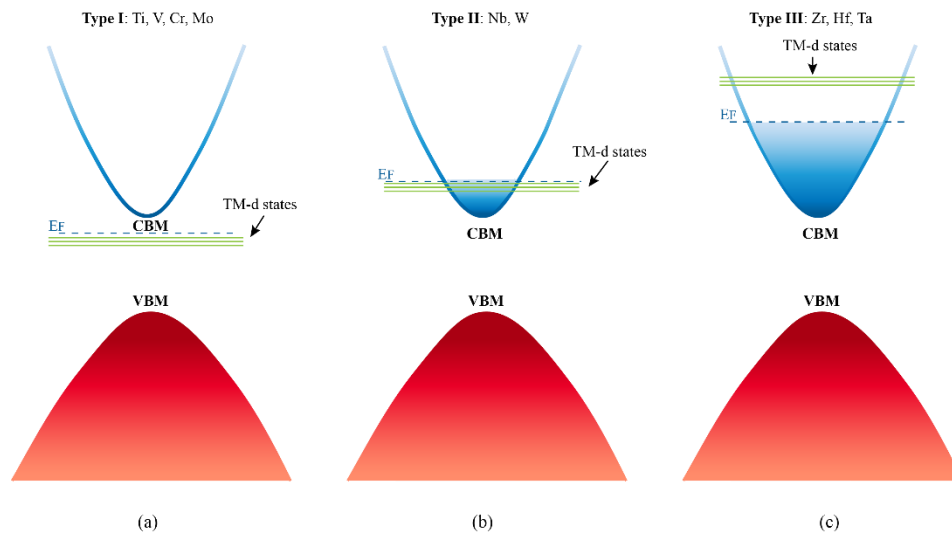


Figure 2.9: Schematic diagrams of band structures for type-I (a), type-II (b), and type-III (c) TM-doped In_2O_3 . The Fermi Energy (E_F) is represented by a dashed line.

3. Experimental Methods

3.1. Introduction

In this chapter, the experimental methods used for the growth and characterization of TCO thin films will be briefly discussed. Two types of In-based TCO will be proposed in this work: Mo-doped ITO, as an example of In_2O_3 co-doping, and Zr-doped In_2O_3 ultra-thin films. In both cases, transition metals (Mo, Zr) have been used to dope In_2O_3 to develop TCO with improved properties. Samples have been deposited through sputtering deposition, with radio frequency (for ITO and In_2O_3) and direct current (for Mo and Zr) sources. Structural, electrical, and optical properties have been studied before and after the annealing treatments performed at different temperatures.

3.2. TCO deposition

Deposition methods traditionally used for TCO should guarantee sufficient low resistivities and large area mass production. Among the different types of deposition methods for thin films, evaporation and sputtering are the most used ones. Magnetron sputtering is usually preferred because of its high deposition rate, optimal quality of the TCO, and high potential for large area depositions.

Sputtering is a physical vapor deposition (PVD) process in which a solid surface (target) is bombarded with energetic ions, with a consequent ejection of atoms or molecules, as illustrated in Figure 3.1⁷². The vapor phase of the coating

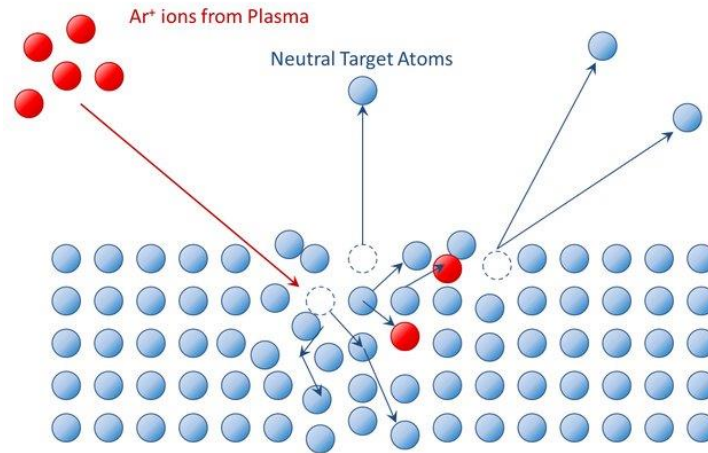


Figure 3.1: schematic representation of the sputtering mechanism. Energetic ions, usually Ar^+ , hit the atoms of the coating materials, ejecting them from the target.

material is obtained by a physical momentum-exchange process and any chemical and thermal process is avoided. The versatility of this technique guarantees the coating of different types of materials, even alloys, employing different targets simultaneously, or sequentially, to create a layered coating.

The sputtering process can be divided into three fundamental steps:

1. production of energetic projectile ions;
2. vapor phase formation of ejected atoms from the coating material and transport towards the substrate;
3. adhesion and deposition of the atoms on the substrate;

Sputter deposition is a vacuum coating process where the chamber is pumped to a pressure ranging from 10^{-5} mbar to 10^{-9} mbar. To provide the ion bombardment necessary for the sputtering process, the evacuated chamber is backfilled with a continuous flow of inert gas, such as Argon, to avoid chemical reactions at the target and substrate. Then, a glow discharge is established. To initiate positive-ions bombardment of the target a negative potential is applied to the target while the substrate is grounded ⁷³.

The sputtering yield, Y , is defined as the number of target atoms ejected per incident projectile (equation 3.1). It quantifies the sputtering process and depends on the target species and the nature, energy, and angle of incidence of the bombarding species. The dependence of the sputtering yield on incident ion

energy, evidence of a *threshold energy* for sputtering, below which, no sputtering occurs. The surface binding energy of the atoms (2 -10 eV) must be exceeded for the atom to escape from the solid by sputtering. The sputtering yield also depends on the mass of the bombarding particles. If the mass of the bombarding particle is of the same order of magnitude as the mass of the target atoms, the sputtering yield tends to be higher. According to this, Argon meets also the requirement of mass compatibility with the materials and low cost.

$$Y = \frac{\text{number of ejected atoms}}{\text{number of incident atoms}} \quad (3.1)$$

The sputtering process is a result of momentum exchange between ions and atoms. During the impact, the momentum imparted to the target particle drives it onto the lattice and then a fraction of the kinetic energy is transferred to the target particle. The sputtered material is ejected in the neutral atomic state.

The adhesion and deposition of the sputtered atoms on the substrate are controlled by the argon gas pressure which influences the mean free path of the sputtered atoms. Sputtered atoms should have a mean free path comparable to, or higher, the distance between the target and the substrate to avoid any other possible collision. Pressure and mean free path are related by the following relation (equation 3.2):

$$\lambda = \frac{RT}{\sqrt{2}\pi d_{Ar}d_{at}N_A p} \quad (3.2)$$

where R is the universal gas constant, T is the gas temperature, d_{Ar} and d_{at} are the dimensions of the argon ions and sputtered atoms respectively, N_A is the Avogadro Number, and p is the gas pressure. The higher the pressure, the higher the ionic current and the final number of sputtered atoms are. However, the pressure value should not exceed the trade-off between the number of sputtered atoms and the mean free-path⁷⁴.

3.2.1. RF and DC Magnetron Sputtering

Sputter deposition technology has grown in a variety of ways. The condition under which sputtering is done (reactive or bias) or the configuration used for sputtering (ion beam sputtering, RF sputtering, DC sputtering, magnetron sputtering, etc..) is indicated by an appropriate prefix. In this work both DC and RF Magnetron sputtering have been used and will be briefly described.

Typical rates of sputtering can be around $100\text{\AA}/\text{min}$ for metals and a few tens $\text{\AA}/\text{min}$ for insulating materials. The origin of this slow rate of sputtering is due to the very low efficiency in the use of electrons to create ions. Increased ionization of the sputtering gas at a given pressure is possible by the use of additional electrons with the assistance of a magnetic field. The application of an axial magnetic field can increase the path length of the electrons that execute longer helical path orbits before reaching the anode. The presence of the magnetic field, in addition, helps the electrons to stay away from the walls of the sputtering chamber, hence, reducing the losses of electrons due to the recombination process at the walls. Magnetron configurations (Figure 3.2) eliminate the path of electrons going to the walls or the substrate. The electrons remain trapped near the target, in a combined electric and magnetic field, so they can increase their ionizing effect and high deposition rates can be achieved. The kinetic energy of the sputtered atoms increases as the probability of atoms from the cathode to the substrate.

Direct Current (DC) sputtering employs a DC glow discharge. A DC power supply energizes the electrodes to create a discharge, where the target is the negative electrode. The electrode at positive potential is the anode and the electrode at the lower or negative potential is the cathode. The electrons are emitted and accelerated away from the target surface at energies equal to the cathode fall potential. These primary electrons enter the so-called *glow region* and collide with the gas atoms causing the ionization of the gas. The positive ions created in the plasma accelerate when they arrive in the vicinity of the cathode plasma sheath. The atoms ejected from the target condense on the substrate to

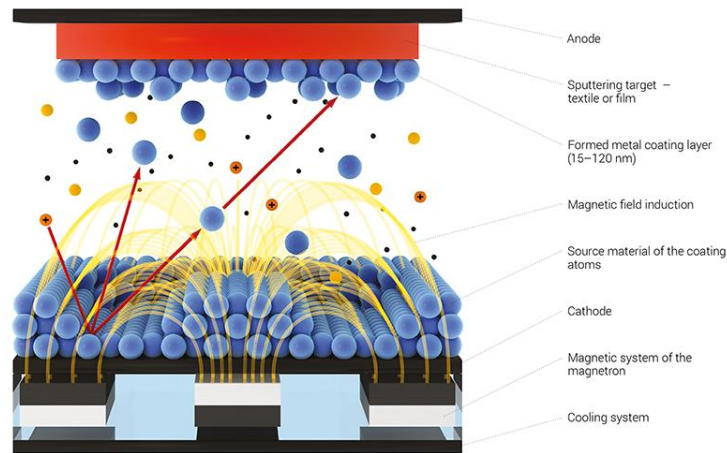


Figure 3.2: Magnetron Sputtering system. The addition of a magnetic field increases the length path of electrons, leading to an increase of the ionization of the sputtering.

form a thin film. DC sputtering impose the limitation that electrodes have to be conductors. If non-conducting electrodes are used, the electrons accumulate on the surface of the insulating electrode. The ions and the electrons recombine on the surface, and without any need to conduct current through the electrodes, the discharge will extinguish itself.

Insulating electrodes can be regarded as capacitors, hence an alternating electric field of sufficient frequency can produce a discharge almost continuously. Initially, both capacitors are uncharged and there is no voltage across them. Then the voltage is applied, drops to a negative value, and the discharge is initiated, hence, this voltage exceeds the breakdown voltage. If the electrodes change polarity every half cycle, each electrode acts as a cathode alternately. If the substrate is insulating, the ions are neutralized at the surface by some electrons already accumulated there. Before the complete ionization occurs, the voltage reverses and if the frequency of the impressed electric field exceeds a certain critical ion frequency, the discharge can be maintained. Radio Frequency (RF) sputtering employs an RF power source at 13.56 MHz. Unlike in a DC discharge, electrons do not reach the anodes since both electrodes in RF discharge are at a negative potential compared to the plasma, and electrons are essentially reflected back and forth between the electrodes and they utilize the energy they gain in the electric field to cause ionization⁷³.

The experimental equipment used in this work is a nanoPVD-S10A-WA by Moorfield Nanotechnology equipped with two magnetron sputtering sources, an RF and a DC power supplies. In this configuration, two targets can be sputtered, either at once or in sequence in the vacuum chamber, and the power to each cathode can be controlled independently.

3.3. TCO characterization

3.3.1. Rutherford Backscattering Spectrometry

Rutherford Backscattering Spectrometry is a non-destructive and multi-elemental ion beam material characterization method based on a sample bombardment with light energetic ions, typically He⁺ in between 1 to 3 MeV energy, with the subsequent measurement of the backscattered He⁺ ions intensity and energy. The technique allows a quantitative measurement of the masses of the elements in a sample, their depth distributions, and their areal density⁷⁵.

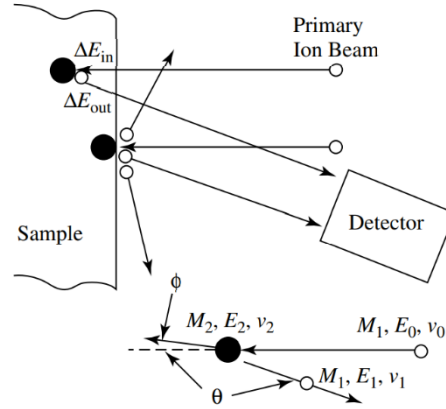


Figure 3.3: schematic of the RBS measurement and experimental set-up. Energetic He^+ ions with mass, energy and velocity M_1, E_0 and v_0 bombard the sample's atoms with mass, energy and velocity M_2, E_2 and v_2 . During elastic collision between the energetic ions and the nuclei of the sample's atoms, the ions are reflected backward and collected by a detector.

The method is schematically illustrated in Figure 3.3. Ions of mass M_1 , atomic number Z_1 , energy E_0 , and velocity v_0 hit a sample composed of atoms of mass M_2 atomic number Z_2 . The incident ions that interact with valence electrons undergo anelastic collisions losing energy within the sample. A small fraction of the incident ions, however, is backscattered from the sample during elastic collisions with the nuclei of the sample atoms.

The primary ion energy loss is quantified by the *Kinematic Factor K*:

$$K = \frac{E_1}{E_0} = \left[\frac{(M_2^2 - M_1^2 \sin^2 \theta)^{1/2} + M_1 \cos \theta}{M_1 + M_2} \right]^2 \quad (3.3)$$

with M_1 and M_2 the mass of the incident ions and the sample atoms respectively, and θ the backscattering angle.

The incident ion interacts not only with the surface atoms but also with those below. The ions lose energy within the sample and they will be backscattered with energy $E_1 < E_0$.

The RBS spectrum returns the counts of the backscattered ions as a function of the energy. Every element will generate a signal characterized by:

- a *threshold energy* that is given by the element mass;

- a *height* linked to the element atomic concentration and the cross-section of the process;
- a *width* dependent on the energy loss within the sample at different depth

The integral of the signal is linked to the material thickness through the following relation:

$$N_A t = \frac{A_A}{Q \Omega \sigma_A(E_0)} \quad (3.4)$$

with Q number of the incident ions, Ω the solid angle subtended by the detector, $\sigma_A(E_0)$ the backscattering cross section for the specimen atom A , N_A the atomic density of the specimen A , and t the material thickness⁷⁶.

The experimental set-up is illustrated in Figure 3.4 and is formed by:

- particle accelerator where the incident ion beam is created;
- a magnet to deviate the beam;
- a scattering chamber for the collision and backscattering process, equipped with a sample holder that can be rotated through a goniometric system;
- a Si-detector formed by a p-n junction;

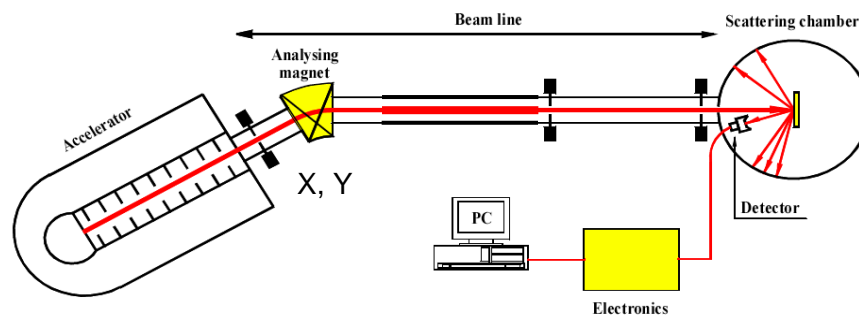


Figure 3.4: Experimental set-up for the collection of RBS spectra.

3.3.2. X-Ray Photoelectron Spectroscopy

X-Ray Photoelectron Spectroscopy is a spectroscopic technique based on the photoelectric effect and it is primarily used to identify chemical species and

their chemical status at the sample surface. For the photoelectric effect (Figure 3.5), X-ray photons interact with core-level electrons, and electrons can be emitted from any orbital with binding energies lower the X-ray one. The fundamental equation for the photoelectric effect is given by:

$$KE = h\nu - (E_B + \Phi) \quad (3.5)$$

where KE and E_B are the kinetic energy and the binding energy of the emitted electron respectively, $h\nu$ is the X-rays photon energy, and Φ is the work function of the sample⁷⁷.

X-rays with 1 to 2 keV energy can eject electrons from several orbitals of the sample. The ejected photoelectrons enter into the spectrometer so that their intensity and energies are analyzed. In a typical XPS spectrum the intensities of photoelectrons are reported as a function of the binding energy.

In Figure 3.6 is shown the energy diagram of the sample and the spectrometer during the measurements. The energy fermi levels are at the same level but the vacuum levels are different. As an electron enters into the spectrometer, its kinetic energy is diminished by the difference between the work function of the spectrometer and the work function of the sample ($\Phi_{spec} - \Phi$). Hence, the measured energy of the ejected electron can be related only to the energy of the primary X-rays and the work function of the spectrometer⁷⁷⁻⁷⁹:

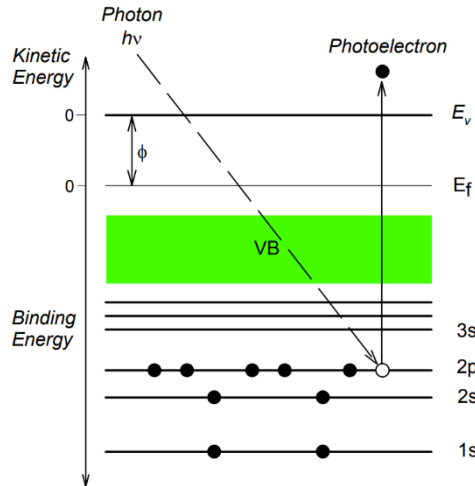


Figure 3.5: schematic representation of photoelectrons emission. X-ray photons determines the emission of electrons from the core level of the atoms.

$$KE = h\nu - E_B - \Phi_{sp} \quad (3.6)$$

The electron binding energy is influenced by its chemical surroundings making this technique useful for chemical and elemental identification.

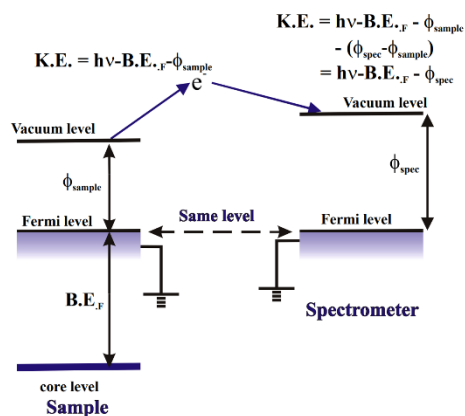


Figure 3.6: binding energy reference diagram for XPS experimental set-up.

3.3.3. X-Ray Diffraction

X-ray diffraction is a non-destructive technique used to determine the structure and the crystallinity of a solid sample. The scattering of X-rays from atoms produces a diffraction pattern, which contains information about the atomic arrangement within the crystal.

Typically diffraction occurs when light is scattered by a periodic grating with long-range order, producing constructive interference at specific angles. The atoms in a crystal are arranged in a periodic array with long-range order and thus can produce diffraction if the probe has a wavelength comparable with the interatomic distance. Each atom can act as a coherent point of scattering because

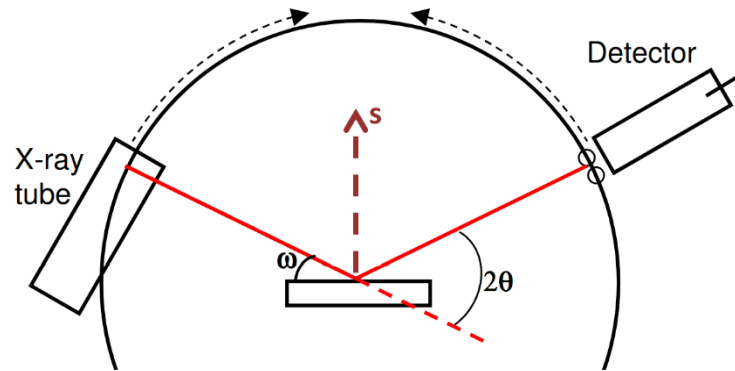


Figure 3.7: XRD experimental set-up.

of the electrons around the atom. The wavelengths of X-rays are similar to the distance between atoms in a crystal and they are used to study the electronic structure⁴⁶.

An X-rays diffraction pattern is characterized by some characteristic diffraction peaks, whose positions and intensities are the product of the unique crystal structure of a material. Diffraction peak widths and shapes instead are mostly a function of the instrument and microstructural parameters. Each diffraction peak is attributed to the scattering from a specific set of parallel planes of atoms identified by the *Miller indices* (hkl)⁸⁰.

As illustrated in Figure 3.7, a diffractometer contains:

- an X-rays tube as source of photons;
- an incident-beam optics to control the X-ray beam before the interaction with the sample;
- a goniometer, a platform that holds and moves the sample, optics, detector, and/or tube;
- a receiving-side optics to condition the X-ray beam after it has interacted with the sample;
- a detector to measure the intensity of the X-rays scattered by the sample at different angles;

Considering a perfect crystal with lattice planes spaced d , X-rays of wavelength λ are incident on the sample at an angle α , defined between the X-rays source and the sample, as shown in Figure 3.8. Constructive interference only occurs when Bragg's law is satisfied, hence the diffracted beam emerges at twice the Bragg angle θ_B

$$\theta_B = \arcsin\left(\frac{\lambda}{2d_{hkl}}\right) \quad (3.7)$$

The diffraction angle, $2\theta_B$, is defined between the incident beam and the detector. The detector moves in a circle around the sample and it records the intensity of X-rays at each angle 2θ .

Crystallites create broadening of the diffraction peaks. After an appropriate calibration, to determine the contribution of peak width from the instrument, this peak broadening can be used to quantify the average crystallite size, D , using the Scherrer equation :

$$D = \frac{K\lambda}{W\cos\theta} \quad (3.8)$$

where K represents the Scherrer constant, λ is the X-rays wavelength, W represents the FWHM of the peak and $\theta = 2\theta/2$ is the peak position.

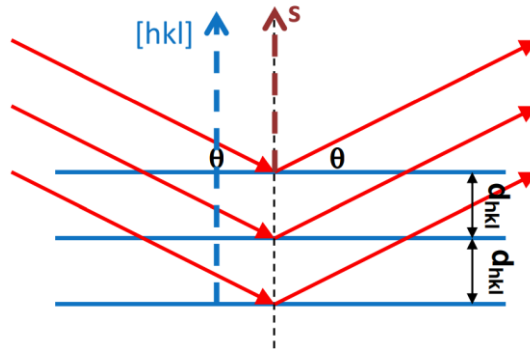


Figure 3.8: Bragg's law diagram.

3.3.4. Atomic Force Microscopy

Atomic Force Microscopy (AFM) is a specific type of scanning probe microscopy used to study the surface properties of materials from the micrometer down to the atomic level. A scanner and a probe are the two fundamental components of this technique. The scanner moves the probe over the surface in a

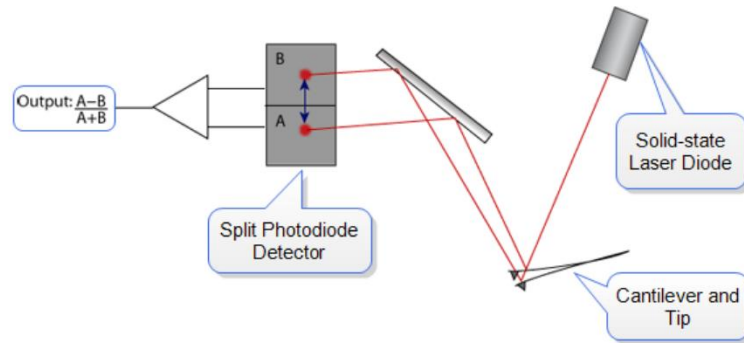


Figure 3.9: Experimental set-up for AFM microscopy.

precise, defined pattern known as *raster pattern*. The probe used in an AFM is a sharp tip, located at the edge of a cantilever. When the tip and the sample are close together, forces between the tip and the sample surface cause the cantilever to bend, or deflect. A photodiode detector measures the cantilever deflections as the tip is scanned over the sample. The measured cantilever deflections allow a computer to generate a map of the surface topography^{81,82}. The experimental set-up is illustrated in Figure 3.9. Several forces typically contribute to the deflection of an AFM cantilever. To detect the position of the cantilever, a solid-state laser diode is used. A light beam from a laser diode bounces off the back of the cantilever and onto a position-sensitive photo-detector. As the cantilever bends, the position of the laser beam on the detector changes.

These forces, as illustrated in Figure 3.10, change as the separation distance between the tip and the sample changes.

As the tip and the sample are gradually brought together, their atoms begin to weakly attract to each other. This attraction increases until the atoms are so close together that their electron clouds begin to repulse each other. As the separation continues to decrease, this electrostatic repulsion progressively weakens the attractive force. Finally, the total force goes through zero and becomes repulsive, in the positive region.

There are three AFM primary modes defined in terms of the type of force being measured and how it is measured⁸³:

- Contact Mode, where the tip is in always in contact with the sample. The contact force causes the cantilever to bend according to changes of the topography. By maintaining a constant cantilever deflection, the force between the sample and the tip remains constant.

- Non-Contact Mode in which an AFM cantilever vibrates around its resonance frequency close to the surface of the sample. The interatomic forces between the cantilever and the sample in this regime is attractive. The system detects changes in the cantilever's resonance frequency or vibration amplitude. The system monitors the resonance frequency or the vibration amplitude of the cantilever by keeping them constant, moving the scanner up and down.
- Tapping Mode maps the topography by lightly tapping the surface with an oscillating probe tip. The cantilever's oscillation amplitude changes with sample surface topography and by monitoring these changes and minimizing them, the topography image is obtained.

The AFM technique in this work has been used in the Peak Force Tapping Mode, patented by Bruker.

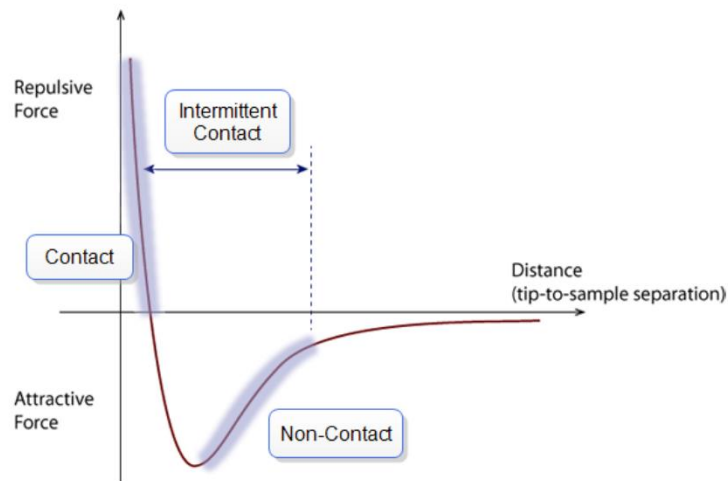


Figure 3.10: The effect of tip-to-sample distance on the force interaction between tip and sample.

3.3.5. Kelvin Probe Force Microscopy

Kelvin Probe Force Microscopy is a technique used for surface potential detection. Since KPFM is an AFM-based apparatus, it is possible to local measure the contact potential difference between a conductive AFM tip and the sample, mapping the work function or surface potential of the sample with high spatial resolution⁸⁴. The experiment can be modelled as a parallel plate capacitor. Figure 3.11 shows the energy level of the tip and the sample surface for the different steps of the measurements. Figure 3.11a illustrates the energy levels of the tip and the sample when they are separated by a distance d and not electrically connected. The vacuum levels are aligned but the Fermi energy levels are different. When two materials with different work functions are brought together with an electrical contact, electrons in the materials with the lower work function flow to the material with the higher work function (Figure 3.11b). The system can be considered a parallel plate capacitor with equal and opposite surface charges on each side and an apparent *contact potential difference* V_{CPD} , will form. Now, the vacuum levels are not aligned anymore but the Fermi-energy levels are the same. An external potential V_{DC} is applied to the capacitor until the surface charges disappear (Figure 3.11c). The amount of applied external bias that nullifies the electrical force due to the potential gradient has the same magnitude as the V_{CPD} but opposite direction, and it is equal to the work function difference between the tip and the sample.

$$V_{CDP} \cdot e = \Phi_{tip} - \Phi_{sample} \quad (3.9)$$

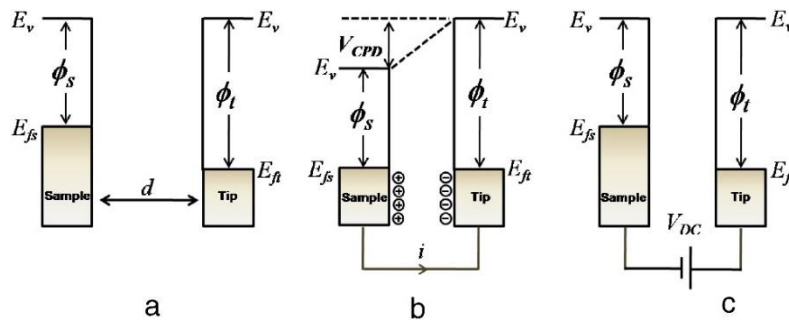


Figure 3.11: Electronic energy levels of the sample and AFM tip for the three different steps of the experiment. The tip and sample are separated by distance d with no electrical contact (a); the tip and sample are in electrical contact (b), and (c) an external bias (V_{DC}) is applied between tip and sample to nullify the tip–sample electrical force. E_v is the vacuum energy level. E_{Fs} and E_{Ft} are Fermi energy levels of the sample and tip, respectively⁸⁵.

where e is the electric charge⁸⁵. Hence the work function of the sample can be calculated if the work function of the tip is known.

There are two main methods for surface potential imaging (Figure 3.12):

- Amplitude Modulated KPFM (AM-KPFM)
- Frequency Modulated KPFM (FM-KPFM)

Amplitude Modulated KPFM (AM-KPFM) is a two-pass procedure where the surface topography is obtained by Tapping Mode AFM in the first pass and the surface potential is measured on the second pass. First, the cantilever is mechanically vibrated near its resonance frequency, then on the second pass the drive piezo is turned off, and an oscillating voltage $V_{AC} \sin(\omega t)$ is applied directly to the probe tip. If there is a DC voltage difference between the tip and the sample, then there will be an oscillating electric force on the cantilever at a frequency ω . Hence, the cantilever vibrates and an amplitude change can be detected (Figure 3.12a). Local surface potential is determined by adjusting the DC voltage on the tip until the oscillation amplitude goes to zero and the tip voltage is the same as the surface potential. The voltage applied to the tip to nullify the amplitude oscillation is recorded to construct the surface potential map.

In Frequency Modulated KPFM (FM-KPFM) mode, the information about tip-sample interactions are provided by changes in the oscillation frequency. FM-KPFM is a Tapping Mode single-pass technique. The cantilever oscillation frequency changes due to the tip-sample distance variation (Figure 3.12b). A DC voltage is applied to nullify these changes to keep the set-point frequency constant⁸⁶.

Differences between AM/FM- KPFM modes lead to a higher spatial resolution for FM modes but also a higher signal-to-noise ratio. The reasons behind these results can be explained by modelling the tip-sample interaction with the harmonic oscillator model. Based on this analytical description, the amplitude change in AM modes is dependent on the force between the tip and the sample, whereas in FM modes the frequency changes are dependent on the force gradient between the tip and the sample, enabling FM mode to have higher spatial resolution than AM modes.

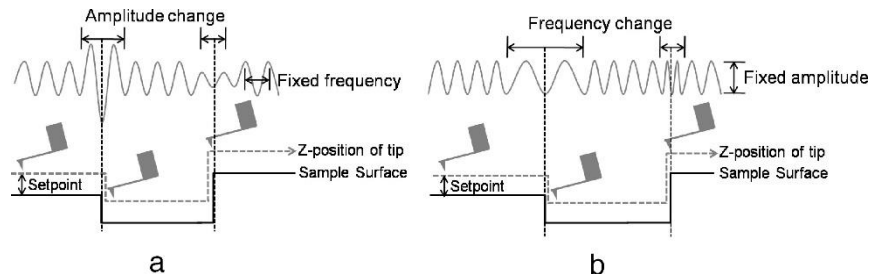


Figure 3.12: Schematic representation of KPFM modes measurements: (a) Amplitude modulation mode and (b) Frequency modulation mode. Both AM and FM modes maintain constant tip-sample separation. AM mode uses oscillation amplitude changes as a feedback signal while FM modes uses oscillation frequency change as feedback ⁸⁵.

In this work, surface potential maps are acquired in Peak Force KPFM modes which is a combination of PeakForce Tapping Mode and FM-KPFM mode. With this combination, patented by Bruker, FM modes measures surface potential using two-pass measurements, as AM modes, representing a better combination of spatial resolution and signal-to-noise ratio ⁸⁶.

3.3.6. Scanning Electron Microscopy

Electron microscopy uses electrons as probe and it was created with the aim of increasing the resolution of optical microscopes that use visible photons as a source. The spatial resolution of whichever instrument uses lenses for obtaining images of an object is limited by diffraction effects to a minimum value essentially determined by the wavelength. The maximum resolution which is possible to obtain with an optical microscope is about 200 nm. The shorter wavelength of electrons results in better theoretical resolution.

The Scanning Electron Microscope (SEM) is formed by different components as illustrated in Figure 3.13.

A stream of electrons is formed by the *Electron Source* and accelerated toward the sample using a positive electrical potential. Depending on the voltage set to accelerate the electrons, the wavelength can be derived. Typical acceleration voltages in SEM are in the range between 100 eV and 30 keV, hence the associated wavelengths are in the range between 0.12 nm and 7 pm. The higher the acceleration voltage, the shorter the wavelength achieved and the higher the spatial resolution.

The stream is confined and focused using metal apertures and magnetic lenses into a thin, focused, monochromatic beam. Hence, the beam is focused onto the sample using *magnetic lenses*. *Scanning coils* are used to raster the beam

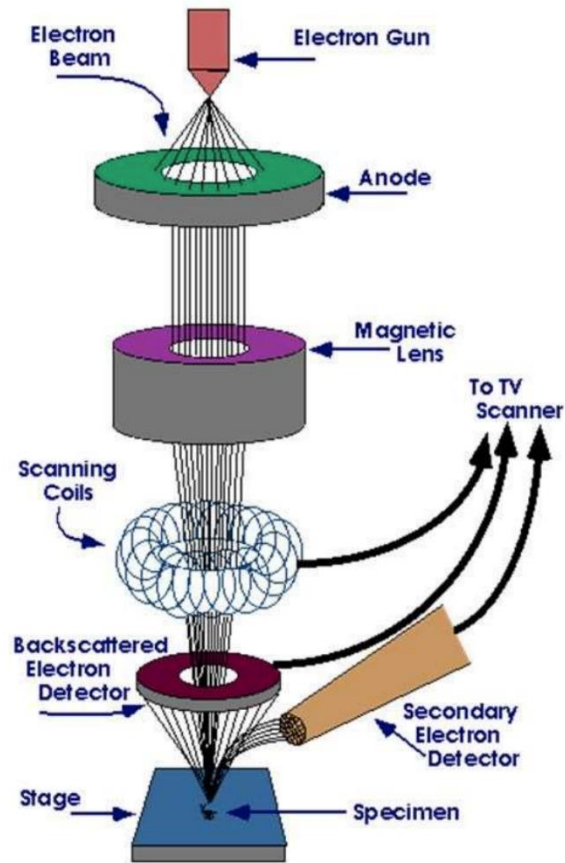


Figure 3.13: Scanning Electron Microscope components.

across the sample for texturing imaging. Interactions occur at the collision point with the specimen generating signals which are collected by detectors and converted into an image⁸⁷.

The beam-specimen interaction is characterized by an interaction volume (Figure 3.14) and depends on:

- atomic number: materials with a higher atomic number absorb more electrons (smaller interaction volume)
- the acceleration voltage: electrons with higher voltages penetrate deeper into the sample and generate larger interaction volumes

3.3 TCO characterization

- the angle of incidence of the electron beam: the greater the angle (from the normal) the smaller the volume

As illustrated in Figure 3.14, SEM can generate different signals but only two main scattering mechanisms are relevant for the image formation: elastic scattering which originates *backscattered electrons (BSE)*, and inelastic scattering with the emission of *secondary electrons (SE)*^{88,89}. Elastic scattering derives from the scattering of electrons with the nuclei and there is no energy transfer. The energy of the beam electron is unchanged and the only change is in the direction of the motion of the beam electrons. When the electrons scatter with the electrons of the atoms of the sample, inelastic scattering occurs and the kinetic energy of the beam electron diminishes.

The BSE electrons (Figure 3.15) have energies close to the energy electron beam ($50 \text{ eV} < E < E_0$). The majority of BSE electrons are therefore emitted with intensities proportional to the atomic number of the atoms of the

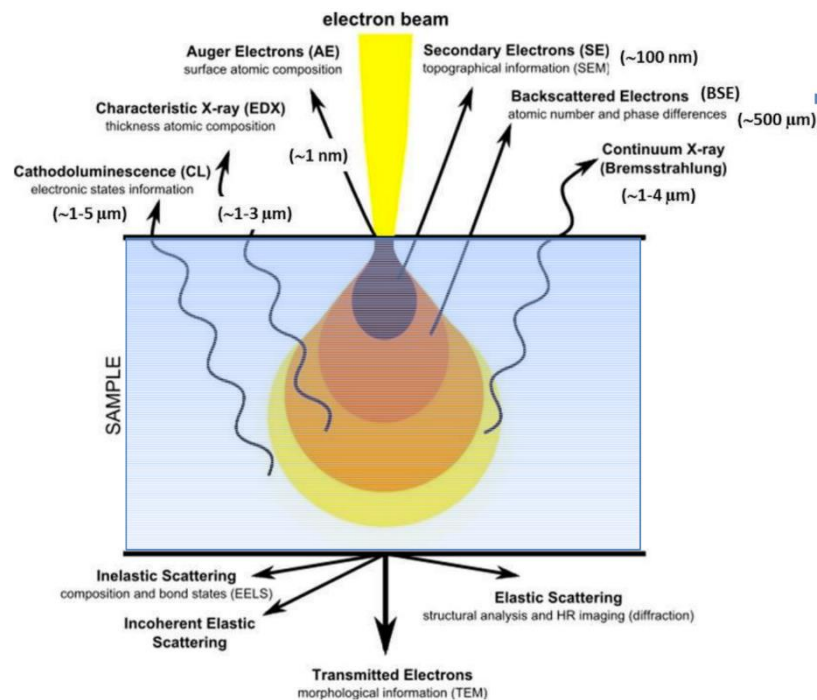


Figure 3.14: Beam-specimen interaction volume and signals produced as a function of the electron penetration-depth.

specimen. The BSE electrons are collected by solid-state semiconductor detectors and carry compositional information about the sample.

The secondary electrons are electrons emitted with energies from 0 to 50 eV and can be classified into three types as illustrated in Figure 3.15. The SE1 are emitted by the interaction with the beam electrons, localized near the beam impact point. To collect these electrons, an In-lens detector is placed on top of the final pole piece in the SEM chamber. The SE1 electrons are intercepted by the weak electrical field at the sample surface, then accelerated to high energy by the field of the electrostatic lens and focused on the annular In-lens detector inside the beam booster located above the objective lens. The SE2 are generated far from the beam impact point. The SE3 electrons, instead, are generated by the scattering of the BSE on the pole pieces of the microscope. The SE2 and SE3 are collected by the so-called Everhart and Thornley detector, located at a certain angle from the normal of the column. Secondary electron yield does not have a strong dependence on the sample atomic number and they are most widely used to image the surface topography of the sample.

A part BSE and SE, other signals can be generated in a SEM (Figure 3.14):

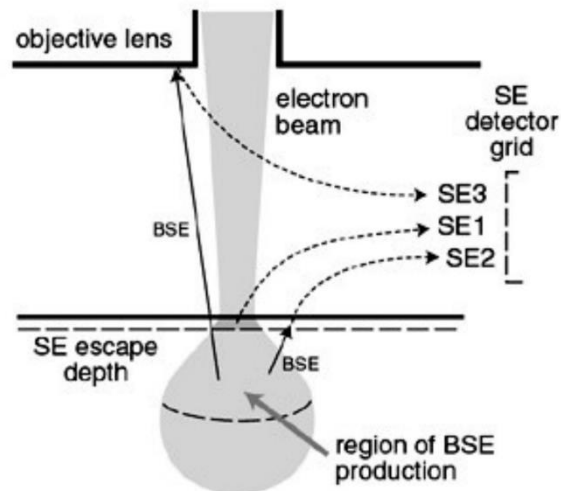


Figure 3.15: Spatial distribution of backscattered electrons, and secondary electrons of the I, II and III type.

- Electron Beam Induced Current (EBIC): when the primary electron beam is scanned on a semiconductor sample, electron-hole pairs are generated and if the generation occurs inside a depleted volume of the sample (p-n junction, Schottky barrier, ...) the charges are separated by the electric field and can be collected to form an electron beam induced current that can be used for imaging and semiconductor analysis;
- Cathodoluminescence: if electrons impact a luminescent material they cause the emissions of photons which may have wavelengths in the visible spectrum. They allow band structure analysis of semiconductors;
- Characteristic X-Rays and Auger electrons: if an impinging electron ionizes the atoms and an inner shell electron is emitted, an upper-level electron can fill the hole. The energy gained from the hole filling can be emitted as an Auger electron or an X-Ray photon. In both cases the emitted energy is characteristic of the atom and determined by the energy difference between the two states;

3.3.7. Hall measurements

The electrical characterization of the samples in this work has been done using an HL5500PC Hall system, from which the Sheet Resistance R_{sh} , the Hall mobility μ_e , and the carrier concentration n_e have been measured. The resistivity of the samples has been calculated after measurements, considering the thickness of each sample.

Samples for measurements have been shaped for a Van Der Pauw geometry. Thin films have been deposited on squared quartz substrates and four gold ohmic contact has been sputtered on the edge of the sample.

The experimental arrangement for the resistivity measurements is based on the van der Pauw's method. Van der Pauw developed a four-point probe configuration method, different from the four-point collinear probe arrangement to measure the resistivity of irregularly shaped samples.

Consider a square sample of a conducting material with contacts 1, 2, 3, and 4 along the edges. The current source is first applied to contacts 1,2 (I_{12}) and the voltage difference between contacts 4,3 (V_{43}) is measured (Figure 3.16). The current source is next applied to the contacts 1,4 (I_{14}) and similarly, the voltage difference between contacts 2,3 (V_{23}) is measured. The resistivity is then given by:

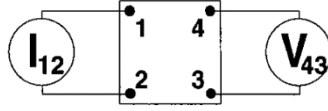


Figure 3.16: Resistivity measurement in Van Der Pauw configuration. The current is injected between two contact and the voltage difference measured on the two remaining. The same is repeated for six possible permutations of the indices.

$$\rho = \frac{\pi}{2 \ln(2)} t \left[\frac{V_{43}}{I_{12}} + \frac{V_{23}}{I_{14}} \right] F \quad (3.10)$$

where t is the thickness of the sample and F is a correction factor for geometrical asymmetry. If the sample is symmetrically shaped $F=1$. If the thickness of the specimen is unknown, it is possible to define the Sheet Resistance R_{sh} as follows:

$$R_{sh} = \frac{\rho}{t} \quad (3.11)$$

The system measures the sheet resistance by injecting the same current I for all six possible permutations obtained by rotation of the indices and the voltage difference across the contacts is measured for both current directions and averaged⁸⁹.

Carrier concentration n_e and hall mobility μ_e are determined by measuring the Hall effect^{44,46} in an arrangement as shown in Figure 3.17. A magnetic field perpendicular to the sample surface is applied and a constant current I is injected at two non-adjacent contacts. The voltage difference is measured at the other two remaining contacts. For the Hall effect when a charged particle moves in presence of a magnetic field, it is subject to the Lorentz force proportional to the magnitude of the magnetic field and the particle velocity. The injected current perpendicular to the magnetic field pushes the free carrier to accumulate along one side of the sample originating a voltage difference, called *Hall voltage*, given by:

$$V_H = \frac{IB}{n_e e t} \quad (3.12)$$

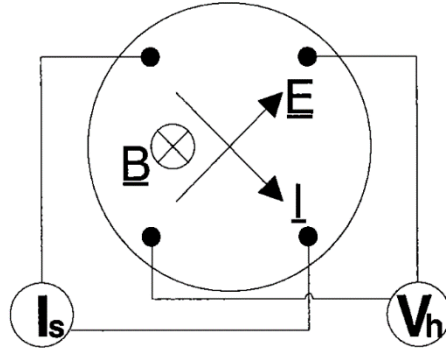


Figure 3.17: Hall effect measurements configuration.

where B is the magnetic field intensity, n_e is the carrier concentration and e and t are the electron elementary charge and the film thickness respectively. For an average value of V_H , different permutations of contacts, current, and magnetic field directions are measured.

The measured V_H allows to define the Sheet Hall coefficient for samples with unknown thickness:

$$R_{Hs} = \frac{V_H}{IB} \quad (3.13)$$

then the sheet carrier density n_{es} (cm^{-2}) is computed as a result of a combination of equation 3.12 and equation 3.13. The bulk carrier density n_e (cm^{-3}) is then obtained for a known thickness.

The calculation for the Hall mobility is possible after the sheet resistance and sheet Hall coefficient measurements and is given by:

$$\mu_H = \frac{R_{Hs}}{\rho_s} \quad (3.14)$$

3.3.8. Transmittance and reflectance measurements

The optical characterization of the samples has been performed with a Varian Cary 500 double beam scanning UV-VIS-NIR spectrophotometer to collect transmittance and specular reflectance spectra.

When electromagnetic radiation travels from one medium to another, can be absorbed, transmitted, or reflected. Named I_0 the intensity of the incident beam, it is represented by the sum of the transmitted intensity I_T , absorbed intensity I_A , and reflected intensity I_R ⁹⁰:

$$I_0 = I_T + I_A + I_R \quad (3.15)$$

Hence, the following quantities can be defined:

- Transmittance, defined as $T = \frac{I_T}{I_0}$ which represents the portion of transmitted light;
- Absorbance, defined as $A = \frac{I_A}{I_0}$ which represents the portion of absorbed light;
- Reflectance, defined as $R = \frac{I_R}{I_0}$ which represents the portion of reflected light;

A spectrophotometer can quantitatively measure the portion of light that can be transmitted and reflected, as a function of the wavelength, when travelling from one medium to another. A schematic representation of a double-beam spectrophotometer is represented in Figure 3.18⁹¹. The system is equipped with several spectroscopic components:

- light sources: a tungsten halogen lamp for the VIS and NIR portion of the electromagnetic spectrum and usually a deuterium lamp for the UV part of the electromagnetic radiation.
- monochromators containing gratings or prisms;
- optical imaging equipment such as lenses, mirrors, fibers, etc..;
- detectors;

Spectrophotometers may be either single-beam, in which the light beam takes a single fixed path and the measurements are done with and without the sample present, or double beam, in which the light is made to pass through two paths, one containing the sample and the other one containing a reference to compare the intensities.

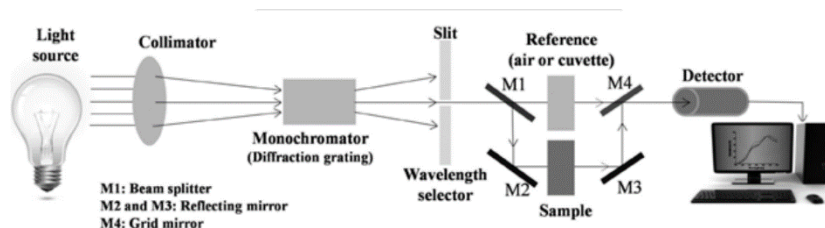


Figure 3.18: Double-beam spectrophotometer components.

Light is taken either from a tungsten or a deuterium lamp by moving a mirror to an appropriate position. All the rays coming from the sources are collected by the collimating convex lens and focused on the entrance of a monochromator. The light is dispersed by the diffraction grating inside the monochromators and is used to select the light beams of a specific wavelength from the light source. The beam is divided into two by an array of divided mirror elements. A chopper disc driven by a motor allows light to pass through only one beam at a time. Both beams are directed to a diffuser and then the signal is switched appropriately to sample or reference by a driven chopper. Then the intensities are compared for transmittance measurements.

Reflectance is measured by shining light on a sample and measuring the light reflected from the sample. Reflected light consists of specular reflected light and diffuse reflected light. The total reflected light is the sum of the two components. The specular reflected light is the light reflected at the same angle as the incident angle. The diffuse reflected light is the diffuse light reflected in all directions from rough surfaces. Specular reflectance measurements are usually performed using an appropriate attachment for the spectrophotometers. Diffuse reflectance is measured by using another appropriate attachment called *integrated sphere* to measure the diffuse reflected light while specular reflected light is excluded. In this work, only specular reflectance spectra have been acquired.

3.4. Devices

TCOs presented in this work have been developed to be implemented as transparent electrodes for photovoltaic applications. In order to test the electrode performances, TCO has been deposited on bi-facial SHJ solar cell devices supplied by Enel 3SUN company for the BEST- 4U project, co-financed by PON Ricerca e Innovazione 2014-2020. The objective of the BEST-4U project is the fabrication of a 4-Terminal bi-facial Tandem - Silicon Heterojunction solar cell for utility scale. A schematic representation of the cells is represented in Figure

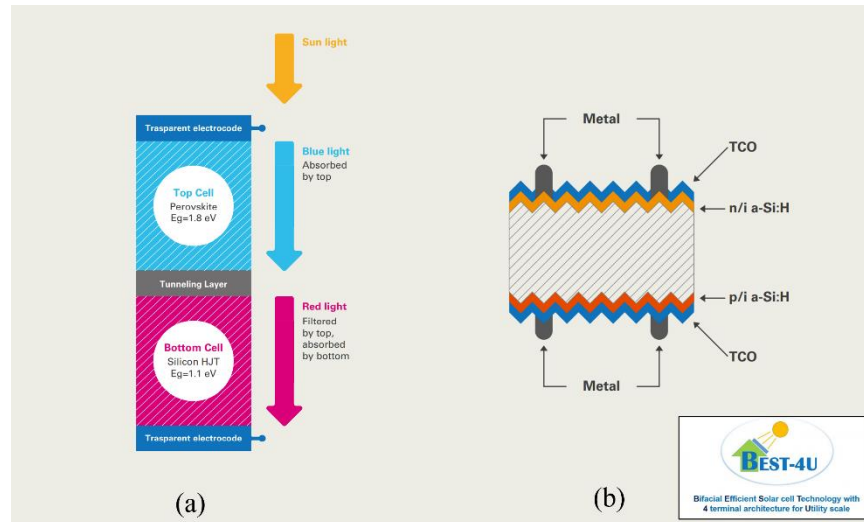


Figure 3.19: Tandem solar cell scheme (a); schematic representation of the bifacial Si-HJT solar cell (b).

3.19a⁹². The cell has a bi-facial Si heterojunction cell as bottom cell and a wide bandgap semiconductor cell as top cell. The top cell collects the blue region of the incident solar spectrum. The bottom cell collects the red and IR part of the spectrum passed through the top cells and, on the backside, the albedo light scattered by the ground. The four-terminal model proposed for the module has some advantages compared to the standard tandem cells with 2 cells connected in series, as the limitations due to lattice parameter matching and current matching. The four terminal structure presents more degrees of freedom.

This work presents some results for the improvement of the bottom silicon cells. A schematic representation of the bottom cells is reported in Figure 3.19b⁹². Enel 3SUN provided the semi-finite Silicon Heterojunction solar cells, before the TCO deposition. The TCOs deposition has been done in the aim of this work and External Quantum Efficiency Measurements have been performed as explained in the next paragraph.

3.4.1. External Quantum Efficiency measurements

For a photovoltaic cell, the quantum efficiency (QE) is the ratio of the number of carriers that are collected by the solar cell and the number of photons reaching the solar cell. There are two types of quantum efficiency: internal quantum efficiency (IQE) and external quantum efficiency (EQE). The EQE does

not includes the reflection losses of the solar cells, whereas IQE is corrected for the optical losses due to reflection at the front of the solar cell.

The QE can be expressed as a function of the wavelength or the energy of photons. It is affected by the photogeneration of electron-hole pairs and by the collection efficiency of these electron-hole pairs. If all photons at a certain wavelength are absorbed and all the resulting minority carriers are collected, then the QE at that particular wavelength should be the unity. Ideally, QE curve is represented with a square-line shape, and goes through zero at long wavelengths, below the bandgap, where no light is absorbed. For most solar cells, the QE is reduced due to recombination effects. At low wavelengths, the QE is typically below the unity due to the recombination at the front surface of the solar cell. Then, since the blue light is absorbed very close to the surface, high surface recombination will affect the blue portion of QE. The green light is absorbed in the bulk of the solar cell and low diffusion length, for example, will affect the collection probability from the solar cell bulk, reducing the QE in the green part of the spectrum. Rear surface recombination instead, will reduce the absorption at long wavelength reducing the response for the red portion of the spectrum.

EQE measurements have been performed with an experimental set-up as illustrated in Figure 3.20⁹³⁻⁹⁶ and formed by different components:

- a monochromator
- a thermostatic chuck
- a PC connected to the monochromator through a wavelength controller. The responsivity and the EQE trends of the solar cell have been scanned and acquired for each wavelength
- a c-Si reference PV cell used to calibrate the EQE detection system

The EQE spectra have been calculated first acquiring the spectral response of the solar cell. The spectral response (SR) is the ratio of the current generated by the solar cell to the power incident on the solar cell. EQE and SR are linked by the following equation:

$$SR = \frac{q\lambda}{hc}EQE \quad (3.16)$$

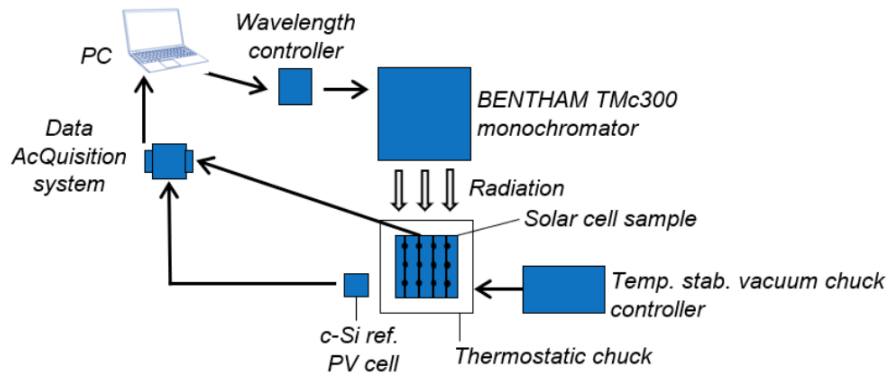


Figure 3.20: Experimental set-up for EQE measurements.

4. Structural, optical, and electrical characterization of ITO films co-doped with Molybdenum

4.1. Introduction

Tin-doped Indium oxide (ITO) is the most used TCO, offering a low electrical resistivity combined with a good transmittance for visible and NIR (near infrared) light. Because of the usual lowering of the optical transparency with increasing the electrical conductivity, the choice of a TCO for a specific application is always based on the best compromise between these two properties. In the last years, however, the demand has extended beyond conductivity and transparency, for which indeed higher performances are more and more required. Other critical issues are long-term stability, low cost, high abundance of raw materials, sustainability of the fabrication processes, use, and recycling.. Driven by these needs, there has been an increasing research activity on these materials, to find novel TCOs with improved properties. Although Transparent Conductor Materials (TCM) include TCO/Metal/TCO multilayer structures^{16–18,66}, Carbon nanotubes⁹⁸, metallic nanowires^{29,30},³⁰conductive polymers^{34,35}, and graphene^{37,99}, all these alternatives are still far from industrial applications and large scale production cycles⁶⁹.

Thus, while searching for new TCM, it is extremely important to improve conventional TCOs which can be implemented in the present industrial processes. Among them, Indium-Tin-Oxide (ITO) is probably the most used one, mainly in the photovoltaic (PV) industry. Focusing on Indium-based TCO, transition metals have been proposed as promising dopants for In_2O_3 . In the case of ITO, the strong hybridization between In and Sn 5s orbitals at the bottom of the conduction band of the In_2O_3 can renormalize its band curvature, so reducing the mobility due to an increase of the electron effective mass. On the contrary, when a transition metal (TM) is introduced as a dopant, the hybridization between the TM d levels and In

5s states is weak and the band curvature around the conduction band minimum is maintained, the electron effective mass decreases, and, consequently, the carrier mobility increases⁴³.

Recently, there has been a growing interest in searching for the best TM dopants for In₂O₃. Among them, Molybdenum has attracted attention due to its dual doping behavior depending on the occupied site in the In₂O₃ lattice. The crystalline structure of many TCO based on indium oxide is that of the In₂O₃ bixbyte structure, with two inequivalent sites for Indium, labeled *8b* and *24d*, characterized by body-diagonal and face-diagonal placement, respectively, of the oxygen structural vacancies in the first shell around In⁴⁰. In the In *8b* substitutional site, Mo acts as a deep donor with no doping effect. On the other hand, when Mo is located in the *24d* site, it creates a shallow level promoting one electron to the conduction band. Furthermore, because of the small hybridization between Mo 4d states and In 5s states, the ionized impurity scattering in the *24d* configuration is strongly reduced, with a consequent enhancement of electron mobility. It is worth noting, however, that the *24d* sites are metastable and temperature dependent^{61,100}.

As reported in the literature, Mo doped Indium Oxide (IMO) thin films are mainly grown by magnetron sputtering¹⁰¹⁻¹⁰³, thermal reactive evaporation¹⁰⁴, aerosol-assisted chemical vapor deposition¹⁰⁰, high-density plasma evaporation¹⁰⁵ and pulsed laser deposition¹⁰⁶. Several studies have shown that IMO thin film properties are also strongly influenced by the substrate temperature, oxygen partial pressure during the growth¹⁰¹, and post-deposition thermal treatments¹⁰⁷. Moreover, theoretical calculations suggest that defect density in the metastable configuration (Mo in the *24d* sites), can be increased with temperature during or after the deposition⁶¹.

The amount of Mo in IMO reported in theoretical and experimental studies^{106,108,109} is around 2-3%, while ITO is usually obtained with Sn/In 10% atomic in the SnO₂+In₂O₃ alloy. By considering the good performances of standard ITO, the low amount of Mo needed to dope In₂O₃, and the fact that, in ITO, Sn occupies the *8b* site, leaving the *24d* available for Mo, we decided to perform a preliminary study on the effect of Mo co-doping in ITO.

In this chapter we report, for the first time to our knowledge, the growth and characterization of ITMO⁹⁷ (In-Sn-Mo-oxide) thin films obtained by Mo and ITO co-sputtering deposition. We give evidence of the role of thermal annealing on the structural, optical, and electrical properties of the material, finding a drastic improvement at $T \geq 300$ °C with respect to the as-deposited film. In particular, the role of Mo as an active co-dopant already at room temperature is demonstrated by a very high concentration of electrons in the conduction band, while the main effect of the thermal processes is the annealing of defects with a consequent increase of the optical transmittance and carrier mobility.

4.2. Experimental

Molybdenum doped Indium Tin Oxide (ITMO) thin films were deposited on soda lime glass substrates by RF and DC magnetron co-sputtering using ITO (Sn/In 10% atomic in $\text{SnO}_2+\text{In}_2\text{O}_3$ alloy) and pure Mo targets (2-inch diameter) 99.99 % pure. Depositions were performed at room temperature in Ar atmosphere with a gas flow of 6 sccm, at a working pressure of 1 Pa. The sputtering power was 45 W for ITO (in RF mode) and 50 W for Mo (in DC mode), with the sample holder in rotational motion to obtain a good thickness and uniform composition on a 4 x 4 cm² area. Several ITMO films were obtained in a single deposition process by mounting small glass substrates side by side. The nominal thickness was 75nm, and 4 different thermal processes at 200 °C, 300 °C, 400 °C, and 500 °C in vacuum for 1h were done after the deposition to check the effect on the electrical and optical properties. To highlight the effects of Mo as a co-dopant, we also report the optical and electrical data of ITO films, 100 nm thick, deposited with the same process parameters.

Rutherford Backscattering Spectrometry (RBS) was employed to quantify the doses of the chemical elements in the films and to convert them into thickness by using the atomic density of the materials. A 2.0 MeV He⁺ ion beam at normal incidence with the backscattered ions detected at an angle of 165° was used. SimNra software was employed to simulate the RBS spectra for the quantitative analysis.

Sheet-resistance R_{sh} , Hall mobility μ_e , and carrier concentration n_e were measured by a 4-point probe in the Van der Pauw configuration at room temperature.

A Varian Cary 500 double beam scanning UV-VIS-NIR spectrophotometer was used to measure the direct optical transmittance (T) and specular reflectance (R) in the 250-2500 nm wavelength range. Transmittance (T) spectra in normal incidence were collected with a 100% baseline obtained without sample, while the reflectance (R) spectra have been detected in specular geometry at 20° using a calibrated standard.

Finally, angle integrated X-ray photoelectron spectroscopy (XPS) spectra were recorded using Mg K α X-ray source to study the Mo chemical states. The overall energy resolution in our experimental conditions was 1.2 eV, with a precision of 0.1 eV on the peak position.

4.3. Results and discussions

4.3.1. RBS Analysis

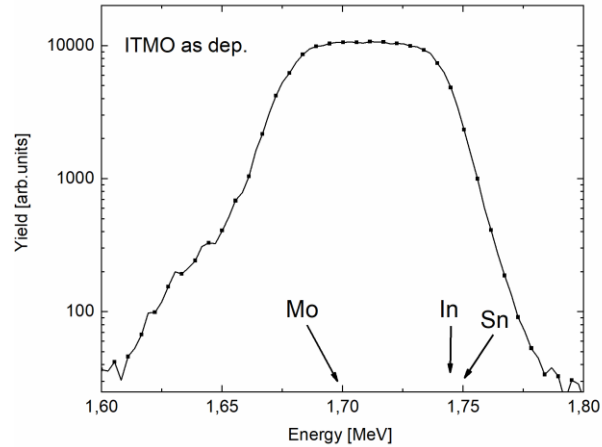


Figure 4.1: RBS spectrum in semi-log scale of the as-deposited ITMO sample. Only the RBS region of Sn, In and Mo signals is shown for clarity. Arrows indicate the position of the elements at the surface.

Figure 4.1 shows the RBS spectra of the as-deposited ITMO sample in a semi-log scale vs. the He^+ backscattered energy in the region of Sn, In, and Mo. Due to the superposition of the signals, the semi-log scale allows us to clearly see the presence of the small amount of Mo (less than 2%) in the ITO matrix. While arrows in Figure 4.1 indicate the backscattered energy due to Sn, In and Mo surface atoms respectively, the shoulder on the left side of the RBS signal is evidence of the presence of Mo atoms distributed in the film. Indeed, the shoulder is not visible when the linear y scale is used in Figure 4.2, where the spectra of the as-deposited and annealed ITMO samples are reported.

RBS data were also used to estimate the thickness of the films by using the atomic areal density (atoms/cm^2) of the chemical elements used in the SimNra simulation program, and the ITO atomic density ($d_{\text{ITO}} = 7.7 \times 10^{22} \text{ at}/\text{cm}^3$). By considering the small amount of Mo in the alloy (less than 2%), and the uncertainty of the RBS technique (about 5-10%), we assumed for the ITMO, the same atomic density as the ITO. The estimated thickness of the as-deposited sample is equal to the nominal one (75 nm) within the experimental uncertainty of the technique, as well as the expected stoichiometry of the alloy. A clear effect of

4. Structural, optical, and electrical characterization of ITO films co-doped with Molybdenum

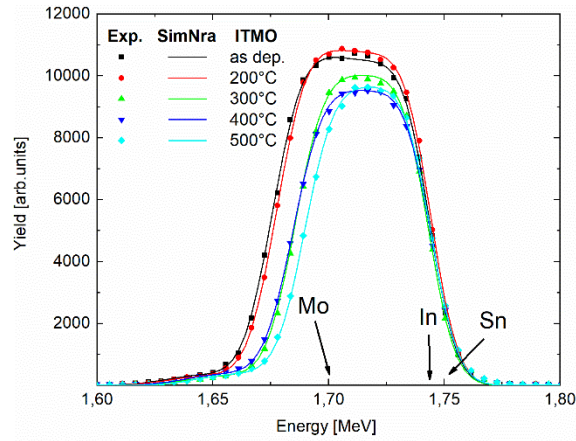


Figure 4.2: RBS spectra of He^+ ions backscattered by ITMO samples as deposited and after annealing at 200 °C, 300 °C, 400 °C and 500 °C for 1h. Continuous lines are the output of the SimNra simulation program used to calculate the atomic areal density of the chemical elements.

the thermal annealing processes is the loss of Indium (between 3% and 6%) with a simultaneous increase of the Oxygen content, while no changes were detected for Mo and Sn. The out-diffusion of In during thermal treatments has been confirmed by XPS and discussed in more detail in the section dedicated to that analysis. As a consequence of the indium loss, a decrease of a few nm in thickness is also observed, as also highlighted by the intensity and wideness decreasing of RBS signals in Figure 4.2. On the other hand, Mo and Sn remain stable after all thermal processes. Data obtained by RBS are listed in Table 4.1.

Table 4.1: Thickness and percentage of the element in ITMO samples.

ITMO	Thickness (nm ± 5)	Mo (%)	Sn (%)	In (%)	O (%)
as-deposited	75	1.9	3.5	36.3	58.3
200°C	71	1.8	3.5	38.0	56.7
300°C	65	1.8	3.5	33.3	61.4
400°C	69	1.9	3.5	30.4	64.2
500°C	62	1.9	3.5	31.3	63.3

4.3.2. XPS Analysis

Figure 4.3 shows the XPS spectra (black lines) and deconvolution (colored lines) of Mo $3d_{3/2}$ and $3d_{5/2}$ spin-orbit doublet for the as deposited sample (Figure 4.3a) and annealed at 400 °C (Figure 4.3b). After the background subtraction, three contributions due to different oxidation states can be identified: the Mo^0 at the lowest binding energy (magenta peaks), the Mo^{4+} (green peaks) due to MoO_2 , and the Mo^{6+} at the highest binding energy (blue peaks) corresponding to MoO_3 . The red curves in Figure 4.3 are the sum of the three Mo components, showing a very good agreement with the experimental spectra. The fit of the signals has been performed by using a mixed Gaussian-Lorentzian peak function, keeping the spin-orbit energy splitting at 3.15 eV and the intensity ratio $I_{5/2}/I_{3/2} = 1.5$ for all the oxidation states. For each sample, the only free fitting parameters were the absolute energy position and intensity of the $3d_{5/2}$ peaks, and the Full-Width Half Maximum (FWHM). However, we used the same FWHM for samples before and after thermal annealing to minimize the number of free parameters.

By keeping into account the constant amount of Mo in our samples (as also verified by RBS), the most evident effect by comparing Figure 4.3a and 4.3b is the conversion of Mo^0 and Mo^{4+} into Mo^{6+} oxidation state, which was already the major chemical configuration in the as-deposited sample as quantitatively reported in Table 4.2. In detail, after thermal annealing at 400 °C, we see that only 1% of Mo is not oxidized yet, with 88% in the Mo^{6+} state.

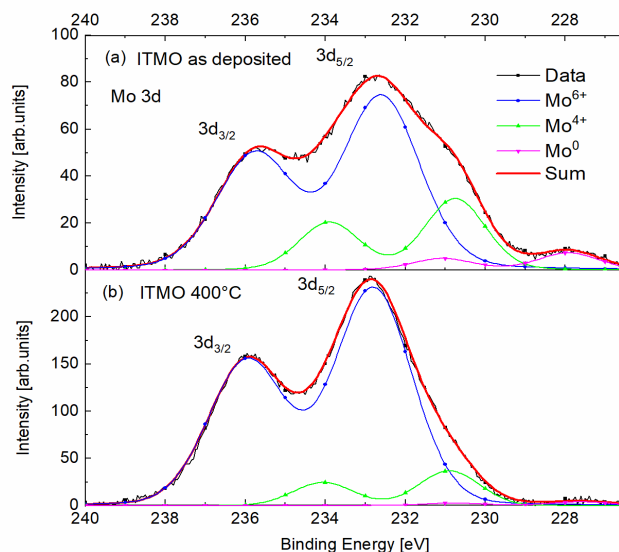


Figure 4.3: XPS spectra of Mo 3d region in as deposited (a) and 400 °C annealed (b) ITMO samples.

4. Structural, optical, and electrical characterization of ITO films co-doped with Molybdenum

Table 4.2: Percentages of Mo⁰, Mo⁴⁺, Mo⁶⁺ oxidation state as obtained by XPS measurements for the as-deposited and annealed (400 °C for 1h) samples.

	Mo ⁰ (%)	Mo ⁴⁺ (%)	Mo ⁶⁺ (%)
As dep	5.73	22.67	71.60
400 °C	1.13	10.66	88.21

The loss of In during thermal annealing has also been detected by XPS. In Figure 4.4 we report the Sn 3d and In 3d spectra for the same samples of Figure 4.3a-b, i.e. as-deposited and annealed at 400 °C. The peak heights have been normalized to the Sn ones to compare the relative intensities of the signals and to detect the eventual variation of In percentage in the alloy already discusses in the RBS section. The quantitative analysis of the peak ratio is reported in the inset of Figure 4.4 and it indicates that after annealing (red data) the In amount decreases about 50% with respect to Sn. Although RBS gives an average value of 6% of In loss after 400 °C for 1h (see Table 4.2), the value of 50% obtained by the XPS is consistent if we take into account the different depths probed by the two techniques. Indeed, while RBS analyzes the entire volume of the film from the surface to the substrate, XPS (in our experimental conditions) is sensitive only to about the first 9 nm from the surface. For this reason, the reduction of 50% of In detected by XPS in the near-surface region of the film agrees with the 6% indicated by RBS on the entire volume, as confirmed by simply comparing the two % values with the inverse of the corresponding probed depths:

$$\frac{50\%}{6\%} = 8.3 = \frac{75 \text{ nm}}{9 \text{ nm}} \quad (4.1)$$

confirming that the majority of the In lost during thermal annealing in vacuum comes from the near-surface region. The reason for the In loss during thermal processes has not been further investigated in this work but it is very likely due to the presence of metallic In, whose melting point is only 156 °C, in the as-deposited film. Indeed, the co-deposition of ITO and Mo in a pure Ar atmosphere (no O₂ gas flow) causes the subtraction of oxygen atoms from ITO to form MoO₂ and MoO₃, as clearly observed by XPS. Thus, some In deprived of oxygen will probably evaporate from the near-surface region in the initial stage of the thermal processes. The poor vacuum condition in the oven (P =10⁻² mbar) during the annealing will then supply extra oxygen, as also in fact seen by XPS.

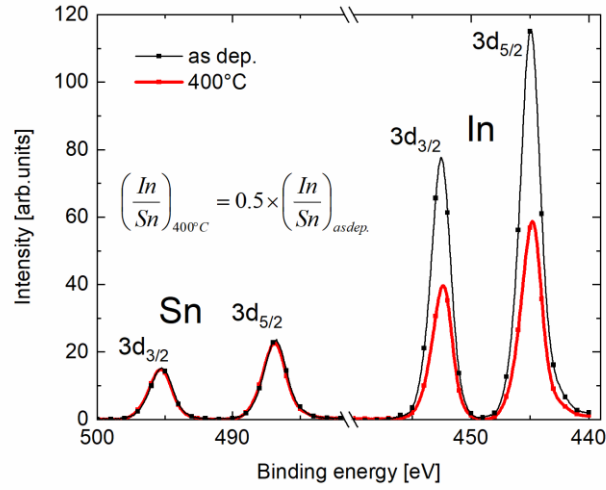


Figure 4.4: Sn and In 3d peaks before (black) and after (red) thermal annealing normalized at the same Sn intensity.

4.3.3. Optical properties

In Figure 4.5 we report the optical analyses of all ITMO samples and, as a comparison, a set of 3 ITO samples grown by our group in the same experimental conditions. In particular, Figure 4.5a-b shows the transmittance spectra and the Tauc plots, respectively, for ITMO, while in Figure 4.5c-d the same parameters for ITO. The average values of the transmittance calculated in the range 380-750 nm and the optical band gap calculated by Tauc analysis are reported in the *legenda* of the figures. In more detail, the optical band gap of Figure 4.5b-d was calculated using Tauc's equation for indirect transitions as follows:

$$(E\alpha)^{1/2} = B(E - E_{gap}) \quad (4.2)$$

where B is the Tauc coefficient, α the absorption coefficient, and E is the photon energy. In this way E_{gap} is obtained from x axis intercept of the curve fitted on the linear portion of the Tauc plot. For our samples α has been extracted by using the following equation¹¹⁰:

4. Structural, optical, and electrical characterization of ITO films co-doped with Molybdenum

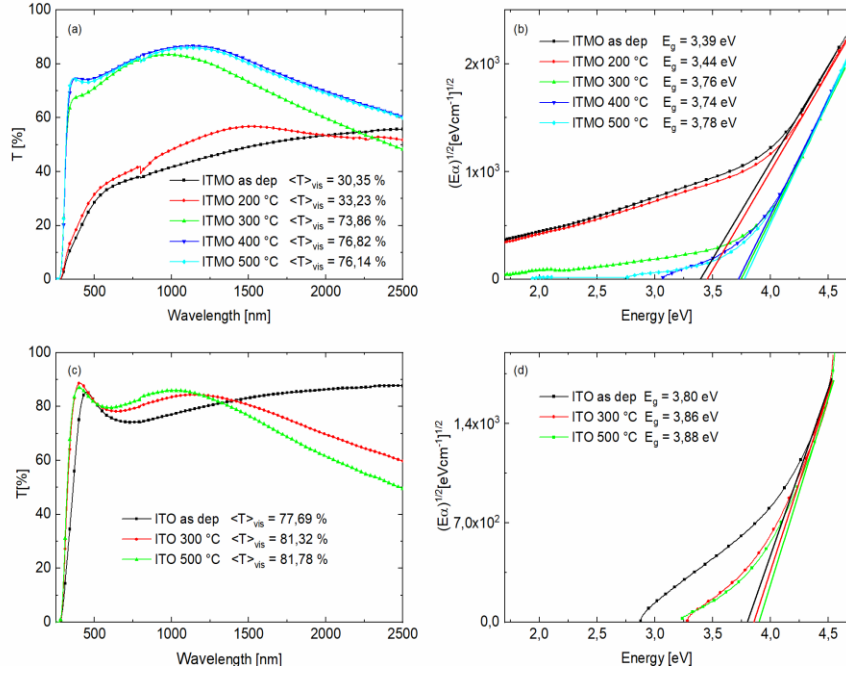


Figure 4.5: Optical transmittance spectra (a, c) and Tauc Plot (b, d) of ITMO and ITO films. The average values of transmittance in the visible range and the values of the optical energy gap are reported within the figures.

$$\alpha = \frac{1}{d} \ln \frac{T_G(1 - R_S)}{T_S} \quad (4.3)$$

where d , T_S , and R_S are the thickness, transmittance, and reflectance of the sample respectively, while T_G is the transmittance of the glass substrate. The optical transmittance of ITMO shows a drastic improvement for thermal treatments at $T \geq 300 \text{ }^\circ\text{C}$ (from 30% to 77% mean value in the visible range), corresponding to the temperatures for which also RBS and XPS have indicated a strong variation of the structural and chemical status of the films. In addition to the variations of the transmittance and optical energy gap, a clear decrease in the Tauc plot of Figure 4.5b is also observed for the low energy region after thermal treatment at $300 \text{ }^\circ\text{C}$. Such a reduction can be attributed to the suppression of the Urbach tails in the band structure (energy states within the gap) which are due to structural defects⁵⁵. This is also in full agreement with the improvement of the

electrical properties after thermal annealing, as discussed below. Concerning the ITO films reported for comparison in Figure 4.5c, we observe a high transmittance overall in the investigated range before thermal processes, with a strong reduction at the infrared wavelengths once annealed. This is due, as clearly demonstrated by the electrical measurements in the next section, to the promotion of free electrons in the conduction band upon thermal processes.

4.3.4. Electrical properties

Further characterization of our films was done by using a 4-point probe in the Van der Pauw configuration at room temperature to obtain the sheet resistance R_{sheet} , the carrier mobility μ , and concentration n . From R_{sheet} and film thickness, the resistivity ρ was calculated and reported in Table 4.3 along with μ and n for ITMO, ITO, and one IMO sample taken from the literature.

As for the majority of TCO, also ITMO benefits from thermal annealing processes, showing in all cases a reduction of the sheet resistance and an increase in carrier mobility. Moreover, in full agreement with the results of all the other characterizations, a strong improvement at 300 °C is observed for ρ , its value decreases by a factor of 30 with respect to the as-deposited film and by a factor of 10 with respect to that annealed at 200 °C. A lowering of the resistivity is usually

Table 4.3: Resistivity, mobility, and carrier concentration for ITMO, ITO, and IMO films.

TCO	T (°C)	ρ (Ωcm)	μ ($\text{cm}^2 \text{V}^{-1} \text{s}^{-1}$)	n (cm^{-3})
	R.T.	4.89×10^{-2}	0.03	4.84×10^{21}
	200	1.65×10^{-2}	0.64	5.91×10^{20}
	ITMO	300	1.44×10^{-3}	12.3×10^{20}
	400	1.44×10^{-3}	5.03	8.46×10^{20}
	500	1.07×10^{-3}	6.40	9.14×10^{20}
	R.T.	2.02×10^{-1}	4.07	7.59×10^{18}
	ITO	300	8.46×10^{-4}	8.57×10^{20}
	500	3.57×10^{-4}	11.3	1.55×10^{21}
IMO 107	R.T.	$\approx 4 \times 10^{-3}$	≈ 40	$\approx 4 \times 10^{19}$

due to higher carrier mobility, carrier concentration, or both. In our case (the last two columns on the right side of Table 4.3) it is clear as the mobility μ rises with the temperature of the annealing, while the same trend is not observed for the concentration n , whose values oscillate without following a clear trend. By these data, we can thus state that the main reason for the lowering of the resistivity is the enhancement of the mobility due to the annealing of defects with the thermal processes, as already highlighted in the discussion of the Tauc plot of Figure 4.5. Moreover, the carrier concentration of ITMO is very high in all samples, and in particular much higher in the as-deposited film with respect to ITO and IMO¹⁰⁷. This behavior agrees with the optical transmittance of ITMO, showing a low value in the infrared region for all samples (Figure 4.5a), due to plasmonic resonance effects. On the other hand, ITO shows an increase in the carrier concentration, and the consequent lowering of the optical transmittance, only after thermal annealing (Figure 4.5c). The high values of n demonstrate that Mo in the ITO matrix acts as an efficient dopant already during the deposition at room temperature, while the high resistivity and low mobility are mainly due to structural defects which are partially removed during post-deposition thermal processes, as also suggested by the partial suppression of the Urbach tails reported in Figure 4.5b.

4.4. Conclusions

The work reported in this chapter is a first attempt, to our knowledge, of improving the electro-optical performances of ITO by Mo co-doping. The starting idea was to combine the very good and well-consolidated properties of ITO films deposited by sputtering with the promising properties of In₂O₃ doped with Mo (IMO). In particular, Mo in IMO is known to act as an efficient donor only when located in the substitutional In *24d* metastable lattice site, while Sn in ITO preferentially occupies the substitutional In *8b* position^{111,112}. For this reason, Mo in ITO should have a higher probability of sitting in the *24d* sites with respect to Mo in IMO. We also show as Mo in ITO tends to form the MoO₃ oxide (72% during deposition and 88% after annealing), which also helps in getting electrons in the conduction band. Our experimental work has shown that already at room temperature the free electron concentration in ITMO is much higher with respect to ITO and IMO, and that post-deposition thermal annealing drastically improves both electrical and optical properties due to the recovery of structural defects. An instability of In during thermal processes has also been revealed, with an important out-diffusion of this element from the near surface region of the films probably caused by the oxidation of Mo and the consequent reduction of In. The limited electrical properties of our ITMO films can be attributed to the presence

4.4 Conclusions

of defects that are partially removed once thermally processed. Nevertheless, also 2% of Mo in ITO could be too high a concentration by considering the contemporary presence of Sn as dopants.

5. Zr-doped Indium Oxide thin films as transparent electrodes for photovoltaic applications

5.1. Introduction

Transparent electrodes are a necessary component in many modern devices such as solar cells, electrochromic mirror windows, flexible OLED, low emissivity windows, touch panel displays, and electromagnetic shielding. Traditionally, this role has been well served by TCOs, characterized by a good transmittance for the visible and near-infrared light and low electrical resistivity. However, the demand has extended beyond conductivity and transparency, for which indeed higher performances are required, but it also includes long-term stability, low surface roughness, suitable work function, high mechanical flexibility, high-temperature resistance for the annealing process, the abundance of raw materials and low fabrication costs^{40,53,113}. Within this class of materials, Sn-doped Indium Oxide or ITO is mostly favored because it is an n-type, highly degenerate, wide bandgap semiconductor that offers the highest available transmissivity for visible light combined with the lowest electrical resistivity. However, it also presents multiple drawbacks such as high cost of materials due to scarcity of Indium, low NIR transmittance, brittleness with the occurrence of cracks under mechanical stress, and limited application in flexible optoelectronic devices: the sputtering process for ITO coating is typically conducted at high temperatures and results in sheet resistances below $20 \Omega/\square$ at 90% transmittance; whereas, when a flexible plastic substrate is used, ITO is preferably deposited at lower temperatures to prevent any damage to the substrate, with the corresponding increase of the sheet resistance^{69,114}.

The aim is to reduce Indium consumption, through different basic strategies that can be classified into three types. The first concern is the development of In-free TE, as In-free TCO (AZO or AZO/Ag/AZO multilayer structures)^{17,18,66,67,115}, conductive Polymers as PEDOT PSS³⁴ or nanostructured metals as metallic NWS and metal grids^{29,68,116,117}, and carbon nanotubes⁶⁹.

The second possibility moves toward the recycling of Indium from old Perovskite solar cells or sputtering deposition waste (from ITO deposited on the equipment or unused target). However, while searching for new TCM approaches and materials, it is extremely important to improve conventional TCOs which can be implemented in the present industrial processes. To circumvent these limitations, we focused on the third solution of reducing TCO thickness from the 100 nm thickness standardly used in solar cells down to 15-20 nm. It must be noticed that the thickness of the TCO is also optimized to minimize the reflection of the visible light due to interference multilayer effects. Thinner TCO could worsen this effect, but this could also be eventually avoided by adding anti-reflective coating materials such as SiO_x, or SiN to reach an optimal light absorption^{71,118}.

The most relevant challenge when decreasing the thickness is to keep a low sheet resistance. Thus, the strategy is to look for Indium Oxide dopants that can lower the resistivity of the material through an enhancement of the carrier mobility.

For ITO, the strong hybridization between In and Sn 5s orbitals at the bottom of the conduction band of the In₂O₃ enlarges the band curvature, reducing the mobility due to an increase of the electron effective mass. In the dispersion relation, the reciprocal of the effective mass is proportional to the curvature of the band, the smaller the effective mass value, the sharper the curvature of the band is. For this purpose, Transition Metals have been proposed as promising dopants for In₂O₃. When a transition metal (TM) is introduced as a dopant, the hybridization between the TM *d* levels and In 5s states is weak and the band curvature around the conduction band minimum is maintained, leading to an electron effective mass lower than for ITO, with consequent higher carrier mobility. In terms of ground-state electronic structure, TM dopants can be generally classified into three types. For Type-I donors, n-type doping cannot be achieved at room temperature (Ti, V, Cr, and Mo) because the defect levels are significantly lower in energy than the CBM of In₂O₃. For Type-II donors (Nb and W) the defect levels are above the CBM of In₂O₃, but because they are not high enough in energy, n_e and μ_e values will be low. For Type-III donors (Zr, Hf, and Ta), the defect levels are sufficiently high in energy above the CBM of In₂O₃, so that TM dopants can be fully ionized, acting as shallow donors, and the m_e can be largely maintained; therefore, ideal n-type doping could be realized with high μ_e and n_e ⁴³.

In this chapter we describe the growth and characterization of Zr-doped In_2O_3 thin films. As reported in the literature, Zirconium doped Indium Oxide (IZrO) thin films are mainly grown by magnetron sputtering^{45,119-122} with a very low Zr concentration (Zr = 2 wt%) showing very promising opto-electrical performances.

A preliminary study has been conducted with different Zr at% to evaluate the best donor concentration for the highest mobility and optical transmittance. Then, fixing the Zr at%, the opto-electrical properties have been studied as a function of the thickness, from the standard values of 100 nm used in solar cells down to 15 nm. Ultra-thin films were deposited at Room Temperature followed by post-deposition thermal treatment at $T = 200\text{ }^\circ\text{C}$ to make the process compatible with Silicon solar cells and possible application in flexible devices.

5.2. Methods

Zirconium doped Indium Oxide thin films (IZrO) were deposited on high purity quartz glass materials (> 99,95 % - Spi supplies) and Si p-type substrates by RF and DC Magnetron co-sputtering technique from Zr and In_2O_3 target (2-inch diameter) supplied by Moorfield Nanotechnology, 99,99% purity. Depositions were performed at room temperature in a pure Argon atmosphere with a gas flow of 6 sccm and a working pressure of 1.6×10^{-2} mbar. A sputtering power of 45 W was used for In_2O_3 in RF mode and 57 W for Zr in DC mode. The sputtering system was used in a sputter-up configuration with a rotating sample holder to guarantee uniform thickness distribution and composition in a $4 \times 4\text{ cm}^2$ area. Two different sets of three samples were grown: the first set with different Zr at% concentration and the second one with different thickness. Post-deposition thermal annealing has been performed at $200\text{ }^\circ\text{C}$ for 30 minutes in ambient atmosphere.

Rutherford backscattering spectrometry (RBS) was employed to quantify the doses of the chemical elements in the films and to convert them into thickness by using the atomic density of the material. RBS measurements were performed using a Singletron ion accelerator with a 2.0 MeV He^+ ion beam at normal incidence with the backscattered ions detected at an angle of 165° . SimNra software was used to simulate the experimental RBS spectra collected for the quantitative analysis.

A Bruker Diffractometer 2D Phaser was used for X-Ray Diffraction measurements. The tool was operated at 30kV, 10 mA, at 2θ ($\text{Cu K}_{\alpha 1} = 0.15406\text{ nm}$, $\text{Cu K}_{\alpha 2} = 0.15444\text{ nm}$) from $10^\circ - 80^\circ$ at step = 0.010° .

Bruker Dimension Icon Atomic Force Microscopy was used for AFM measurements in a Peak Force Tapping Mode using a Silicon Nitride probe provided by Bruker (ScanAsyst-Air).

Bruker Dimension Icon Atomic Force Microscopy has been used in Peak Force Tapping mode for Frequency Modulated Kelvin Probe Force Microscopy measurements (FM-KPFM) to measure the work function of the samples. A PFQNE-AL heavily doped silicon probe, calibrated with a reference Au sample, was used to collect surface potential maps.

Sheet resistance R_{sh} , Hall mobility μ_e , and carrier concentration n_e were measured by a 4-point probe in the Van der Pauw configuration at room temperature with a Hall Effect Measurements System HL5500PC.

A Varian Cary 500 double beam scanning UV-VIS-NIR spectrophotometer was used to measure the direct optical transmittance (T) and specular reflectance (R) in the 250-2500 nm wavelength range. Transmittance (T) spectra in normal incidence were collected with a 100% baseline obtained without sample, while the reflectance (R) spectra have been detected in specular geometry at 20° using a calibrated standard. Tauc analyses were performed to determine the energy gap of the samples.

The detector responsivity and the external quantum efficiency of the samples were acquired through Bentham PV300 photovoltaic QE system. The experimental setup used for the EQE measurements consists of a monochromator, a thermostatic golden plated chuck, as a potential reference, a c-Si reference PV cell used for the calibration of the EQE detection system, a lock-in controller for modulating the light source's power and an electrical current measure unit. The samples, of square shape, were connected to the electrical current measure unit by a conductive tip and held in a fixed position by vacuum suction (see figure Xb) near the light spot (3x3 mm) to achieve the maximum current extraction. The samples' detector responsivity was acquired from 300 to 1100 nm with a step of 5 nm. The extracted current for each wavelength with its specific radiation power represents the detector responsivity (DR) of the sample. The DR is reported in $A \cdot W^{-1} \cdot nm^{-1}$ and the EQE trends of the solar cell samples are obtained from the DR by converting the radiation power into number of photons.

The surface samples morphology of textured SHJ solar cells with IZrO deposited as transparent electrodes, was investigated by field emission scanning electron microscopy (SEM) using a Zeiss Supra 25 microscope operating at 1.0 kV in InLens operation mode.

5.3. Results and discussions

5.3.1. RBS Measurements

Rutherford Backscattering Spectrometry (RBS) spectra of IZrO thin films as-deposited with different atomic Zr at % are shown in Figure 5.1. The Figure shows the semi-log scale of RBS Yield vs. the energy of the backscattered He⁺ ions in the region of interest with Zr and In.

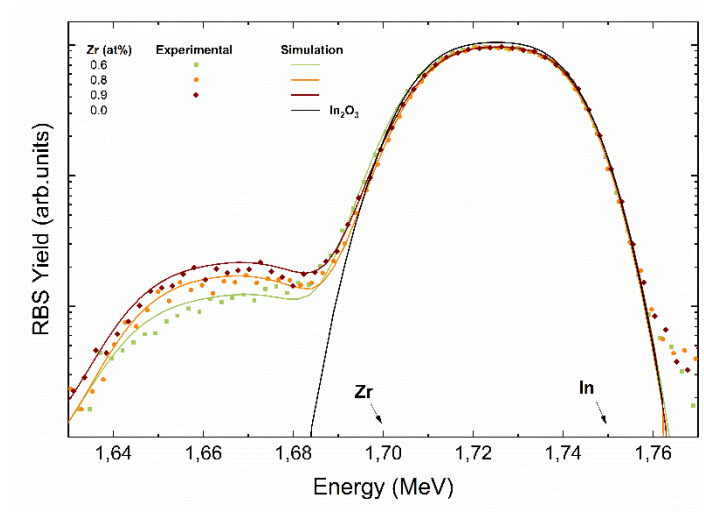


Figure 5.1: RBS experimental Spectra and Simulated curves with SimnNra software for IZrO 40 nm thin films with different Zr at% as-deposited compared with 40 nm In₂O₃ film simulated spectra.

Table 5.1: SimNra software simulation data for IZrO 40nm film thickness as-deposited for different Zr at%.

Zr (at%)	In (at%)	O (at%)
0.6	38.8	60.6
0.8	35.8	63.4
0.9	35.8	63.3

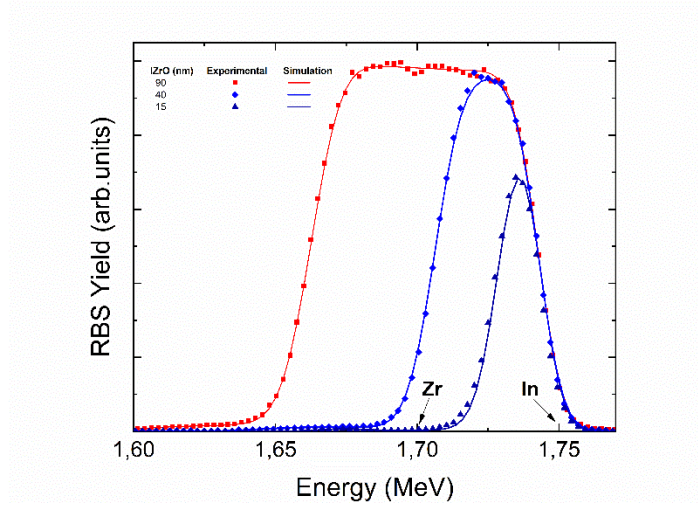


Figure 5.2: RBS experimental Spectra and Simulated curves with SimnNra software for IZrO thin films as-deposited with Zr = 0.6 at% for different thickness.

Table 5.2: RBS DATA obtained from SimNra software simulation for IZrO thin films as-deposited with Zr = 0.6 at% for different thicknesses.

Thickness (nm)	Zr (at%)	In (at%)	O (at%)
90	0.6	36.8	62.6
40	0.6	38.8	60.6
15	0.6	38.8	60.6

The semi-log scale in the chosen region allows to clearly see the small amount of Zr present inside the films. Spectra collected, represented by the dots were simulated by SimNra software as showed by the solid lines, for quantitative analysis. In the graph the energy positions for He ions backscattered by Zr and In at the surface are also indicated. For this first set of samples, the deposition time was fixed to obtain the same thickness, about 40 nm using the atomic areal density (atoms/cm²) simulated with the software and the atomic density ($d_{\text{IZrO}} = 7.69 \times 10^{22}$ at/cm³). The RBS yield proportional to the element atomic concentration allowed us to detect the Zr at% going from 0.6 at% to 0.9 at%. For comparison, an In₂O₃ film (with Zr = 0 at%) of the same thickness has been simulated.

In Figure 5.2, the second set of samples, with a fixed Zr concentration of 0.6 Zr at%, is also showed in the Zr and In regions. The signal width proportional to the film thickness confirmed the three different thickness of 90, 40 and 15 nm.

Data obtained by RBS simulations for both set of samples have listed in Table 5.1 and Table 5.2. The same graphs in the entire range are shown in Figure A.1 and Figure A.2 in Appendix A, on a linear scale.

5.3.2. XRD Measurements

Figure 5.3 shows the X-Ray Diffraction patterns of the as-deposited and annealed ($T=200\text{ }^{\circ}\text{C}$) samples for different thickness. Films show the characteristic diffraction peaks along (211), (222), (400), (440), and (622) planes of the unit cubic bixbyte structure of $\text{In}_2\text{O}_3^{24}$.

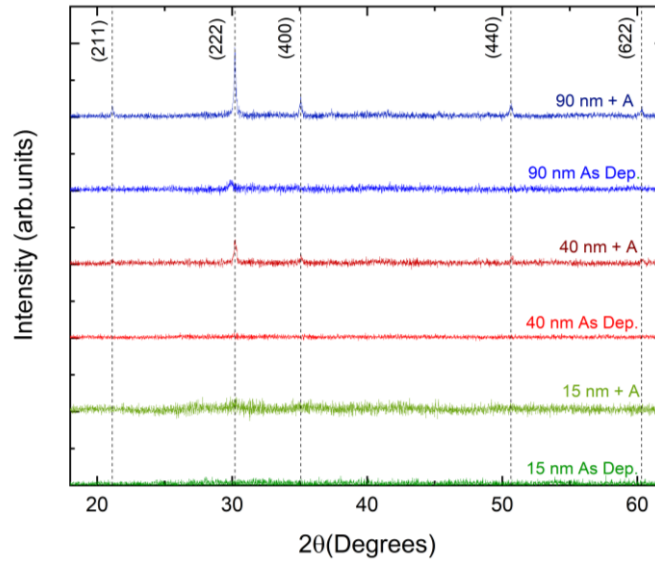


Figure 5.3: XRD Pattern for as-deposited and annealed IZrO films for different thickness.

Table 5.3: (hkl) miller index, 2θ position of the peaks, and relative intensity for IZrO crystalline thin films.

Sample Name	hkl	2θ (Degrees)	Relative Intensity (%)
IZrO 90nm As Dep.	222	29.90	100
IZrO 90nm + A	211	21.12	16.24
-	222	30.20	100
-	400	35.06	28.98
-	440	50.64	17.87
-	622	60.32	15.17
IZrO 40 nm + A	222	30.23	100
-	400	35.12	39.36
-	440	50.70	38.68

Most of the as-deposited films exhibit amorphous nature except for the 90 nm one, confirming that if the thickness is large enough it is possible to grow crystalline films by sputtering at RT as reported for other TCO¹²³. For the annealed samples, they showed a transition to the crystalline phase, together with an increase in the intensity and in the number of characteristic peaks observed, alongside thickness, as the intensity is proportional to the effective volume of the crystalline material on the sample.

The 15 nm IZrO films do not show any characteristic peaks even after the annealing, probably due to their ultra-thin nature. The 2θ positions of the detected peaks, assigned crystallographic planes, and relative intensities are listed in Table 5.3. Some peaks, compared to the reference are slightly shifted towards higher angles and this can be attributed to the presence of Zr interstitial atoms in the lattice. All the spectra showed no diffraction peaks for impurity phases, as expected, due to the similar atomic radii of In (80 pm) and Zr (72 pm). The relative intensities of the peaks confirm for all the samples the preferred orientation towards the (222) plane according to the In₂O₃ bixbyte structure.

Additional sample information can be obtained from further analysis of the peak width. The Full-Width Half Maximum is related to the average size D of the single crystalline domain within the polycrystalline films through the Scherrer Formula (equation 5.1):

$$D = \frac{K\lambda}{W\cos\theta} \quad (5.1)$$

in which $K=0.9$ is the Scherrer constant, λ is the XRD wavelength, $\theta = 2\theta/2$ is the peak position and W is the FWHM of the peak. XRD patterns for the (222) region peak of crystalline samples (IZrO 90 nm as-deposited, 40 nm +A, 90 nm + A) have been collected at high resolution and subsequently fitted with

Gaussian function to extrapolate the FWHM of the peaks. The FWHM has been corrected considering the instrumental broadening, which was previously estimated from a Corundum sample used as a reference. We calculated an average crystal size D for IZrO films as 20.52 nm for IZrO 90nm as-deposited films and 30.53 nm and 42.04 nm for annealed films IZrO 40nm and 90nm respectively. A reduction of the FWHM and the corresponding increase of D is related to an improvement of the crystalline quality of the film as confirmed by the XRD spectra. The related Figures with Gaussian peaks fit are reported in Appendix A (Figure A.3, Figure A.4, Figure A.5, and Table A.1)

5.3.3. AFM Measurements

The surface morphology of IZrO films for different thicknesses was investigated by atomic force microscopy measurements (AFM) as shown in Figure 5.4. All the thin films have a smooth surface morphology as shown by the low surface roughness (1-2 nm range) listed in Table 5.4 in terms of Root Mean Square Roughness (RMS). For the as-deposited samples increasing the thickness lead to bigger native grains that aggregates into cluster after annealing. The native grains aggregation also became more evident with increasing the thickness.

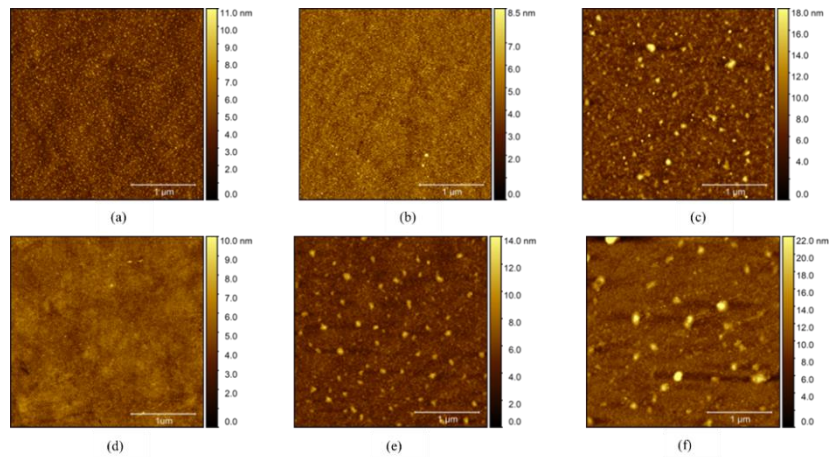


Figure 5.4: AFM images (3μm x 3μm) of IZrO thin films for different thickness as deposited: (a) 15nm as-deposited, (b) 40nm as-deposited, (c) 90nm as-deposited, and after annealing: (d) 15 nm + A, (e) 40 nm + A, (f) 90 nm + A.

5.3 Results and discussions

Table 5.4: Root Mean Square Roughness (RMS) for different IZrO films thickness before (as-dep.) and after (+A) annealing.

IZrO thickness (nm)	RMS As Dep. (nm)	RMS + A (nm)
15	1.17	0.85
40	0.88	1.21
90	1.76	2.11

5.3.4. FM-KPFM Measurements

The Work Function of IZrO thin films as a function of the doping concentration has been extracted through surface potential mapping in Frequency Modulated – Kelvin Probe Force Microscopy (FM-KPFM) mode. The morphology and the complementary surface potential map of 3x3 um scan-size for the three different Zr at% (0.6 at%, 0.8 at%, and 0.9 at%) after annealing are shown in Figure 5.5 and compared with In₂O₃ (Zr = 0 at%) to check the effect of Zr introduction in the lattice. A heavily doped Silicon probe (PFQNE-AL) has been used and previously calibrated against the work function of the Au : ($\Phi_{Tip} = \Phi_{Au} - eV_{CDP}$) where we assumed $\Phi_{Au} = 5.01$ eV and V_{CDP} was measured on an Au sample reference. For every map, the average value of the surface potential has been extracted by further analysis, and the work function is calculated according to the relevant equation for the Tip biasing mode:

$$\Phi_{Sample} = \Phi_{Tip} + eV_{CDP} \quad (5.2)$$

All the values obtained are listed in Table 5.5. A clear effect of the Zr introduction is the increase of the Work Function from 4.51 eV up to 4.65 eV. The maps evidence also, a uniform work function in a 3x3 um scan size area.

Table 5.5: Work Function values and Root Mean Square Roughness (RMS) for IZrO 40nm thin films with different Zr at% compared with 40 nm In₂O₃ thin film (Zr = 0 at%).

Zr (at%)	W _F (eV)	RMS (eV)
0	4.51	0.02
0.6	4.57	0.02
0.8	4.55	0.02
0.9	4.65	0.02

5. Zr-doped Indium Oxide thin films as transparent electrodes for photovoltaic applications

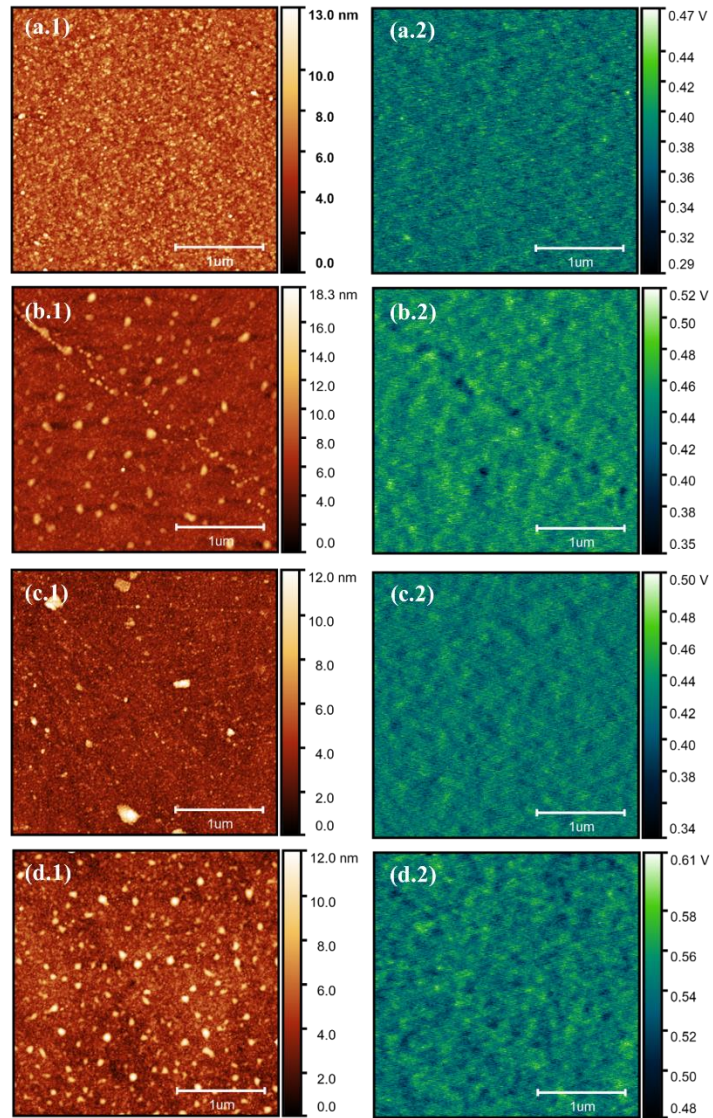


Figure 5.5: Surface morphology and surface potential maps from FM-KPFM measurements for IZrO films with different Zr at%: 0 at% (a.1-a.2), 0.6 at% (b.1- b.2), 0.8 at% (c.1-c.2), 0.9 at% (d.1- d.2).

5.3.5. Electrical properties

The electrical characterization has been performed with a four-point probe in a Van Der Pauw configuration, with a Hall system, to measure the Sheet Resistance R_{sh} , the carrier mobility μ_e and carrier concentration n_e . From the R_{sh} and film thickness, the resistivity ρ has been calculated. All values are reported in Table A.2 and Table A.3 in Appendix A. For both sets of samples, a clear effect of the annealing is the improvement of the electrical properties with a decrease in the resistivity, higher values of carrier mobility, and a decrease in the carrier concentration. Figure 5.6 shows the electrical resistivity for the different Zr at% for film thickness fixed at 40nm before and after the post-deposition thermal annealing compared with standard ITO samples from the literature. The trend shows a decrease in the electrical resistivity after annealing from $10^{-3} \Omega cm$ down to $4 \cdot 10^{-4} \Omega cm$ with lower values compared to ITO⁷⁰ ($7 \cdot 10^{-4} \Omega cm$). Carrier concentration n_e and carrier mobility μ_e are compared in Figure 5.7 for different Zr at%, after annealing, to establish which concentration produces the best electrical properties. Data evidence that for the lowest (Zr = 0.6 at%) the materials have the best electrical properties with the highest carrier mobility up to $21 \text{ cm}^2 V^{-1} s^{-1}$ and the lowest carrier concentration $-1.10 \cdot 10^{21} \text{ cm}^{-3}$. The increase of the dopant concentration is accompanied by a decrease of the carrier mobility.

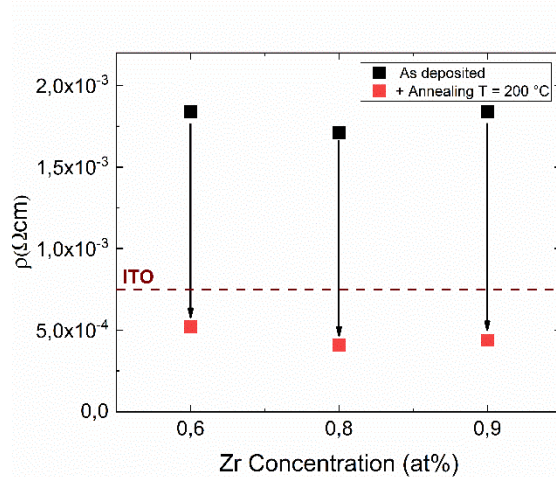


Figure 5.6: IZrO thin films resistivity for different Zr at% of 0.6 at%, 0.8 at% and 0.9 at% with a fixed thickness of 40nm, before and after post-deposition thermal annealing compared with ITO reference from literature⁷⁰.

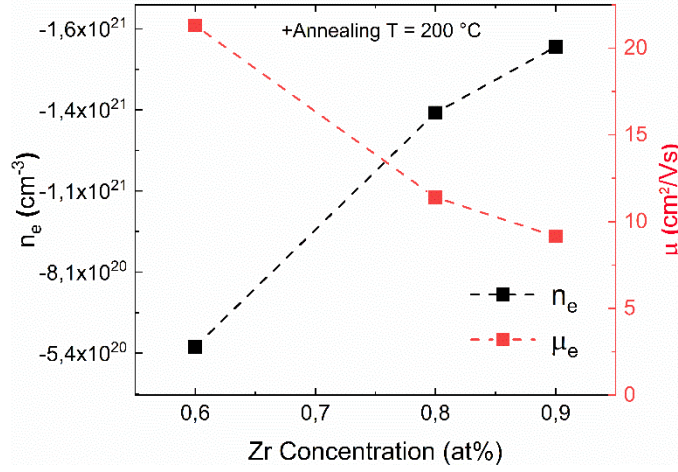


Figure 5.7: IZrO thin films mobility and carrier concentration for different Zr at% of 0.6at%, 0.8at% and 0.9at% with a fixed thickness of 40nm, before and after post-deposition thermal annealing.

Keeping the dopant concentration at $Zr = 0.6 \text{ at\%}$, the electrical properties of thin films with reduced thickness has been analyzed. To compare the electrical performance for different materials with the same thickness we listed the Sheet Resistance of ultra-thin TCO films in Table 5.6: ITO 20nm, AZO 20nm¹²⁴ from the literature, compared to our IZrO 15nm.. Our data show prominent results as $R_{sh} = 344 \Omega/\square$ for IZrO compared to the higher $623 \Omega/\square$ and $876 \Omega/\square$ for ITO and AZO respectively.

In addition, to evaluate the activation rate for the Zr donors, the ratio between the measured carrier density (from Van der Pauw measurements) and the expected carrier density (from RBS analysis) has been calculated (equation 5.4) assuming that every Zr atom in a substitutional Indium site can contribute with one electron in the conduction band (equation 5.3).



Table 5.6: Comparison of Sheet Resistance for IZrO 15nm film thickness with different types of ultra-thin TCO films, ITO 20nm, and AZO 20nm.

Sample Name and thickness (nm)	R_{sh} (Ω/\square)
IZrO 15nm [this work]	344
ITO 20nm ¹¹⁸	623
AZO 20nm ¹¹⁸	876

$$R = \frac{\text{Measured Carrier Density } (n_{VD})}{\text{Expected Carrier Density } (n_{RBS})} \quad (5.4)$$

Carrier Concentration values are listed in Table A.4 and Table A.5 in Appendix A. In Figure 5.8 and Figure 5.9 the activation Rate (R) for a sample with a fixed thickness (40 nm) and with fixed Zr at% (0.6 at%) respectively, have been compared before and after post-deposition thermal annealing. The general trend shows an activation rate values higher than 1, indicating that Zr behaves as a good donor impurity already in the as-deposited samples and that most carriers are generated from donor-type lattice defects in In_2O_3 as oxygen vacancies. For many samples, R decreases after the annealing as a possible consequence of oxygen absorbed during the annealing in air atmosphere, so partially annealing oxygen vacancies. However, the high carrier density for all samples confirms that Zr acts as an efficient dopant already at room temperature deposition.

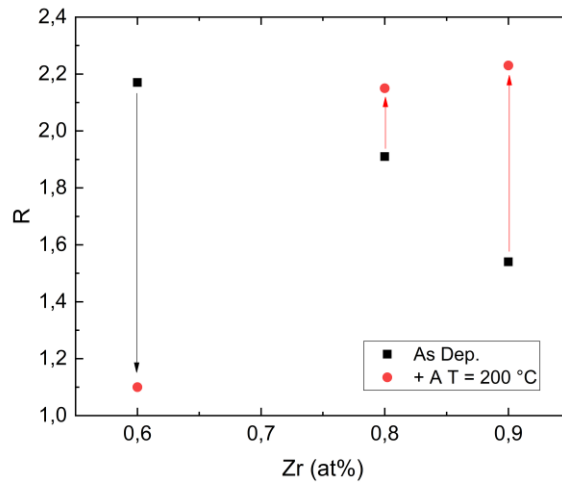


Figure 5.8: Activation Rate for different Zr at% of 0.6 at%, 0.8 at% and 0.9 at% with a fixed thickness of 40 nm, before and after post-deposition thermal annealing.

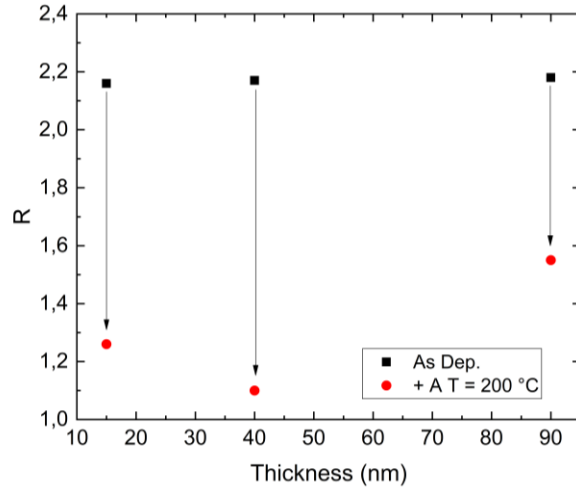


Figure 5.9: Activation Rate for different IZrO thickness of 15 nm, 40 nm, and 90 nm with a fixed Zr = 0.6 at%, before and after post-deposition thermal annealing.

5.3.6. Optical properties

Figure 5.11 and Figure 5.10 show the transmittance spectra for samples with different Zr at% (fixed thickness) and with different thicknesses (fixed Zr at%) respectively before and after the thermal treatments. The effect of post-deposition thermal annealing is the improvement of the optical properties for all sets of samples, increasing the mean values of the transmittance ($\langle T \rangle$) both in VIS and in the NIR range. This can be related to an improvement of the crystalline quality of the films according to XRD measurements shown in Section 5.3.2. From Figure 5.10, where the transmittance is shown as a function of the doping concentration, a decrease in the transmittance is evident as the donor concentration increases. The lowest concentration of, $Zr = 0.6 \text{ at\%}$, shows the best optical performances with high values of transmittance up to $\langle T \rangle = 72\%$ in the VIS range and $\langle T \rangle = 84\%$ in NIR range after annealing. Once fixed $Zr = 0.6 \text{ at\%}$, Figure 5.11 shows the transmittance spectra for different thicknesses (90 nm, 40 nm, and 15 nm) and, as expected, a decreasing of the thickness produces an increase of the transmittance in all wavelength ranges, up to 86% in VIS after annealing. In the NIR range, the low carrier density after annealing ($\approx -5 \cdot 10^{20} \text{ cm}^{-3}$) leads to a decrease of the plasma frequency, with a consequent increase of the transmittance in this range, up to 92% for the 15 nm thick IZrO. The reflectance spectra for both set of samples are reported in Figure A.6 and Figure A.7 in Appendix A.

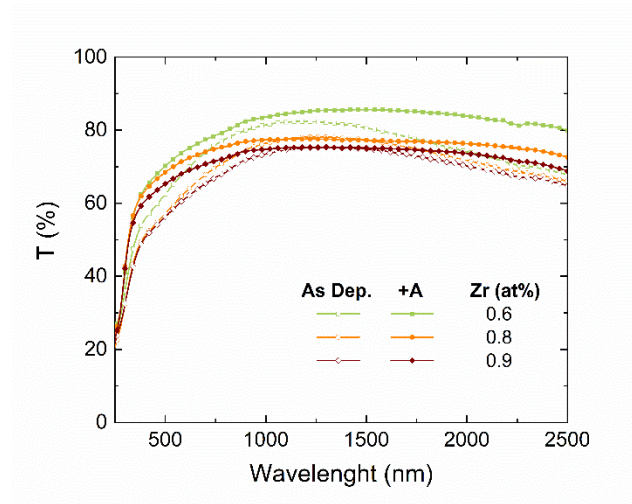


Figure 5.11: Transmittance spectra of IZrO thin films for different thickness of 90 nm, 40 nm, and 15 nm with a fixed Zr = 0.6 at%, before and after post-deposition thermal annealing.

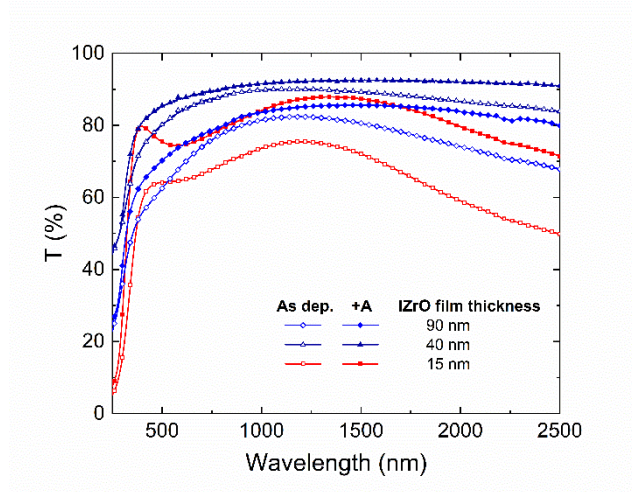


Figure 5.10: Transmittance spectra of IZrO thin films for different Zr at% of 0.6 at%, 0.8 at% and 0.9 at% with a fixed thickness of 40nm, before and after post-deposition thermal annealing.

The optical band gap was calculated using Tauc's equation⁵⁵ for direct transitions (equation 5.5):

5. Zr-doped Indium Oxide thin films as transparent electrodes for photovoltaic applications

Table 5.7: Mean Values for Transmittance in the VIS range ($\langle T \rangle_{\text{vis}}$), NIR range ($\langle T \rangle_{\text{NIR}}$), and Energy gap values (E_g) for different Zr at% of 0.6at%, 0.8 at% and 0.9 at% with a fixed thickness of 40nm, before and after post-deposition thermal annealing.

Sample Name	$\langle T \rangle_{\text{vis}}$ (380-780) (%)	$\langle T \rangle_{\text{NIR}}$ (780-1500) (%)	E_g (eV)
Zr = 0.6 at% As Dep.	60.2	81.15	3.95
Zr = 0.6 at% + A	72.3	84.06	4.04
Zr = 0.8 at% As Dep.	60.62	76.59	3.86
Zr = 0.8 at% + A	70.06	77.2	3.92
Zr = 0.9 at% As Dep.	59.17	73.76	3.85
Zr = 0.9 at% + A	66.86	74.78	4.12

Table 5.8: Mean Values for Transmittance in the VIS range ($\langle T \rangle_{\text{vis}}$), NIR range ($\langle T \rangle_{\text{NIR}}$), and Energy gap values (E_g) for d for different IZrO film thicknesses of 90nm, 40nm, and 15nm with a fixed Zr = 0.6 at%, before and after post-deposition thermal annealing.

Sample Name	$\langle T \rangle_{\text{vis}}$ (380-780) (%)	$\langle T \rangle_{\text{NIR}}$ (780-1500) (%)	E_g (eV)
90 nm As Dep.	64.27	73.49	3.89
90 nm + A	76.18	85.3	4.07
40 nm As Dep.	66.26	81.15	3.92
40 nm + A	72.35	84.08	4.05
15 nm As Dep.	82.27	89.60	3.77
15 nm + A	86.11	91.78	3.91

$$(E\alpha)^2 = B(E - E_{gap}) \quad (5.5)$$

where B is the Tauc coefficient, α the absorption coefficient, and E the photon energy. In this way, E_{gap} is obtained at the x axis intercept of the curve fitted on the linear portion of the Tauc plots shown in Figure 5.12 and Figure 5.13 for different Zr at% and different thicknesses, respectively. For the samples, α has been extracted by using the following equation (equation 5.6) ¹¹⁰.

$$\alpha = \frac{1}{d} \ln \frac{T_G(1 - R_s)}{T_s} \quad (5.6)$$

where d , T_s , and R_s are the thickness, transmittance and reflectance of the sample respectively, while T_G is the transmittance of the glass substrate. The band-gap values are in the range of 3.91 eV before annealing with a slight increase up to 4.12 eV after the thermal treatment confirming the nature of wide band gap TCO for IZrO. The energy gap values and mean values of transmittance are listed in Table 5.7 and Table 5.8.

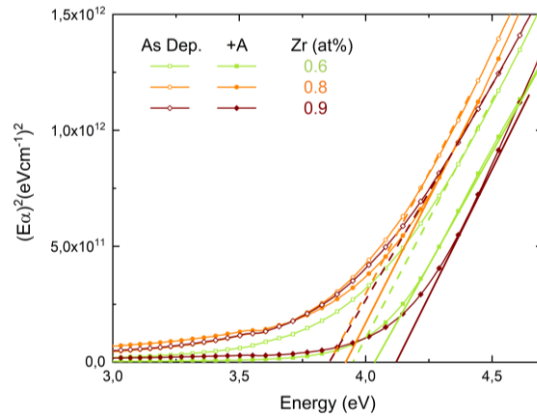


Figure 5.12: Tauc Plot of IZrO thin films for different Zr at% of 0.6 at%, 0.8 at% and 0.9 at% with a fixed thickness of 40 nm, before and after post-deposition thermal annealing.

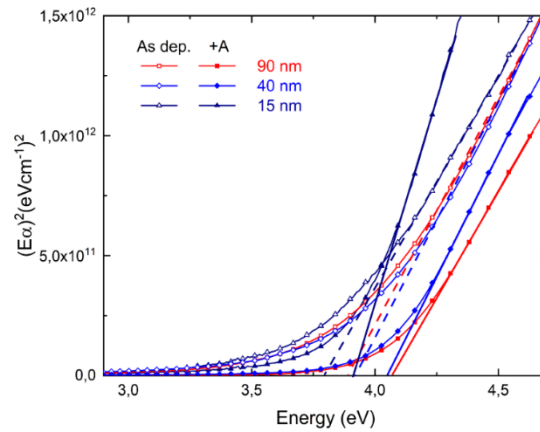


Figure 5.13: Tauc Plot of IZrO thin films for different thickness of 15 nm, 40 nm, and 90 nm with a fixed Zr = 0.6 at%, before and after post-deposition thermal annealing.

5.3.7. Device Characterization

We tested the performance of the IZrO electrodes on a bifacial Silicon Heterojunction solar cell. The cell was fabricated by Enel 3SUN company with the structure of a-Si(p⁺):H/a-Si(i):H/c-Si(n)/a-Si(i):H/a-Si(n⁺):H, while 90nm IZrO thin films have been deposited as front and back contact as illustrated in the schematic of Figure 5.14c. An equivalent cell with ITO deposited by 3SUN has been tested as reference. The cells have been subsequently annealed at T = 200 °C in an ambient atmosphere. Figure 5.14(a-b) shows SEM images top view at different magnifications after the deposition of IZrO.

In Figure 5.15 the EQE measurements for both cells with IZrO electrodes (orange lines) and ITO electrodes (violet lines) after the thermal process are reported. The EQE has been measured either by shading light from the front and from the back. It is evident as the cell with ITO electrodes deposited during the industrial fabrication process shows an excellent performance in all ranges for both configurations, i.e. front and back side illumination. On the other hand, EQE of the cell with IZrO electrodes deposited on small pieces in our laboratory, so

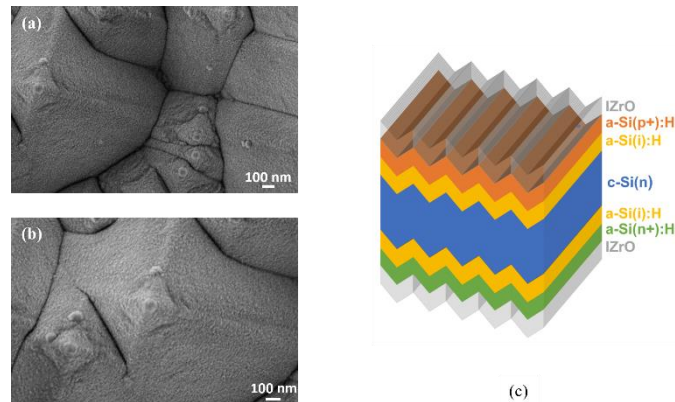


Figure 5.14: Top view SEM images of 90 nm IZrO deposited on top of rear bifacial SHJ solar cell at different magnification (a),(b), and Bifacial rear-junction Silicon Heterojunction solar cell (a structure supplied by Enel 3sun in the aim of the BEST4U project with IZrO electrodes deposited as aim of this work.

interrupting the fabrication process, is lower with respect to the industrial reference. The EQE reduction is dramatic for the back side illumination, probably due to parasitic losses, while the EQE for the front side is almost equivalent to the industrial cell, with an evident reduction only in the infrared region. In all cases, the EQE responses for IZrO contacts deposited at the University (i.e. far from the

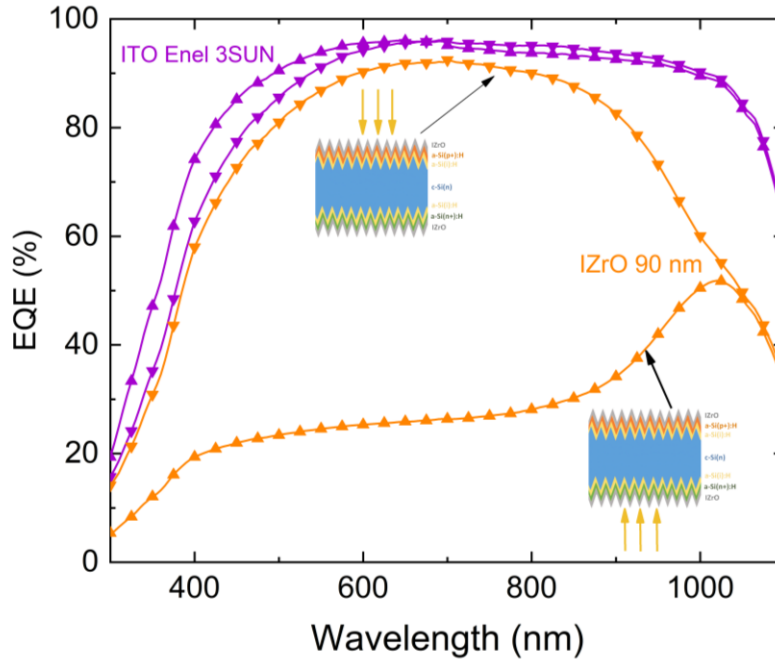


Figure 5.15: EQE data on the SHJ solar cell with 90nm IZrO thickness after annealing deposited as front and back contacts compared with EQE on SHJ solar cell with ITO deposited by Enel 3SUN as front and back contact after annealing.

optimal industrial conditions) are much higher with respect to those obtained with ITO deposited using the same equipment.

5.4. Conclusions

In summary, we grew Zr-doped Indium Oxide thin films by co-sputtering deposition at room temperature followed by post-deposition thermal annealing at $T = 200\text{ }^{\circ}\text{C}$. A preliminary study has been performed to determine the best Zr at% for the opto-electrical properties. Measurements show that with Zr = 0.6 at%, carrier mobility up to $21\text{ cm}^2\text{V}^{-1}\text{s}^{-1}$ and optical transparency up to $T = 86\%$ in the VIS range and $T = 92\%$ in the NIR range can be achieved after annealing due to an improvement of the crystalline quality of the films as confirmed by XRD measurements. In addition, the material satisfies all the requirements for an excellent TE like uniform work function ($W_F \approx 4.6\text{ eV}$), wide bandgap ($E_g \approx 4$

5. Zr-doped Indium Oxide thin films as transparent electrodes for photovoltaic applications

eV), and low surface-roughness ($1\text{nm} < \text{RMS}_q < 2\text{ nm}$). With the strategy of growing In-based-TCO with very low thickness to reduce the amount of Indium, without affecting the performances of the electrode, we set up a study as a function of the IZrO thickness. Three different samples have been grown with thickness of 90 nm, 40 nm, and 15 nm, and they have been characterized through different techniques. The thinnest film, only 15 nm, has been compared to other ultra-thin TCO films (ITO-20nm and AZO-20nm) showing the lowest Sheet Resistance ($R_{\text{sh}} = 344\ \Omega/\square$). We successfully implemented IZrO electrodes on a bi-facial Silicon Heterojunction solar cell and EQE measurements evidenced performances comparable to those of standard ITO electrodes deposited during a real industrial process, confirming IZrO as a promising alternative material to ITO.

Conclusions

This thesis describes the developing of In-based TCO for high-efficiency transparent electrode applications in SHJ solar cells. The main conclusions are summarized below.

First, we developed Mo co-doped ITO with DC and RF Magnetron sputtering thin films. In Chapter 4 we described Mo:ITO deposited at room temperature and further annealed at different temperatures from 200 °C up to 500 °C. The measurements evidenced a drastic improvement of both electrical and optical properties of ITMO thin films with post-deposition annealing at $T \geq 300$ °C. The average values of the transmittance calculated in the range 380-750 nm shows an increase from 30% up to 77% for high post-deposition thermal processes. ITMO benefits of thermal annealing processes, showing in all cases a reduction of the resistivity and an increase of the carrier mobility. Moreover, in full agreement with the results of other characterizations, a strong improvement at 300 °C is observed for ρ , its value decreasing by a factor of 30 with respect to the as-deposited film and by a factor of 10 with respect to that annealed at 200 °C. Our experimental work has shown that, already at room temperature, the free electron concentration in ITMO is quite high, an evidence that Mo can act as an efficient dopant already at room temperature. The limited electrical properties of ITMO films can be attributed to the presence of defects that are partially removed during a thermal process.

The second step of the research activity focused on the growth and characterization of Zr-doped In_2O_3 thin films. A preliminary study has been conducted with different Zr at% to evaluate the best donor concentration for the highest mobility and optical transmittance. Then, fixing the Zr at% the opto-electrical properties have been studied as a function of the thickness, from the standard values of 90 nm used in solar cells down to 15 nm. Ultra-thin films were deposited at room temperature followed by post-deposition thermal treatment at $T = 200$ °C, to make the process compatible with Silicon solar cells and possible application in flexible devices. The effect of post-deposition thermal annealing is

the improvement of the optical properties for all samples, increasing the mean values of the transmittance ($\langle T \rangle$) both in VIS and in NIR range. The lowest concentration $Zr = 0.6 \text{ at\%}$ shows the best optical performances, with high values of transmittance up to $\langle T \rangle = 72\%$ in the VIS range and $\langle T \rangle = 84\%$ in NIR range after annealing. For both sets of samples, a clear effect of the annealing is the improvement of the electrical properties with a decrease of the resistivity, higher values of the carrier mobility, and a decrease of the carrier concentration. We successfully grew IZrO thin films of 90 nm on a bi-facial Silicon Heterojunction solar cell and EQE measurements evidenced performances comparable to those of standard ITO electrodes deposited by Enel 3Sun Company, confirming IZrO as a promising alternative material to ITO.

A. Appendix

A.1 RBS Supplementary Informations

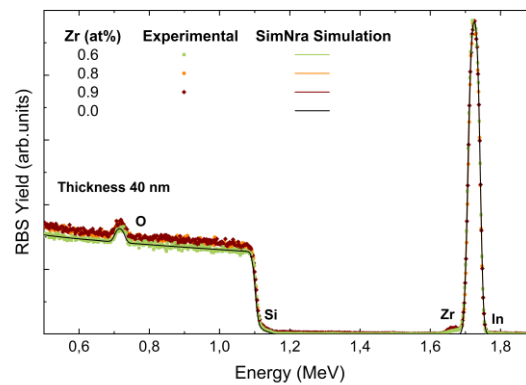


Figure A. 2: RBS extended experimental Spectra and Simulated curves with SimNra software for IZrO 40 nm thin films on Silicon substrate as-deposited with different Zr at% compared with 40nm In₂O₃ films simulated spectra.

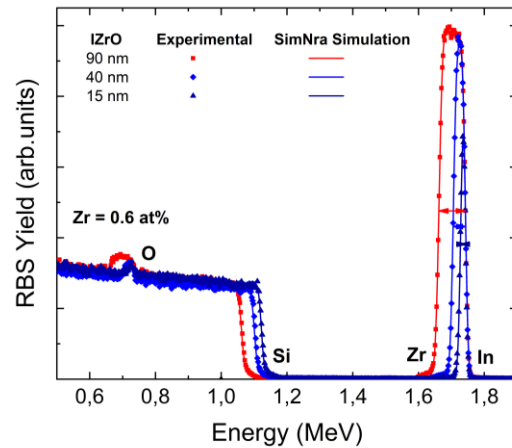


Figure A. 1: RBS extended experimental Spectra and Simulated curves with SimNra software for IZrO thin films on Silicon substrate as-deposited with Zr = 0.6 at% for different thickness.

A.2 XRD Supplementary Informations

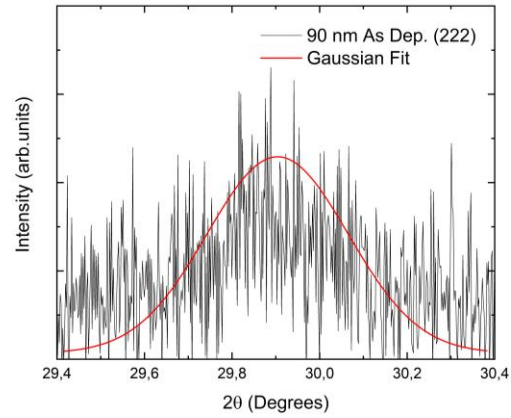


Figure A. 3: XRD pattern and Gaussian peak fit for the (222) plane of IZrO 90nm as-deposited thin film.

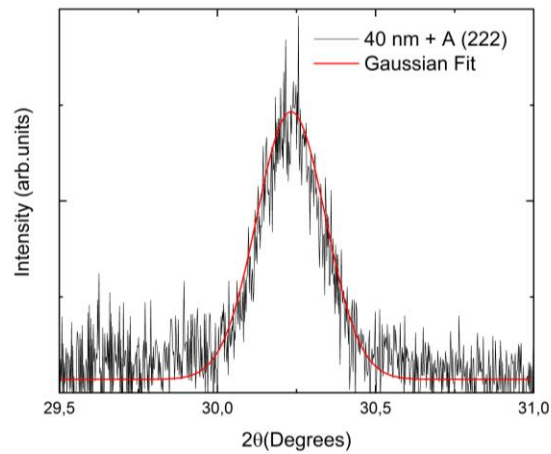


Figure A. 4: XRD pattern and Gaussian peak fit for the (222) plane of IZrO 40nm thin film after annealing.

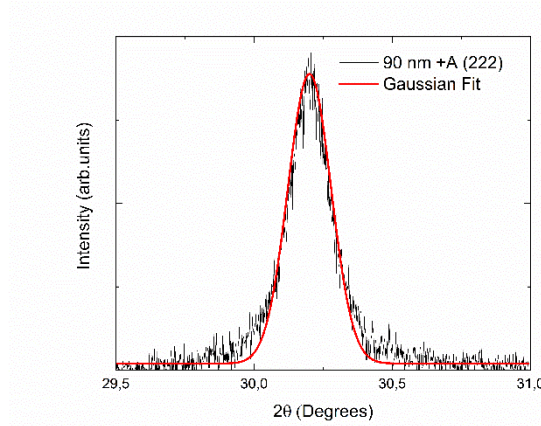


Figure A. 5: XRD pattern and Gaussian peak fit for the (222) plane of IZrO 90 nm thin film after annealing.

Table A.1: Average Crystal size (τ) obtained from Scherrer formula for different crystalline samples

Sample Name	τ (nm)
IZrO 90 nm As Dep.	20.52
IZrO 40 nm + A	30.53
IZrO 90 nm + A	42.04

A.3 Electrical properties Supplementary Informations

Table A.2: Sheet Resistance (R_{Sh}), Resistivity (ρ) Carrier Mobility (μ_e) and Carrier Concentration (n_e) for different Zr at% of 0.6 at%, 0.8 at% and 0.9 at% with a fixed thickness of 40nm, before and after post-deposition thermal annealing

Sample Name	R_{Sh} (Ω/\square)	ρ (Ωcm)	μ_e ($cm^2 V^{-1} s^{-1}$)	n_e (cm^{-3})
Zr = 0.6 at% As Dep.	460.5	$1.84 \cdot 10^{-3}$	3.06	$-1.10 \cdot 10^{21}$
Zr = 0.6 at% + A	130.9	$5.20 \cdot 10^{-4}$	21.3	$-5.61 \cdot 10^{20}$
Zr = 0.8 at% As Dep.	445.2	$1.71 \cdot 10^{-3}$	3.07	$-1.19 \cdot 10^{21}$
Zr = 0.8 at% + A	106.4	$4.10 \cdot 10^{-4}$	11.4	$-1.34 \cdot 10^{21}$
Zr = 0.9 at% As Dep.	468.3	$1.84 \cdot 10^{-3}$	3.15	$-1.08 \cdot 10^{21}$
Zr = 0.9 at% + A	111.6	$4.38 \cdot 10^{-4}$	9.15	$-1.56 \cdot 10^{21}$

Table A.3: Sheet Resistance (R_{Sh}), Resistivity (ρ), Carrier Mobility (μ_e) and Carrier Concentration (n_e) for different IZrO film thickness of 90 nm, 40 nm and 15 nm with a fixed Zr = 0.6 at%, before and after post-deposition thermal annealing.

IZrO thickness	R_{Sh} (Ω/\square)	ρ (Ωcm)	μ_e ($cm^2 V^{-1} s^{-1}$)	n_e (cm^{-3})
90 nm As Dep.	184.6	$1.64 \cdot 10^{-3}$	3.84	$-9.89 \cdot 10^{20}$
90 nm + A	64.86	$5.79 \cdot 10^{-4}$	15.3	$-7.02 \cdot 10^{20}$
40 nm As Dep.	463.5	$1.84 \cdot 10^{-3}$	3.06	$-1.10 \cdot 10^{21}$
40 nm + A	130.9	$5.20 \cdot 10^{-4}$	21.3	$-5.61 \cdot 10^{20}$
15 nm As Dep.	1098	$1.54 \cdot 10^{-3}$	3.82	$-1.07 \cdot 10^{21}$
15 nm + A	343.9	$4.81 \cdot 10^{-4}$	20.8	$-6.22 \cdot 10^{20}$

Table A.4 Carrier Concentration from Van Der Pauw Measurements (n_{VD}) and from RBS Measurements (n_{RBS}) for different Zr at% of 0.6 at%, 0.8 at% and 0.9 at% with a fixed thickness of 40 nm, before and after post-deposition thermal annealing

Zr (at%)	n_{VD} (cm^{-3})	n_{RBS} (cm^{-3})
Zr = 0.6 at% As Dep.	$-1.06 \cdot 10^{21}$	$-4.88 \cdot 10^{20}$
Zr = 0.6 at% + A	$-5.38 \cdot 10^{21}$	$-4.88 \cdot 10^{20}$
Zr = 0.8 at% As Dep.	$-1.19 \cdot 10^{21}$	$-6.23 \cdot 10^{20}$
Zr = 0.8 at% + A	$-1.34 \cdot 10^{21}$	$-6.23 \cdot 10^{20}$
Zr = 0.9 at% As Dep.	$-1.08 \cdot 10^{21}$	$-7.01 \cdot 10^{20}$
Zr = 0.9 at% + A	$-1.56 \cdot 10^{21}$	$-7.01 \cdot 10^{20}$

Table A.5. Carrier Concentration from Van Der Pauw Measurements (n_{VD}) and from RBS Measurements (n_{RBS}) for different IZrO film thickness of 90nm, 40nm and 15nm with a fixed Zr = 0.6 at%, before and after post-deposition thermal annealing.

IZrO thickness (nm)	n_{VD} (cm^{-3})	n_{RBS} (cm^{-3})
90 nm As Dep.	$-1.02 \cdot 10^{21}$	$-4.69 \cdot 10^{20}$
90 nm + A	$-7.25 \cdot 10^{20}$	$-4.69 \cdot 10^{20}$
40 nm As Dep.	$-1.06 \cdot 10^{21}$	$-4.88 \cdot 10^{20}$
40 nm + A	$-5.38 \cdot 10^{20}$	$-4.88 \cdot 10^{20}$
15 nm As Dep.	$-1.01 \cdot 10^{21}$	$-4.67 \cdot 10^{20}$
15 nm + A	$-5.89 \cdot 10^{20}$	$-4.67 \cdot 10^{20}$

A.4 Optical properties Supplementary Informations

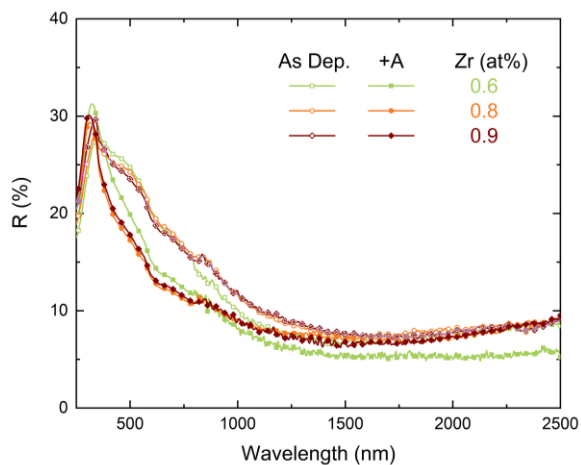


Figure A. 6: Reflectance spectra of IZrO thin films for different Zr at% of 0.6 at%, 0.8 at% and 0.9 at% with a fixed thickness of 40 nm, before and after post-deposition thermal annealing.

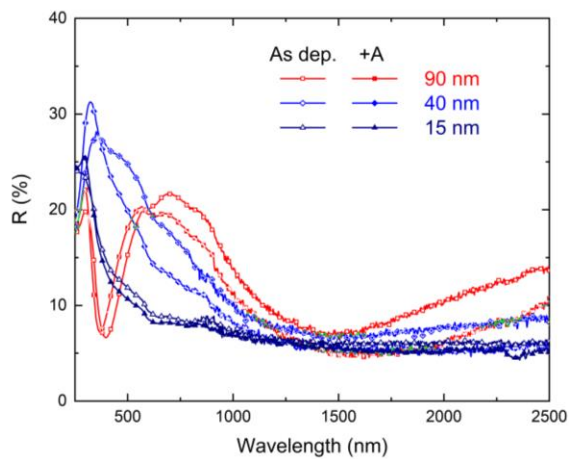


Figure A. 7: Reflectance spectra of IZrO thin films for different thickness of 90 nm, 40 nm, and 15 nm with a fixed Zr = 0.6at%, before and after post-deposition thermal annealing.

References

1. Lenssen, N. J. L. *et al.* Improvements in the GISTEMP Uncertainty Model. *J. Geophys. Res. Atmos.* **124**, 6307–6326 (2019).
2. Data.GISS: GISS Surface Temperature Analysis: Sources. <https://data.giss.nasa.gov/gistemp/>.
3. IEA. World Energy Outlook 2021 : Part of the World Energy Outlook. *Int. Energy Agency* 386 (2021).
4. International Energy Agency. Net Zero by 2050: A Roadmap for the Global Energy Sector. *Int. Energy Agency* 224 (2021).
5. United Nations Development Programme. *World Energy Assessment. Energy and the challenge of Sustainability. World Energy Assessment* (2000).
6. Becquerel, E. Mémoire sur les effets électriques produits sous l'influence des rayons solaires. *Comptes Rendus* **9**, 561–567 (1839).
7. Fritts, C. E. On the fritts selenium cells and batteries. *J. Franklin Inst.* **119**, 221–232 (1885).
8. Yan, Y. *et al.* Best Research-Cell Efficiency Chart | Photovoltaic Research | NREL. *Journal of the American Chemical Society* vol. 5 1–8 (2020).
9. Blakers, A. W., Wang, A., Milne, A. M., Zhao, J. & Green, M. A. 22.8% efficient silicon solar cell. *Appl. Phys. Lett.* **55**, 1363 (1998).
10. Zhao, J., Wang, A., Green, M. A. & Ferrazza, F. 19.8% efficient 'honeycomb' textured multicrystalline and 24.4% monocrystalline silicon solar cells. *Appl. Phys. Lett.* **73**, 1991–1993 (1998).
11. K. Baedeker, *Annalen der Physik (Leipzig)* 327 (1907) 749. - Google Scholar. https://scholar.google.com/scholar?hl=it&as_sdt=0%2C5&q=+K.+Baedeker%2C+Annalen+der+Physik+%28Leipzig%29+327+%281907%29+749.&btnG=.
12. Leenheer, A. J. *et al.* General mobility and carrier concentration relationship in transparent amorphous indium zinc oxide films. *Phys.*

- Rev. B - Condens. Matter Mater. Phys.* **77**, (2008).
13. Morales-Masis, M., Martin De Nicolas, S., Holovsky, J., De Wolf, S. & Ballif, C. Low-Temperature High-Mobility Amorphous IZO for Silicon Heterojunction Solar Cells. *IEEE J. Photovoltaics* **5**, 1340–1347 (2015).
 14. Koida, T. *et al.* Correlation between oxygen stoichiometry, structure, and opto-electrical properties in amorphous In₂O₃:H films. *J. Appl. Phys.* **111**, (2012).
 15. Kobayashi, E., Watabe, Y., ... T. Y.-S. E. M. & 2016, undefined. Cerium oxide and hydrogen co-doped indium oxide films for high-efficiency silicon heterojunction solar cells. *Elsevier*.
 16. Crupi, I. *et al.* Optimization of ZnO:Al/Ag/ZnO:Al structures for ultra-thin high-performance transparent conductive electrodes. *Thin Solid Films* **520**, 4432–4435 (2012).
 17. Torrisi, G. *et al.* Ag cluster beam deposition for TCO/Ag/TCO multilayer. *Sol. Energy Mater. Sol. Cells* **199**, 114–121 (2019).
 18. Torrisi, G., Crupi, I., Mirabella, S. & Terrasi, A. Robustness and electrical reliability of AZO/Ag/AZO thin film after bending stress. *Sol. Energy Mater. Sol. Cells* **165**, 88–93 (2017).
 19. Ebbesen, T. W., Lezec, H. J., Ghaemi, H. F., Thio, T. & Wolff, P. A. Extraordinary optical transmission through sub-wavelength hole arrays. *Nature* **391**, 667–669 (1998).
 20. Genet, C. & Ebbesen, T. W. Light in tiny holes. in *Nanoscience and Technology: A Collection of Reviews from Nature Journals* 205–212 (World Scientific Publishing Co., 2009). doi:10.1142/9789814287005_0021.
 21. Gao, H., Henzie, J. & Odom, T. W. Direct evidence for surface plasmon-mediated enhanced light transmission through metallic nanohole arrays. *Nano Lett.* **6**, 2104–2108 (2006).
 22. Valkonen, E., Karlsson, B., Energy, C. R.-S. & 1984, undefined. Solar optical properties of thin films of Cu, Ag, Au, Cr, Fe, Co, Ni and Al. *Elsevier*.
 23. Smith, G. B., Niklasson, G. A., Svensson, J. S. E. M. & Granqvist, C. G. Noble-metal-based transparent infrared reflectors: Experiments and theoretical analyses for very thin gold films. *J. Appl. Phys.* **59**, 571–581 (1986).
 24. Sahu, D. R., Chen, C. Y., Lin, S. Y. & Huang, J. L. Effect of substrate temperature and annealing treatment on the electrical and optical properties of silver-based multilayer coating electrodes. *Thin Solid Films*

- 515**, 932–935 (2006).
25. Sahu, D. R. & Huang, J. L. High quality transparent conductive ZnO/Ag/ZnO multilayer films deposited at room temperature. *Thin Solid Films* **515**, 876–879 (2006).
 26. Sahu, D. R., Lin, S. Y. & Huang, J. L. ZnO/Ag/ZnO multilayer films for the application of a very low resistance transparent electrode. *Appl. Surf. Sci.* **252**, 7509–7514 (2006).
 27. Sahu, D. R. & Huang, J. L. Characteristics of ZnO-Cu-ZnO multilayer films on copper layer properties. *Appl. Surf. Sci.* **253**, 827–832 (2006).
 28. Sahu, D. R. & Huang, J. L. Dependence of film thickness on the electrical and optical properties of ZnO-Cu-ZnO multilayers. *Appl. Surf. Sci.* **253**, 915–918 (2006).
 29. De, S. *et al.* Silver nanowire networks as flexible, transparent, conducting films: Extremely high DC to optical conductivity ratios. *ACS Nano* **3**, 1767–1774 (2009).
 30. Lee, J. Y., Connor, S. T., Cui, Y. & Peumans, P. Solution-processed metal nanowire mesh transparent electrodes. *Nano Lett.* **8**, 689–692 (2008).
 31. Garnett, E. C. *et al.* Self-limited plasmonic welding of silver nanowire junctions. *Nat. Mater.* **11**, 241–249 (2012).
 32. Zilberberg, K. & Riedl, T. Metal-nanostructures-a modern and powerful platform to create transparent electrodes for thin-film photovoltaics. *Journal of Materials Chemistry A* vol. 4 14481–14508 (2016).
 33. Barnes, T. M. *et al.* Comparing the fundamental physics and device performance of transparent, conductive nanostructured networks with conventional transparent conducting oxides. *Adv. Energy Mater.* **2**, 353–360 (2012).
 34. Zhang, F., Johansson, M., Andersson, M. R., Hummelen, J. C. & Inganäs, O. Polymer photovoltaic cells with conducting polymer anodes. *Adv. Mater.* **14**, 662–665 (2002).
 35. Ouyang, J., Chu, C. W., Chen, F. C., Xu, Q. & Yang, Y. High-conductivity poly(3,4-ethylenedioxythiophene):poly(styrene sulfonate) film and its application in polymer optoelectronic devices. *Adv. Funct. Mater.* **15**, 203–208 (2005).
 36. Stankovich, S. *et al.* Graphene-based composite materials. *Nature* **442**, 282–286 (2006).
 37. Watcharotone, S. *et al.* Graphene-silica composite thin films as

- transparent conductors. *Nano Lett.* **7**, 1888–1892 (2007).
38. Geim, A. K. Graphene: Status and prospects. *Science* vol. 324 1530–1534 (2009).
 39. Delahoy, A. E. & Guo, S. Transparent Conducting Oxides for Photovoltaics. in *Handbook of Photovoltaic Science and Engineering* 716–796 (2011). doi:10.1002/9780470974704.ch17.
 40. Ginley, David S., Hideo Hosono, and David C. Paine, E. *Handbook of Transparent Conductors. Handbook of transparent conductors* (2010).
 41. Löbmann, P. Transparent conducting oxides. in *Chemical Solution Deposition of Functional Oxide Thin Films* vol. 9783211993 655–672 (2013).
 42. Gordon, R. G. Criteria for choosing transparent conductors. *MRS Bull.* **25**, 52–57 (2000).
 43. Xu, J. *et al.* Design of n-Type Transparent Conducting Oxides: The Case of Transition Metal Doping in In₂O₃. *Adv. Electron. Mater.* **4**, 1–7 (2018).
 44. JAIN, S. C. & RADHAKRISHNA, S. Physics of Semiconductor Devices. in 1–546 (1987). doi:10.1142/9789814542012.
 45. Jain, A. *et al.* A high-throughput infrastructure for density functional theory calculations. *Comput. Mater. Sci.* **50**, 2295–2310 (2011).
 46. Ibach, H. & Lüth, H. *Solid-state physics: An introduction to principles of materials science. Solid-State Physics (Fourth Extensively Updated and Enlarged Edition): An Introduction to Principles of Materials Science* (Springer Berlin Heidelberg, 2010). doi:10.1007/978-3-540-93804-0.
 47. Lundstrom, M. Fundamentals of Carrier Transport, 2nd edn. *Meas. Sci. Technol.* **13**, 230–230 (2002).
 48. Ellmer, K. & Mientus, R. Carrier transport in polycrystalline ITO and ZnO:Al II: The influence of grain barriers and boundaries. *Thin Solid Films* **516**, 5829–5835 (2008).
 49. Erfle, H. Optische Eigenschaften und Elektronentheorie. *Ann. Phys.* **329**, 672–708 (1907).
 50. Haacke, G. New figure of merit for transparent conductors. *J. Appl. Phys.* **47**, 4086–4089 (1976).
 51. Nadaud, N., Lequeux, N., Nanot, M., Jové, J. & Roisnel, T. Structural studies of tin-doped indium oxide (ITO) and In₄Sn₃O₁₂. *J. Solid State Chem.* **135**, 140–148 (1998).

52. Marezio, M. Refinement of the crystal structure of In_2O_3 at two wavelengths. *Acta Crystallogr.* **20**, 723–728 (1966).
53. Granqvist, C. G. Transparent conductors as solar energy materials: A panoramic review. *Solar Energy Materials and Solar Cells* vol. 91 1529–1598 (2007).
54. Granqvist, C. G. & Niklasson, G. A. Solar energy materials for thermal applications: A primer. *Sol. Energy Mater. Sol. Cells* **180**, 213–226 (2018).
55. B. G. Bagley (auth.), J. T. (eds. . *Amorphous and Liquid Semiconductors*. (Springer US, 1977).
56. Ellmer, K. Resistivity of polycrystalline zinc oxide films: Current status and physical limit. *J. Phys. D. Appl. Phys.* **34**, 3097–3108 (2001).
57. Walsh, A., Da Silva, J. L. F. & Wei, S. H. Origins of band-gap renormalization in degenerately doped semiconductors. *Phys. Rev. B - Condens. Matter Mater. Phys.* **78**, 075211 (2008).
58. Smirnov, Y. *et al.* Scalable Pulsed Laser Deposition of Transparent Rear Electrode for Perovskite Solar Cells. *Adv. Mater. Technol.* **6**, 2000856 (2021).
59. Boccard, M. *et al.* Hole-Selective Front Contact Stack Enabling 24.1%-Efficient Silicon Heterojunction Solar Cells. *IEEE J. Photovoltaics* **11**, 9–15 (2021).
60. Yao, Z. *et al.* Influence of Oxygen on Sputtered Titanium-Doped Indium Oxide Thin Films and Their Application in Silicon Heterojunction Solar Cells. *Sol. RRL* **5**, 2000501 (2021).
61. Swallow, J. E. N. *et al.* Resonant doping for high mobility transparent conductors: The case of Mo-doped In_2O_3 . *Mater. Horizons* **7**, 236–243 (2020).
62. Wang, G. H., Shi, C. Y., Zhao, L., Diao, H. W. & Wang, W. J. Transparent conductive Hf-doped In_2O_3 thin films by RF sputtering technique at low temperature annealing. *Appl. Surf. Sci.* **399**, 716–720 (2017).
63. Han, C. *et al.* Room-temperature sputtered tungsten-doped indium oxide for improved current in silicon heterojunction solar cells. *Sol. Energy Mater. Sol. Cells* **227**, (2021).
64. Yu, J. *et al.* Improved opto-electronic properties of silicon heterojunction solar cells with $\text{SiO}_x/\text{Tungsten-doped indium oxide}$ double anti-reflective coatings. *Jpn. J. Appl. Phys.* **56**, 08MB09 (2017).

65. Yu, J. *et al.* Tungsten doped indium oxide film: Ready for bifacial copper metallization of silicon heterojunction solar cell. *Sol. Energy Mater. Sol. Cells* **144**, 359–363 (2016).
66. Boscarino, S., Crupi, I., Mirabella, S., Simone, F. & Terrasi, A. TCO/Ag/TCO transparent electrodes for solar cells application. *Appl. Phys. A Mater. Sci. Process.* **116**, 1287–1291 (2014).
67. Crupi, I. *et al.* Laser irradiation of ZnO:Al/Ag/ZnO:Al multilayers for electrical isolation in thin film photovoltaics. *Nanoscale Res. Lett.* **8**, 1–5 (2013).
68. Benetti, G., Banfi, F., Cavaliere, E. & Gavioli, L. Mechanical properties of nanoporous metallic ultrathin film: A paradigmatic case. *Nanomaterials* vol. 11 3116 (2021).
69. Hecht, D. S., Hu, L. & Irvin, G. Emerging transparent electrodes based on thin films of carbon nanotubes, graphene, and metallic nanostructures. *Adv. Mater.* **23**, 1482–1513 (2011).
70. Han, C. *et al.* Towards bifacial silicon heterojunction solar cells with reduced TCO use. *Prog. Photovoltaics Res. Appl.* **30**, 750–762 (2022).
71. Cruz, A. *et al.* Optoelectrical analysis of TCO+Silicon oxide double layers at the front and rear side of silicon heterojunction solar cells. *Sol. Energy Mater. Sol. Cells* **236**, 111493 (2022).
72. Lesker Company, K. J. Practical Process Tips - Sputtering. *Lesker Tech* **7**, 1–4 (2010).
73. K. Harsha - Principles of Physical Vapor Deposition of Thin Films- Elsevier (2007).
74. Keifer, G. & Effenberger, F. *Handbook of Sputter Deposition Technology. Angewandte Chemie International Edition* vol. 6 (1967).
75. *MATERIAL AND DEVICE SEMICONDUCTOR MATERIAL AND DEVICE Third Edition.*
76. Feldman, L. C. & Mayer, J. W. Fundamentals of surface and thin film analysis. 352 (1986).
77. Turner, D. W. & Jobory, M. I. A. L. Determination of Ionization Potentials by Photoelectron Energy Measurement. *J. Chem. Phys.* **37**, 3007 (1962).
78. Practical Surface Analysis, 2nd ed. Volume 1 - Auger and X-ray Phototelectron Spectroscopy. (1990).
79. Hüfner, S. *Photoelectron spectroscopy: principles and applications.*

- (Springer Verlag, 1995).
80. Hull, A. W. A New Method of X-ray Crystal Analysis. *Phys. Rev.* **10**, 661 (1917).
 81. science, E. M.-P. in surface & 1992, undefined. Atomic force microscopy. *Elsevier* **41**, 3–49 (1992).
 82. Rugar, D., today, P. H.-P. & 1990, undefined. Atomic force microscopy. *if.ufrj.br*.
 83. Giessibl, F. J. Advances in atomic force microscopy. *Rev. Mod. Phys.* **75**, 949–983 (2003).
 84. Glatzel, T., Lux-Steiner, M. C., Strassburg, E., Boag, A. & Rosenwaks, Y. Principles of kelvin probe force microscopy. *Scanning Probe Microsc.* **2**, 113–131 (2007).
 85. Melitz, W., Shen, J., Kummel, A. C. & Lee, S. Kelvin probe force microscopy and its application. *Surf. Sci. Rep.* **66**, 1–27 (2011).
 86. Panchal, V., Pearce, R., Yakimova, R., Tzalenchuk, A. & Kazakova, O. Standardization of surface potential measurements of graphene domains. *Sci. Rep.* **3**, 1–8 (2013).
 87. Goldstein, J., Newbury, D., Michael, J. & Ritchie, N. Scanning electron microscopy and X-ray microanalysis. (2017).
 88. Heinrich, K. & Newbury, D. Electron probe quantitation. (2013).
 89. Schroder, D. K. Semiconductor Material and Device Characterization: Third Edition. *Semicond. Mater. Device Charact. Third Ed.* 1–779 (2005) doi:10.1002/0471749095.
 90. Mistrik, J., Kasap, S., Ruda, H. E., Koughia, C. & Singh, J. *Optical properties of electronic materials: fundamentals and characterization. Springer Handbooks* (2017). doi:10.1007/978-3-319-48933-9_3.
 91. Jimenez, J. & Tomm, J. W. *Spectroscopic Analysis of Optoelectronic Semiconductors. Springer Series in Optical Sciences* vol. 202 (2016).
 92. Enel Green Power, the platform dedicated to renewables | Enel Green Power. <https://www.enelgreenpower.com/>.
 93. Galluzzo, F. R. *et al.* Experimental investigation and characterization of innovative bifacial silicon solar cells. *Int. J. Renew. Energy Res.* **9**, 1995–2002 (2019).
 94. Ricco Galluzzo, F. *et al.* Electrical characterization of high-efficiency bifacial silicon solar cells. *IET Conf. Publ.* **2018**, 5–8 (2018).

95. Galluzzo, F. R. *et al.* Numerical modeling of bifacial PV string performance: Perimeter effect and influence of uniaxial solar trackers. *Energies* **13**, 1–19 (2020).
96. Galluzzo, F. R., Canino, A., Gerardi, C. & Lombardo, S. A. A new model for predicting bifacial PV modules performance: First validation results. *Conf. Rec. IEEE Photovolt. Spec. Conf.* 1293–1297 (2019) doi:10.1109/PVSC40753.2019.8980925.
97. Micali, M., Cosentino, S. & Terrasi, A. Structural, optical and electrical characterization of ITO films co-doped with Molybdenum. *Sol. Energy Mater. Sol. Cells* **221**, (2021).
98. Gruner, G. Carbon nanotube films for transparent and plastic electronics. *J. Mater. Chem.* **16**, 3533–3539 (2006).
99. Vollmer, A. *et al.* Electronic and structural properties of graphene-based transparent and conductive thin film electrodes. *Appl. Phys. A Mater. Sci. Process.* **94**, 1–4 (2009).
100. Bhachu, D. S. *et al.* Origin of high mobility in molybdenum-doped indium oxide. *Chem. Mater.* **27**, 2788–2796 (2015).
101. Yoshida, Y., Gessert, T. A., Perkins, C. L. & Coutts, T. J. Development of radio-frequency magnetron sputtered indium molybdenum oxide. *J. Vac. Sci. Technol. A Vacuum, Surfaces, Film.* **21**, 1092–1097 (2003).
102. Elangovan, E., Marques, A., Fernandes, F. M. B., Martins, R. & Fortunato, E. Preliminary studies on molybdenum-doped indium oxide thin films deposited by radio-frequency magnetron sputtering at room temperature. *Thin Solid Films* **515**, 5512–5518 (2007).
103. Deangelis, A. D. *et al.* Temperature-resistant high-infrared transmittance indium molybdenum oxide thin films as an intermediate window layer for multi-junction photovoltaics. *Sol. Energy Mater. Sol. Cells* **127**, 174–178 (2014).
104. Meng, Y. *et al.* A new transparent conductive thin film In₂O₃:Mo. *Thin Solid Films* **394**, 218–222 (2001).
105. Sun, S. Y., Huang, J. L. & Lii, D. F. Properties of indium molybdenum oxide films fabricated via high-density plasma evaporation at room temperature. *J. Mater. Res.* **20**, 247–255 (2005).
106. Warm Singh, C. *et al.* High-mobility transparent conducting Mo-doped In₂O₃ thin films by pulsed laser deposition. *J. Appl. Phys.* **95**, 3831–3833 (2004).
107. Yamada, N., Tatejima, T., Ishizaki, H. & Nakada, T. Effects of postdeposition annealing on electrical properties of Mo-doped indium

- oxide (IMO) thin films deposited by RF magnetron cosputtering. *Japanese J. Appl. Physics, Part 2 Lett.* **45**, (2006).
108. Li, X. *et al.* The electrical and optical properties of molybdenum-doped indium oxide films grown at room temperature from metallic target. *Semicond. Sci. Technol.* **20**, 823–828 (2005).
109. Hai, Y. *et al.* Effects of deposition temperature on structure and properties of mo-doped indium oxide by radio frequency magnetron sputtering. *Vacuum* **85**, 211–213 (2010).
110. Mirabella, S. *et al.* Light absorption in silicon quantum dots embedded in silica. *J. Appl. Phys.* **106**, (2009).
111. Nadaud, N., Lequeux, N., Nanot, M., Jové, J. & Roisnel, T. Structural studies of tin-doped indium oxide (ITO) and In₄Sn₃O₁₂. *J. Solid State Chem.* **135**, 140–148 (1998).
112. González, G. B. *et al.* Neutron diffraction study on the defect structure of indium-tin-oxide. *J. Appl. Phys.* **89**, 2550–2555 (2001).
113. Morales-Masis, M., De Wolf, S., Woods-Robinson, R., Ager, J. W. & Ballif, C. Transparent Electrodes for Efficient Optoelectronics. *Advanced Electronic Materials* vol. 3 (2017).
114. Sharma, S., Shriwastava, S., Kumar, S., Bhatt, K. & Tripathi, C. C. Alternative transparent conducting electrode materials for flexible optoelectronic devices. *Opto-electronics Rev.* **26**, 223–235 (2018).
115. Boscarino, S. *et al.* Morphology, Electrical and Optical Properties of Cu Nanostructures Embedded in AZO: A Comparison between Dry and Wet Methods. *mdpi.com* (2022) doi:10.3390/mi13020247.
116. Ren, Z. *et al.* Strategies for high performance perovskite/crystalline silicon four-terminal tandem solar cells. *Sol. Energy Mater. Sol. Cells* **179**, 36–44 (2018).
117. Li, S. *et al.* Transparent-conductive-oxide-free front contacts for high-efficiency silicon heterojunction solar cells. *Joule* **5**, 1535–1547 (2021).
118. Han, C. *et al.* Towards bifacial silicon heterojunction solar cells with reduced TCO use. *Prog. Photovoltaics Res. Appl.* **30**, 750–762 (2022).
119. Liang, Y. C. & Liang, Y. C. Physical properties of low temperature sputtering-deposited zirconium-doped indium oxide films at various oxygen partial pressures. *Appl. Phys. A Mater. Sci. Process.* **97**, 249–255 (2009).
120. Rucavado, E. *et al.* Zr-doped indium oxide electrodes: Annealing and thickness effects on microstructure and carrier transport. *Phys. Rev.*

- Mater.* **3**, 084608 (2019).
121. Aissa, B., Zakaria, Y., Shetty, A. R., Samara, A. & Broussillou, C. High Electron-Mobility of a Transparent and Conductive Zr-Doped In₂O₃ Deposited by Reactive Magnetron Sputtering. *Conf. Rec. IEEE Photovolt. Spec. Conf.* 71–73 (2021)
doi:10.1109/PVSC43889.2021.9518643.
 122. Morales-Masis, M. *et al.* Highly Conductive and Broadband Transparent Zr-Doped In₂O₃ as Front Electrode for Solar Cells. *IEEE J. Photovoltaics* **8**, 1202–1207 (2018).
 123. Guillén, C. & Herrero, J. Structure, optical, and electrical properties of indium tin oxide thin films prepared by sputtering at room temperature and annealed in air or nitrogen. *J. Appl. Phys.* **101**, (2007).
 124. Gwamuri, J. *et al.* Limitations of ultra-thin transparent conducting oxides for integration into plasmonic-enhanced thin-film solar photovoltaic devices. *Mater. Renew. Sustain. Energy* **4**, 1–11 (2015).

Acknowledgements

Quando decisi di intraprendere la strada del dottorato di ricerca, lo feci con l'estrema convinzione e determinazione che questo percorso avrebbe arricchito la mia carriera rendendomi un'esperta nel mio settore di ricerca. Ciò di cui non avevo minimamente idea è quello che questa esperienza mi avrebbe donato al di là della pura formazione lavorativa. Il Dottorato mi ha insegnato a gestire il mio tempo, mi ha messo di fronte a sfide difficili e mi ha insegnato a pensare in un modo che solo chi ha intrapreso lo stesso percorso può comprendere. Tutto ciò non sarebbe stato possibile senza l'aiuto di alcune persone che hanno condiviso con me questi anni e che pertanto vorrei ringraziare.

I primi ringraziamenti vanno al mio tutor, il **Prof. Antonio Terrasi**, e a tutto ciò che mi ha insegnato. Lo ringrazio per non essersi mai accontentato di ciò che facevo e avermi sempre spronato a fare meglio, perché nella vita in fondo si può sempre migliorare, e senza questa filosofia, oggi, non sarei la persona che sono e non sarei dove sono adesso. Lo ringrazio per avermi guidato lasciandomi però la libertà di pensare e di condurre gli esperimenti, come un leader dovrebbe fare. Lo ringrazio per il tempo che mi ha dedicato anche quando le sue ore di lavoro erano terminate e per il clima sempre scherzoso e allegro dei nostri meeting. Infine, lo ringrazio per aver iniziato a credere in me senza mai smettere.

I wish to thank all the people that I met during the period that I spent at Amolf Institute and a special thanks, is for you **Esther**, you had been my second supervisor for a couple of months, but more than that. You welcomed me into your wonderful group, helping me in every technical and emotional situation. You are the perfect balance between work and family, and one of the women with the strongest personality I ever meet. This experience would not have been possible without you **Albert**, you accepted me as a guest in your Institute, but I never felt like a guest, but always like a part of the team, so thank you. Thank you also to all of the people in my group. First of all **Daphne**, my first friend in the Netherlands, thank you for becoming close to me, for all our days together inside and outside Amolf, thank you for our trip, for our shopping sessions, and every single little gesture. **Yorick**, you spent a lot of time with me in our electrochemistry sessions, helping me with my mental breakdown and never complaining about my messing up everything, so thank you for these and all our drinking nights always ending up with me falling from my bike. Thank you, **Alex**, for all of our coffee breaks and to be always nice to me and **Daniel** for our long

conversation about life at the coffee corner. Thank you also to the old members of the group **Hallie** and **Kaj** and to all the other people met there, **Stefan, Eveljin, Gianluca, Sarah, Susan, Hongyu Sun, Mees, Patrick, Moritz, Imme, Matthias, Nika, Falco, Parisa, Dhawal, Bob, Igor, and Alberto**. Infine tra tutte le persone incontrate ad Amolf, vorrei ringraziare particolarmente **Francesca**, grazie per essere diventata una mia amica più che una semplice collega, e **Andrea** per avermi aiutato nelle fasi cruciali del mio trasferimento sebbene non mi conoscesse e per sostenere sempre l'italian-team creatosi di Amolf.

Ringrazio inoltre tutto i membri ed il personale tecnico del cnr, tra cui in particolare **Vicky, Maria Canteralla, Maria Miritello, Maria Antonietta, Massimo e Giuseppe Pantè**. Ringrazio tutti i ragazzi **Antonio, Maria Josè, Andrea, Fiorella, Salvo, Nino, Sergio e Stefano, Noemi, Marica e Annalisa**. Ringrazio in particolare **Maria Censabella**, per essere stata una mia fedele compagna di avventure e ti auguro tutto il meglio che la vita ti possa donare.

Ringrazio la mia gang anche se per ringraziarvi di tutti questi anni non basterebbero 10 pagine, cercherò di fare del mio meglio. **Luca, Giacometta e Gisella**, siete stati molto più che dei colleghi in questi anni, per tutto ciò che abbiamo condiviso e per il gruppo indistruttibile che abbiamo formato. Ringrazio anche l'evoluzione del nostro gruppo, la **stanza dottorandE**, con il nuovo membro della gang, la piccola **Vale**. Non potrò mai dimenticare le nostre piccole abitudini, come me e Gisella al parcheggio la mattina con la stessa macchina, molto spesso le ultime a lasciare l'edificio, i nostri caffè fissi, ognuna conoscendo esattamente quante zollette di zucchero vanno nel caffè dell'altra, i nostri gossip, i nostri modi di dire, il nostro capirci solo con lo sguardo. *Grazie, siete una delle cose che è stato più difficile lasciare e che mi mancherà di più.*

Ringrazio i miei amici più cari, quelli che mi conoscono da sempre, come **Giuliana, Aurelio e Giada**, siete una di quelle amicizie che può durare una vita, non importa come, dove quando e perché io per voi ci sarò sempre.

Grazie a te **Alice**, la mia prima coinquilina, la mia amica, la mia compagna di cinema, di viaggio, di cene, di colazioni, di complessi e di problemi. Abbiamo vissuto un milione di avventure (riguardati il video del tuo compleanno nel caso in cui non te le ricordassi), grazie per avermi permesso di far parte della tua vita condividendola con me. Grazie per avermi sempre ascoltata con pazienza e comprensione durante le mia crisi senza mai giudicarmi.

Ringrazio la mia famiglia, mia sorella **Michelle** prima di tutti, che anche con il suo carattere "difficilino" riesce ad esserci sempre quando ho bisogno, ti aspetto ad Amsterdam e sappi che ci sarò sempre per te anche se sarò lontana. Grazie ai miei genitori, ai miei nonni, zii e cugini per avermi sempre sostenuta, essere sempre stati orgogliosi e aver sempre creduto in me.

Infine ringrazio me stessa, per non essermi mai arresa nei momenti più difficili, per essere riuscita a dare una svolta alla mia vita tirando fuori un coraggio che non avrei mai pensato di avere.

List of publications

1. **Micali, M.**, Cosentino, S., & Terrasi, A. (2021). Structural, optical, and electrical characterization of ITO films co-doped with Molybdenum. *Solar Energy Materials and Solar Cells*, 221, 110904.
2. **Micali M.**, Leonardi M., Lombardo S., Bengasi G., Colletti C.; Alarcón Lladó E., Terrasi A.. Zr-doped Indium Oxide as transparent electrodes for photovoltaics. – In Preparation
3. Achilli, E.; Annoni, F.; Armani, N.; Patrini, M.; Cornelli, M.; Celada, L.; **Micali M.**; Terrasi, A.; Ghigna, P.; Timò, G. Capabilities of Grazing Incidence X-ray Diffraction in the Investigation of Amorphous Mixed Oxides with Variable Composition. *Materials* 2022, 15, 2144.
4. Boscarino, S., Censabella, **M.**, **Micali**, M., Russo, M., Terrasi, A., Grimaldi, M. G., & Ruffino, F. (2022). Morphology, Electrical and Optical Properties of Cu Nanostructures Embedded in AZO: A Comparison between Dry and Wet Methods. *Micromachines*, 13(2), 247

Curriculum Vitae



Melanie Micali was born in June 9th, 1993 in Catania. She attained her Master Degree in Physics on July 19th, 2019 at the University of Catania. In November 2019, she started the PhD course in Materials Science and Nanotechnologies at the University of Catania and CNR-IMM. Her Ph.d project developed under the supervision of Prof. Antonio Terrasi concerned on the growth and characterization of transparent conductive oxide through magnetron sputtering for photovoltaic applications. She attained her Ph.D at the University of Catania, Dep. of Physics and Astronomy “Ettore Majorana”. She spent part of her PhD course (November 2021-July 2022) at Amolf Institute Institut (Amsterdam, Netherlands), in the “3D Photovoltaics Group” under the supervision of Dr. Esther Alarcón Lladó. During the PhD course she presented the results of her research activity, giving both oral and poster contributions, at the following international conferences: European Materials Research Society, Spring Meeting 2021(Online); EUROMAT 2021 European Congress and Exhibition on Advanced Materials and Processes (Online); TCM-TOEO 2021 Conference 8th International Symposium on Conductive Materials & 12th International Symposium on Transparent Oxide and Related Materials for Electronics and Optics (Online); E-MRS Spring Meeting 2022 where she attained as Invited Speaker and She won the Young Scientist Award at Symposium G: “Materials for sustainable energy technologies (M-SET)”. Melanie Micali is author or co-author of several articles, published in international referred scientific journals.

